UNIVERSITY OF SOUTHAMPTON

New Recoupling Techniques in Solid-State NMR

by
Ildefonso Marín Montesinos

A thesis submitted for the
degree of Doctor of Philosophy

Faculty of Engineering, Science and Mathematics
School of Chemistry

June 2007

Abstract

This thesis deals with the development of new methodology for homonuclear dipolar recoupling by symmetry-based radiofrequency pulse sequences in magic-angle-spinning solid-state nuclear magnetic resonance.

The first chapters of this thesis introduce NMR spectroscopy, the basic theory of NMR and some basic elements. After these introductory chapters, the rotor-synchronized symmetry-based pulse sequences are described. Each class of symmetry-based pulse sequence is defined, introducing their selection rules and scaling factors for the recoupling of certain spin interactions.

In the second part, the main topics and subjects of the thesis are analysed more deeply. First, the interference of heteronuclear dipolar decoupling in the homonuclear dipolar recoupling by symmetry-based pulse sequences is considered. These effects are studied by experiments, simulations and average Hamiltonian theory in two families of dipolar recoupling sequences belonging to the CN_n^ν and the RN_n^ν symmetry classes.

In the final chapter, a new recoupling concept in multiple-spin systems called truncated dipolar recoupling (TDR) is presented. This new concept allows the selective determination of internuclear distances in a wide variety of homonuclear multiple-spin systems. This methodology involves a symmetry-based recoupling sequence that generates: (i) Zero-quantum (ZQ) recoupling of homonuclear dipole-dipole interactions; (ii) simultaneous recoupling of frequency-dispersing spin interactions that truncate the ZQ dipolar Hamiltonian. This truncation of the spin Hamiltonian allows the commutation of the different dipolar coupling in the multiple spin system. Two different implementations of this idea are discussed and demonstrated experimentally and by numerical simulations.

Contents

Acknowledgements

All the work behind this thesis could not have been possible without the help and support of many people. I would like to mention the people who contributed, one way or another, to this work.

First of all, I would like to express my gratitude to my supervisor Malcolm Levitt for his support, encouragement, motivation and confidence throughout these three years. Thank you for giving me the of joining your group and for guiding me through the world of the nuclear magnetic resonance. Thanks for the time spent on me during these last years, especially during the correction of my thesis.

I am very grateful to all the members and visitors of the group: Marina, Ole, Darren, Jacco, Natala, Linda, Axel, Giancarlo, Peppe, Maria, Salvo, Giulia, Angelika, Matthias, Madhu, Pauline and Andree. All of them have been of great help and support during my PhD. Darren Brouwer, for his enthusiastic help in my first steps in solid-state NMR, his extremely useful advice and his assistance with the first chapters of my thesis. Marina, for teaching me many NMR, computer-related and instrumental issues. I have enjoyed a lot your home-made Italian food. Ole, for helping with instruments and computers. Your assistance was essential throughout these three years. I have also enjoyed a lot your sense of humour, the football matches at Saint Mary's and the Norwegian bacalao. Just one problem, you are a Real Betis supporter. Axel, for his enthusiastic help with experiments. You always had a moment for a interesting and stimulating discussion, not only about NMR. Giancarlo, who helped me with theoretical and mathematical stuff. Thanks to Peppe and Maria, for their cooperation and support. The parties at your place were very nice. Jacco, for helping me with theoretical and computer related issues

Thanks go to Darren, Andreas, Giancarlo and Linda for their invaluable help with my first work. Many thanks to Peppe, Axel, Giulia, Marina, Ole, Matthias and Angelika for the great and hard work in the TDR project.

I would like to thank the EPSRC and the School of Chemistry for the financial support of these three years.

Thanks to Angelika Sebald for helping me with my thesis plan. Her counsels were very constructive. I have also appreciated discussions with Geoffrey Luckhurst and Jim Emsley. Also, I am very grateful with Marek for his confidence and collaboration.

Thanks to Rozid for his friendship and Azizah for being the nicest person that I met in-

Southampton. Thanks to all the friends who supported me during these years in Southampton, Kasia, Laurent, Ismael, Ruben, Martin, Eva, Marco, Caterina and Bruno.

Gracias a todos los amigos que me han apoyado durante estos tres años, desde España: Roberto, Reyes, Paco, Ángela, Iván, Nuria, Ángela e Isabel. Mi agradecimiento a Manuel y Manoli por su interés y apoyo durante estos tres años.

Muchas gracias a mis padres, Agustín y Antonia, por su imensa ayuda, motivación, apoyo e interés. Sin vosotros nada de esto hubiera sido posible. También quiero agradecer el apoyo y las visitas durante estos años de mis hermanos (Agustín, Paqui y Antonio) y mi cuñada (Celia).

Finalmente gracias a Isabel, por su amor, por estar siempre a mi lado, apoyandome y dandome ánimos. Gracias por soportar los días de intenso trabajo y ser mi motor auxiliar cuando fue necesario, especialmente durante la escritura de la tesis. Esta tesis también te pertenece.

1. Introduction

1.1. Nuclear Magnetic Resonance

Nuclear Magnetic Resonance (NMR) is a spectroscopy in which nuclear spin levels are split by a strong static magnetic field and an observable signal is generated by inducing transitions between these levels with a modulated magnetic field.

NMR was first discovered in 1946 independently by Purcell et al. [1] and Bloch et al. [2]. Both shared the Nobel Prize in Physics in 1952 for their discovery. They noticed that magnetic nuclei could absorb radiofrequency energy when placed in a magnetic field of a strength specific to the identity of the nuclei. That was the beginning of NMR spectroscopy.

At the beginning, the technique was used and developed by physicists to study magnetic properties, but soon, the technique was applied in chemistry due to the strong relation of the NMR signal with the surrounding environment of nuclei [3], [4]. Nowadays, NMR is an essential technique for studying matter, its properties and its structure, having important applications for liquid and solid samples in many fields, from inorganic materials to biological complex systems. Also, a technique called magnetic resonance imaging (MRI) has important application in medicine.

1.2. Solid-State NMR

Over the last decades the interest in solid materials has grown enormously in the scientific community and in industry due to their properties. Many fields of chemistry, physics, biology and engineering are involved in the research, development, study, or practical applications of materials which are solids or have a behaviour close to a solid, such as glasses, polymers, synthetic products, ceramics or proteins. Therefore, for many researchers, it is important to have an insight in the structure and properties of these materials.

Solid-state NMR is an important tool for the study of solid materials or anisotropic phases and it is commonly used for a wide range of applications from characterization of inorganic materials to the study of membrane proteins, and dynamics processes in solids. Solid-state NMR has been always an important technique for investigating solids, but due to the broad features in the spectra and the difficulty of their interpretation, solid-state NMR was

applied later to chemistry and biochemistry. However, with the development of techniques such as magic-angle-spinning (see chapter 4), cross-polarization (see chapter 4) and heteronuclear decoupling (see chapter 4), the spectral resolution and resolution were increased and solid-state NMR entered the "world" of chemistry and biology. Additionally, new techniques to recouple anisotropic interactions removed during application of MAS, and heteronuclear decoupling, were introduced, recovering the structural information given by these interactions. Therefore, solid-state NMR is one of the most important and complete techniques for solids.

2. Nuclear Magnetism

Matter is made of *atoms* which are composed of *electrons* and *nuclei*. The nucleus has four important physical properties: *mass*, *electric charge*, *magnetism* and *spin*.

The nucleus interacts with magnetic fields like a small magnet. This property is called nuclear magnetism. The nucleus has intrinsic angular momentum, which is known as spin.

The properties of nuclear magnetism and spin have almost no effect on the physical and chemical properties of the matter. However, these two properties and their interactions represent very powerful tools for investigating the microscopic and internal structures of objects without disturbing them, being the essential principle of NMR spectroscopy.

2.1. Nuclear Spin and Magnetic Moment

Concepts such as *angular momentum* and *magnetic moment* are familiar from classical physics. Elementary particles, such electrons and photons, also have an angular momentum associated with the movement of the particle. However, from the application of the *relativistic quantum mechanics* to these particles an additional property called spin is derived [5].

Table 2.1 Selection of nuclear spin and their properties of interest in NMR [6], [7].

Isotope	Ground state spin	Natural Abundance %	Gyromagnetic ratio γ/rad s^{-1} T^{-1}	NMR frequency at 9.4 T $(\omega_0/2\pi)$/MHz
^{1}H	½	~100	267.522×10^{6}	-400.000
^{2}H	1	0.015	41.066×10^{6}	-61.437
^{13}C	½	1.1	67.283×10^{6}	-100.602
^{14}N	1	99.63	19.338×10^{6}	-28.914
^{15}N	½	0.37	-27.126×10^{6}	40.559

The spin is a form of angular momentum which is an intrinsic property of the particle and is not related with a physical rotation. According to quantum mechanics, the *spin angular momentum* is quantized taking values of the form $\hbar\sqrt{S(S+1)}$, where $\hbar$ is the Planck's constant divided by 2π and S is the *spin quantum number*. Each elementary particle has an associated spin quantum number that is either an integer number (0, 1, 2, ...) or a half-integer (1/2,

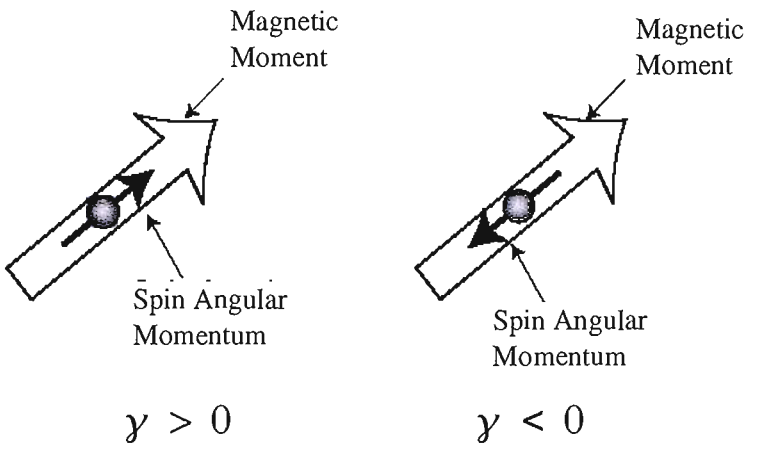

Fig. 2.1. The sign of the gyromagnetic ratio (From [6]).

3/2, ...). For instance, electrons have spin-1/2, whereas photons have spin-1.

The nuclear spin depends on the spin of their constituents: *nucleons* (protons and neutrons), which are made of elementary particles called *quarks*, held together by *gluons*. Therefore, the nuclear spin quantum number can be an integer or a half-integer number [6]. NMR spectroscopy can only be performed on nuclei with spin not equal to 0. Table 2.1 contains properties for the commonest nuclei in NMR. In the context of this thesis, only ^{13}C and ^{1}H are of interest.

The nuclei with spin $S \neq 0$ have an *associated magnetic moment* that is proportional to the spin angular momentum [8], [9]:

$$\hat{\mu} = \gamma \hat{S} \tag{2.1}$$

where γ is the gyromagnetic ratio in units of rad s^{-1} T^{-1} [6]. The gyromagnetic ratio has a positive or negative sign depending on the relative orientation between the spin angular momentum and the magnetic moment (Fig. 2.1).

2.2. Spin Precession and Larmor Frequency

Consider an ensemble of nuclei. In the absence of a magnetic field the spin angular momentum of each spin can point in any possible direction in space. The distribution of magnetic moments is completely *isotropic*.

Generally, NMR spectroscopy involves a strong static magnetic field along one direction (defined as the *z-direction* in the *laboratory frame*, see section 3.3). In this situation, the spin polarization starts moving around the magnetic field. The magnetic moment of the spin

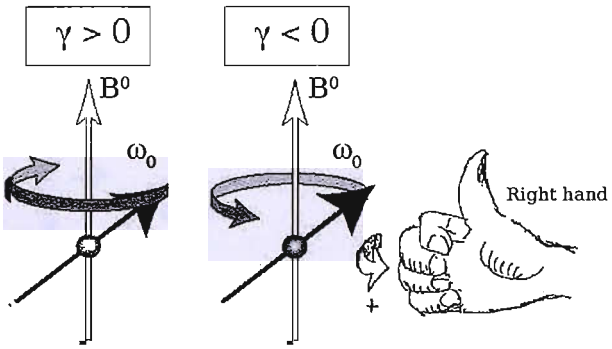

Fig. 2.2. Spin precession for spins with negative and positive gyromagnetic ratio and determination of the sense of the precession by using one's right hand rule (From [6]).

moves on a cone defined by the angle between the spin magnetic moment and the magnetic field. This movement is called *precession* around the axis of the magnetic field.

The nuclear spin precesses around the external magnetic field with a frequency called the *Larmor frequency*, which is equal to:

$$\omega_0 = -\gamma B^0 \tag{2.2}$$

where B^0 is the magnitude of the external magnetic field. The sign of γ determines the sense of the precession (Fig. 2.2). The Larmor frequency ω_0 is expressed in rad s^{-1} and $\omega_0/2\pi$ is given in Hz. Table 2.1 contains the Larmor frequencies of several nuclei at $B^0 = 9.4$ T.

2.3. Longitudinal Magnetization and Relaxation

Considering the proton nuclei in a sample of water in the absence of an external field, the *spin polarization* is spread in all the possible orientations and the total magnetic moment is close to zero.

If a strong magnetic field along one direction is turned on, all the spins start to precess at the Larmor frequency. This has no effect on the total spin polarization and the *isotropic distribution* of magnetic moments makes no contribution to the magnetism of the sample. However, the ^{1}H nuclei share the molecular environment with other magnetic particles, including electrons and other nuclei. Because of *thermal motion* of these particles the local magnetic fields fluctuate rapidly in time. Therefore, the protons feel a total magnetic field that fluctuates slightly in magnitude and direction. These small fluctuations are very import-

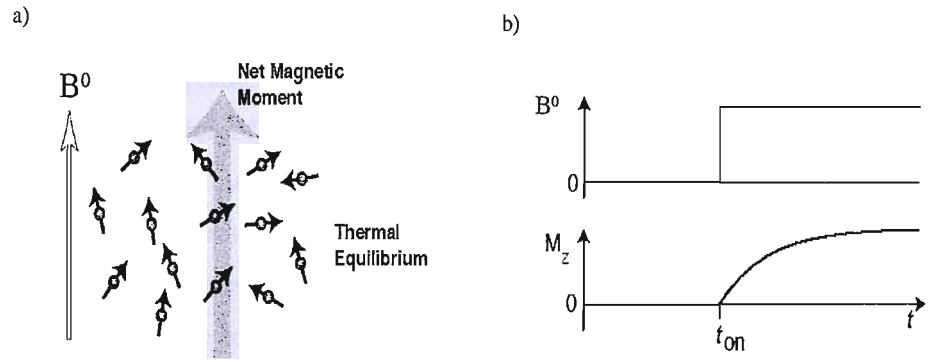

Fig. 2.3. a) Longitudinal magnetization after the thermal equilibrium is reached. The net magnetic moment has been exaggerated. b) Buildup of longitudinal spin magnetization when a strong magnetic field is switched on (from [6]).

ant because they break the isotropy of the system and a macroscopic nuclear magnetic moment arises.

This magnetic moment, due to the fact that an orientation with low energy is more favourable than an orientation with *high energy*, leads to a stable *anisotropic distribution* parallel to the external magnetic field, called *thermal equilibrium*.

The anisotropy of the magnetic distribution in thermal equilibrium means that the entire sample acquires a small net magnetization along the field which is called *longitudinal magnetization*.

The total nuclear magnetization is initially zero when the external magnetic field is turned on. However, due to the process described above, a small net magnetization grows in the direction of the applied magnetic field (z-direction). The build up of longitudinal magnetization (Fig. 2.3) follows an exponential behaviour which is given by:

$$M_z^{nuc}(t) = M_{eq}^{nuc}(1 - \exp\{-(t - t_0)/T_1\}) \tag{2.3}$$

where t_0 is the time at which the external field is applied and T_1 is known as a *longitudinal relaxation time constant* or *spin-lattice relaxation time constant*. Typically, this constant is in the range of milliseconds to seconds, however in some cases could be as long as days or even years.

2.4. Transverse Magnetization and Relaxation

The longitudinal magnetization has a rather small magnitude, which makes NMR spectroscopy a comparatively insensitive technique. In NMR, the measured magnetization is the

magnetization *perpendicular* to the strong magnetic field. The polarization of each spin is suddenly rotated by $\pi/2$ radians around the x-axis (Fig. 2.4) by applying a radiofrequency (r.f.) pulse of appropriate frequency and duration. (see section 3.4.3). The pulse rotates the entire spin polarization of the sample, transferring the net spin polarization from the z-axis to the y-axis. This net magnetization is called *transverse magnetization.*

After the pulse, the spins start to precess on their individual cones in the xy-plane, leading to a precession of the total magnetic moment.

Components of the transverse magnetization after a time t have the form:

$$M_y^{nuc}(t) = -M_{eq}^{nuc}\cos(\omega_0 t)\exp\{-(t/T_2)\}$$
$$M_x^{nuc}(t) = M_{eq}^{nuc}\sin(\omega_0 t)\exp\{-(t/T_2)\} \qquad (2.4)$$

After a time of evolution in the xy-plane the nuclear precessing spins start to lose synchronization because each nuclear spin feels a slightly different field. Gradually the nuclear spins get out of phase with each other and the transverse magnetization decays slowly because it is impossible to maintain the synchronization of the precessing nuclear magnets. This decay is called *homogeneous decay*. The time constant T_2 (*transverse relaxation constant, coherence dephasing time constant or spin-spin relaxation time constant*) is used to describe this homogeneous decay of the precessing transverse magnetization. For liquids T_2 is in the range of several seconds but in solids or large molecules in solution this time may be several milliseconds.

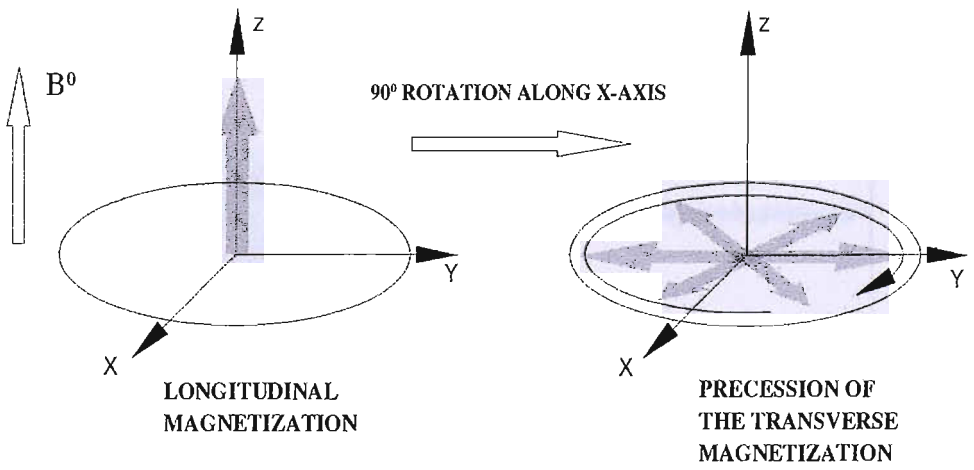

Fig. 2.4. The longitudinal magnetization is rotated by a 90 degree r.f. pulse along x-axis and converted into transverse magnetization, which precesses in the xy-plane with a frequency equal to the Larmor frequency.

2.5. NMR signal

The rotating transverse magnetic moment generates a rotating magnetic field. Following *Maxwell's equations* [10] this rotating magnetic field is associated by an oscillating electric field. If a wire coil is located close to the sample, the rotating transverse magnetic field induces an oscillating electric current in the coil that can be detected by using a radiofrequency detector. The oscillating electric current induced by the transverse magnetization is called the *NMR signal or free-induction decay* (FID).

The NMR spectrometer is a device capable of registering an FID and by a *Fourier transformation* of the FID to obtain the NMR spectrum.

For an extensive description of the NMR spectrometer and Fourier transform methods see [6], [11], [12].

2.6. NMR Spectrum

The NMR spectrum is obtained by transforming the NMR signal through a mathematical technique called Fourier transform [12]. The FID is amplified and processed in the NMR spectrometer [6] producing the quadrature-detected signal:

$$s(t) \sim \exp\{(i\Omega^0 - \lambda)t\} \tag{2.5}$$

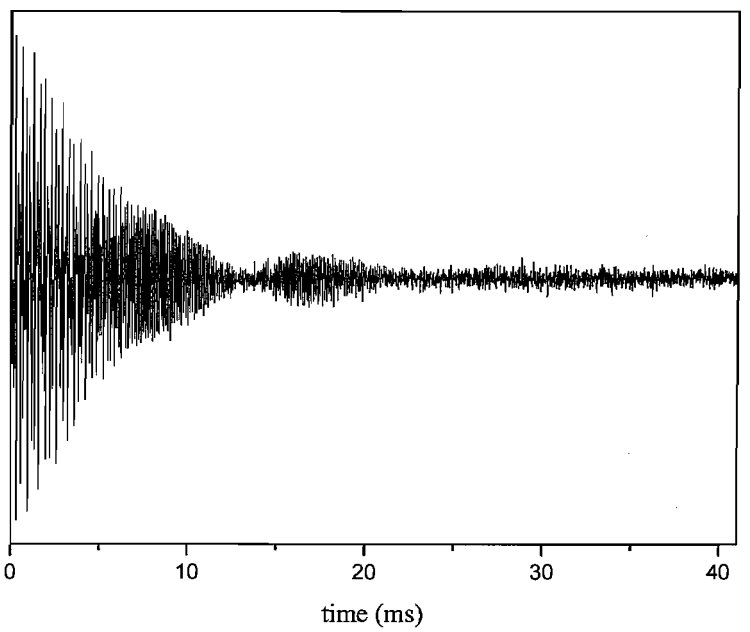

Fig. 2.5. NMR signal or FID of a one-pulse experiment for $^{13}C_3$-alanine.

where λ is a rate constant equal to T_2^{-1} and Ω^0 is equal to:

$$\Omega^0=\omega_0-\omega_{ref} \tag{2.6}$$

with ω_0 equal to the Larmor frequency for each spin and ω_{ref} is the spectrometer reference frequency. A more general signal contains a superposition of different signal components s_l:

$$s(t)=\sum_l s_l(t) \tag{2.7}$$

The Fourier transform converts the time-dependent signal *s(t)* into a frequency function S(Ω) as follows:

$$S(\Omega)=\int_0^\infty s(t)\exp\{-i\Omega t\}\,dt \tag{2.8}$$

The time-domain signal and the frequency domain are complex functions, therefore the relation between the real and the imaginary parts may be depicted as follows:

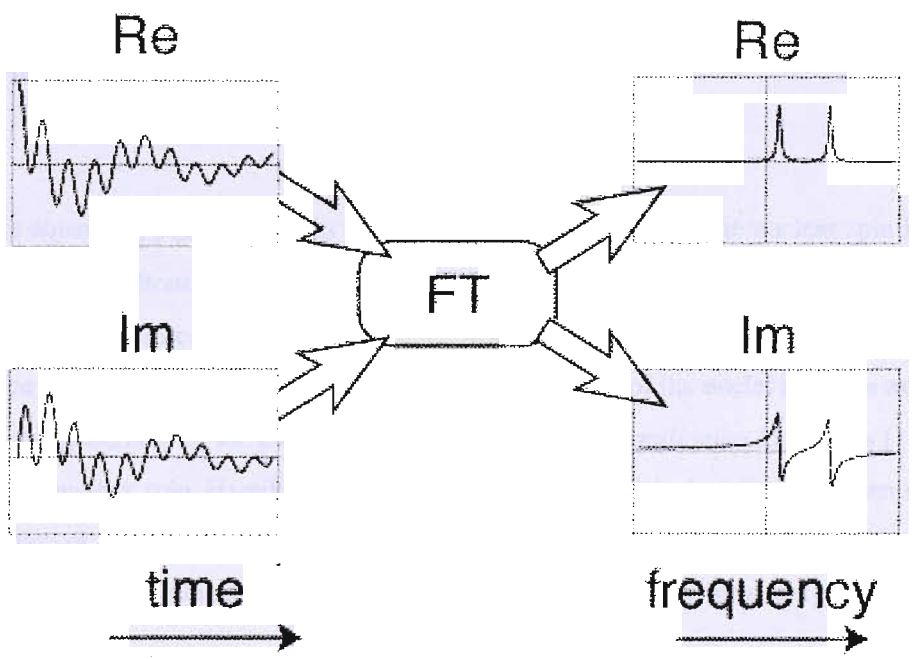

Fig. 2.6. The relationship between the real and the imaginary parts of *s(t)* and *S(Ω)*. Taken from [6]

3. Theory of Solid-State NMR

In this chapter the basics of the *dynamics* of nuclear spins [6] will be treated. For this purpose, it is necessary to solve the *time-dependent Schrödinger equation* for the time evolution of the *quantum state* of a physical system:

$$\frac{d}{dt}|\psi_{full}(t)\rangle = -i\hat{\mathcal{H}}_{full}|\psi_{full}(t)\rangle \tag{3.1}$$

where $\hat{\mathcal{H}}_{full}$ is a *Hermitian operator*, called the *Hamiltonian* associated with the total energy of the system and $|\psi_{full}\rangle$ is the wave function that describes the quantum state of the system. This equation is complete but it is also quite complicated to use because of the enormous amount of information that it contains.

In NMR is possible to work with a much simpler equation which only contains the nuclear spin states:

$$\frac{d}{dt}|\psi_{spin}(t)\rangle \simeq -i\hat{\mathcal{H}}_{spin}|\psi_{spin}(t)\rangle \tag{3.2}$$

in this equation $|\psi_{spin}\rangle$ is the spin state of the nuclei and $\hat{\mathcal{H}}_{spin}$ is the nuclear spin Hamiltonian. This Hamiltonian only includes terms dependent on the nuclear spin. This is possible because the dynamics of electrons are much faster than those of the nuclei. Therefore the influence of the electrons on the magnetic and electric fields of the nuclei is a time average of the fields generated by the electrons. This called the *spin Hamiltonian hypothesis* [13].

The nuclear spin Hamiltonian has different terms which describe the orientation-dependence of the nuclear energy. In general two terms can be described, one is called the *electric spin Hamiltonian* and the second is the *magnetic spin Hamiltonian*:

$$\hat{\mathcal{H}}_{spin} = \hat{\mathcal{H}}^{elec}_{spin} + \hat{\mathcal{H}}^{mag}_{spin} \tag{3.3}$$

The electric spin Hamiltonian vanishes for nuclei with spin number equal to ½ because the charge distribution is spherically symmetrical. However, for nuclei with spin number bigger than ½ (*Quadrupolar nuclei*) this distribution of charge is not spherical and the electric spin Hamiltonian does not vanish. Only spins-1/2 are considered in this thesis.

The magnetic spin Hamiltonian describes the variation of the nuclear magnetic energy when the nucleus is rotated. The magnetic field experienced by a spin-1/2 nucleus can have an external or internal origin. These are referred to as *external* or *internal spin interactions*. In the case of quadrupolar nuclei (spin >1/2), an internal electric interaction is included in

the internal spin interactions.

$$\hat{\mathcal{H}}_{spin}=\hat{\mathcal{H}}^{int}_{spin}+\hat{\mathcal{H}}^{ext}_{spin} \tag{3.4}$$

3.1. Spin Angular Momentum

3.1.1. Angular Momentum Operators

In the quantum description of the *spin angular momentum operator*, the three components along the three axes, x, y and z are denoted by $\hat{I}_x$, $\hat{I}_y$ and $\hat{I}_z$. This three components of the spin angular momentum operator follow the *cyclic commutation relationships* [6], [14], [15], [16]:

$$\begin{aligned}[\hat{I}_x,\hat{I}_y]&=i\hbar\hat{I}_z\\ [\hat{I}_y,\hat{I}_z]&=i\hbar\hat{I}_x\\ [\hat{I}_z,\hat{I}_x]&=i\hbar\hat{I}_y\end{aligned} \tag{3.5}$$

and the *total square spin angular momentum* is equal to:

$$\hat{I}^2=\hat{I}_x^2+\hat{I}_y^2+\hat{I}_z^2 \tag{3.6}$$

Since $\hat{I}^2$ and $\hat{I}_z$ are Hermitian and commute, a common set of *eigenfunctions* $|I, m\rangle$ can be chosen for both operators. The eigenvalues of $\hat{I}^2$ for the eigenfunction $|I, m\rangle$ are given by the *eigenequation*:

$$\hat{I}^2\ |I,m\rangle=\hbar^2 I(I+1)\ |I,m\rangle \tag{3.7}$$

where the *eigenvalues* are given by $\hbar^2 I(I+1)$ with $I = 0, 1/2, 1, 3/2, ...$The eigenvalues $\hat{I}_z$ of for the same eigenfunction are given by:

$$\hat{I}_z\ |I,m\rangle=\hbar m\ |I,m\rangle \tag{3.8}$$

where the eigenvalues are given by $\hbar m$ with $m = -I, -I+1, ..., I-1, I$.

3.1.2. Zeeman Eigenbasis

For an isolated nucleus with spin $I = ½$, the two possible eigenvalues are $m = \pm ½$. The eigenstates of the angular momentum along the z-axis are called *Zeeman eigenstates* and are denoted by:

$$|\alpha\rangle=|\frac{1}{2},+\frac{1}{2}\rangle \tag{3.9}$$

$$|\beta\rangle=|\frac{1}{2},-\frac{1}{2}\rangle \tag{3.10}$$

Therefore, the eigenstates $|\alpha\rangle$ and $|\beta\rangle$ follow the eigenequations:

$$\begin{aligned}\hat{I}_z|\alpha\rangle&=\frac{1}{2}\hbar|\alpha\rangle\\ \hat{I}_z|\beta\rangle&=-\frac{1}{2}\hbar|\beta\rangle\end{aligned} \tag{3.11}$$

The matrix representations of the three components of the spin angular momentum operator in the *Zeeman eigenbasis* are:

$$\hat{I}_z=\frac{1}{2}\begin{pmatrix}1 & 0\\ 0 & -1\end{pmatrix}\ ;\ \hat{I}_x=\frac{1}{2}\begin{pmatrix}0 & 1\\ 1 & 0\end{pmatrix}\ ;\ \hat{I}_y=\frac{1}{2i}\begin{pmatrix}0 & 1\\ -1 & 0\end{pmatrix} \tag{3.12}$$

It is convenient to define the *shift operators* of the spin angular momentum:

$$\begin{aligned}\hat{I}^+&=\hat{I}_x+i\hat{I}_y\\ \hat{I}^-&=\hat{I}_x-i\hat{I}_y\end{aligned} \tag{3.13}$$

and their matrix representations in the Zeeman eigenbasis:

$$\hat{I}^+=\begin{pmatrix}0 & 1\\ 0 & 0\end{pmatrix}\ ;\ \hat{I}^-=\begin{pmatrix}0 & 0\\ 1 & 0\end{pmatrix} \tag{3.14}$$

3.2. Tensors

The physical properties of a system can be described in terms of entities of different dimensionality. In general, the three classes of physical properties can be described as a tensors of different rank. In the NMR context, the different properties of the system can be described as tensors of rank-0 (scalars), tensors of rank-1 (vectors) and tensors of rank-2. Higher order rank tensors can be defined but in the context of NMR are not needed.

Tensors of rank-0 are fully described by a number, for instance, the electric charge or the mass of a particle. A tensor of rank-1 requires the knowledge of its magnitude and direction for a full description of the physical property. Magnetic or electric fields are example of physical properties with rank-1. The third class, tensors of rank-2, manifest different behaviour in different directions and can be represented by a full matrix form. Conductivity, magnetic susceptibility and compressibility, for instance, belong to this class of quantities.

Before going deeper into the concept of tensors, it is useful to introduce the next concepts: Cartesian and spherical systems in three-dimensional space, Euler angles and Wigner

matrices.

3.2.1. Cartesian and Spherical Bases

Three-dimensional space is defined by a basis of three independent vectors. Each point is identified by three numbers which depend on the particular basis which is chosen to represent it. The commonest choice is to adopt the basis as the Cartesian vectors ($\mathbf{e}_x$, $\mathbf{e}_y$, $\mathbf{e}_z$) in the direction of the Cartesian axes as the basis. This basis is known as the canonical basis and it is an orthonormal basis. In this basis a point **P** can be expressed as (in this thesis "non-bold" symbols are used for the magnitudes of vectors):

$$\mathbf{P} = \sum_{k=x,y,z} p_k \mathbf{e}_k \tag{3.15}$$

where the scalar p_k are the projections of **P** on the Cartesian axes and the point can be identified as $\mathbf{P} = (p_x, p_y, p_z)$.

In the description of NMR interactions, it is more convenient, from a mathematical point of view, to use the spherical basis. The *covariant* spherical basis vector [14] is defined as follows:

$$\begin{aligned} \mathbf{e}_{+1} &= -\frac{1}{\sqrt{2}}(\mathbf{e}_x + i\,\mathbf{e}_y) \\ \mathbf{e}_0 &= \mathbf{e}_z \\ \mathbf{e}_{-1} &= \frac{1}{\sqrt{2}}(\mathbf{e}_x - i\,\mathbf{e}_y) \end{aligned} \tag{3.16}$$

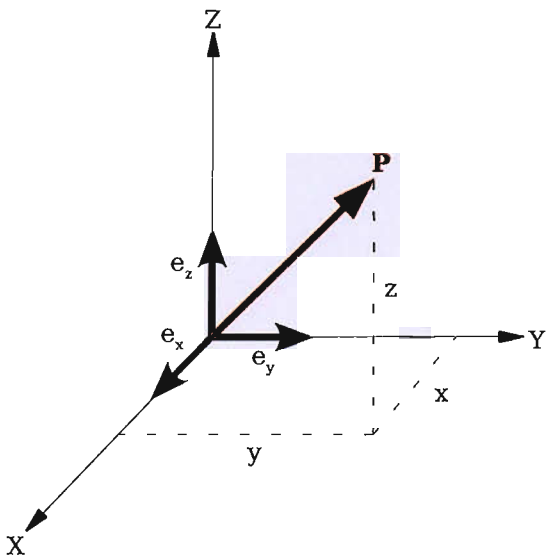

Fig. 3.1. Cartesian coordinate system.

and *contravariant* spherical basis vectors are defined as:

$$\begin{aligned} \mathbf{e}^{+1} &= -\frac{1}{\sqrt{2}}(\mathbf{e}_x - i\mathbf{e}_y) \\ \mathbf{e}^{0} &= \mathbf{e}_z \\ \mathbf{e}^{-1} &= \frac{1}{\sqrt{2}}(\mathbf{e}_x + i\mathbf{e}_y) \end{aligned} \tag{3.17}$$

The relationship between covariant and contravariant basis vectors are:

$$\mathbf{e}^{\mu}=(-1)^{\mu}\mathbf{e}_{-\mu} \qquad \mathbf{e}_{\mu}=(-1)^{\mu}\mathbf{e}^{-\mu} \qquad \mathbf{e}_{\mu}=\mathbf{e}^{-\mu *} \qquad \mathbf{e}^{\mu}=\mathbf{e}_{-\mu *} \tag{3.18}$$

with $\mu = 0, \pm 1$.

3.2.2. Euler Angles and Wigner matrices

The orientation of an object in three-dimensional space can be described by three angles (α, β, γ). The best way to define these angles in the context of NMR is to use the system called *Euler angles* [17].

A general rotation to transform a vector or matrix from one coordinate system to another

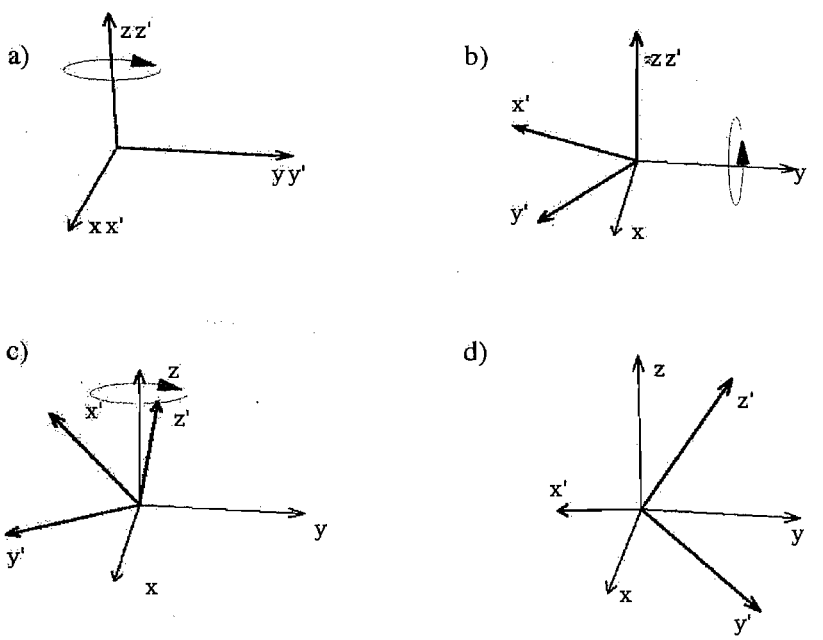

Fig. 3.2. In this figure, the frame (x, y, z) is brought into a frame (x', y', z') with an orientation described by the Euler angles (α, β, γ)=(90°, 20°, 60°) by three consecutive rotations. The rotations are through (a) 90° about the z-axis of the original frame; (b) 20° about the y-axis of the original frame, and (c) 60° about the z-axis of the original frame.

can be decomposed as the product of the three individual rotations:

$$\hat{R}(\Omega)=\hat{R}(\alpha,\beta,\gamma)=\hat{R}_z(\alpha)\hat{R}_y(\beta)\hat{R}_z(\gamma) \tag{3.19}$$

where Ω is the symbol to denote Euler angles and $\hat{R}_z(\alpha)\hat{R}_y(\beta)\hat{R}_z(\gamma)$ are rotations around z-axis with an angle γ, around y-axis with an angle β and a last rotation again around z-axis through α.

If a general rotation $\hat{R}(\alpha,\beta,\gamma)$ is applied to an object of certain rank l with m components, A_{lm} this rotation leads to a transformation into another object with the same rank $A_{lm'}$:

$$\hat{R}(\Omega)A_{l,m}=\sum_{m'=-l}^{+l} D^{l}_{mm'}(\Omega)A_{lm'} \tag{3.20}$$

where $D^{l}_{mm'}(\Omega)$ is called a *Wigner matrix element* and the complete Wigner matrix is the matrix representation of the rotation $\hat{R}(\alpha,\beta,\gamma)$. The elements of the Wigner matrix depend on the angles α, β, γ. The Wigner matrix elements can be decomposed into three separate factors, each depending on one of the Euler angles:

$$D^{l}_{mm'}(\Omega)=e^{-im\alpha}d^{l}_{mm'}(\beta)e^{-im'\gamma} \tag{3.21}$$

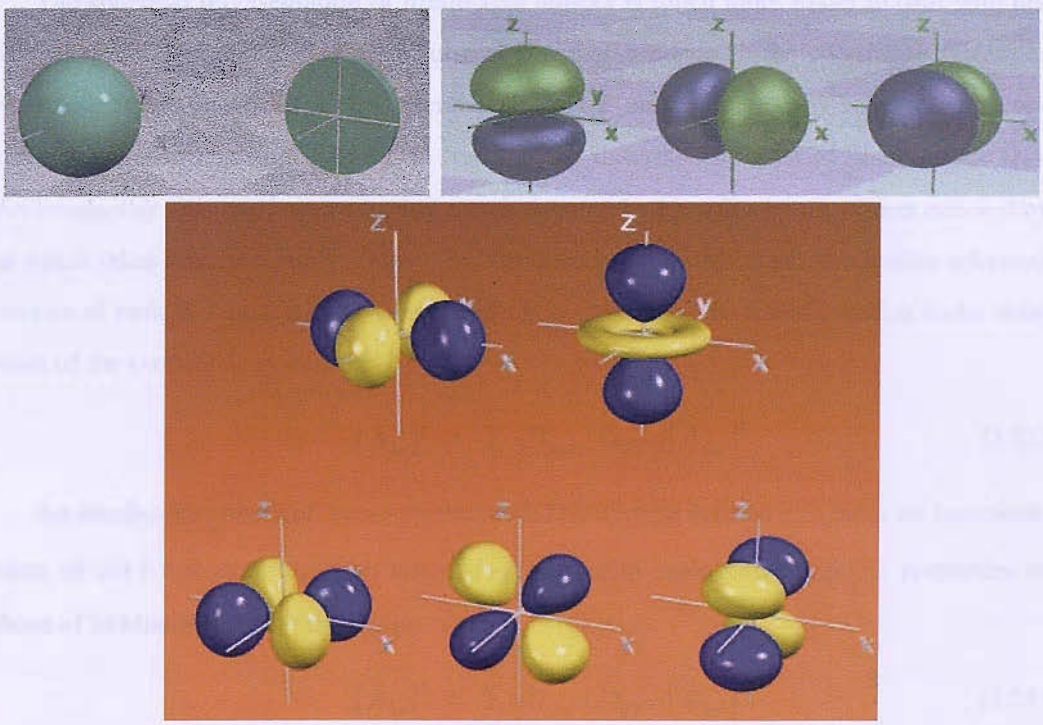

Fig. 3.3. This figure contains the graphical representation of sphericals tensor of rank-0 (a), rank-1 (b) and rank-2 (c) and their 2*l*+1 components. (From *http://winter.group.shef.ac.uk/orbitron/*).

The term $d^{l}_{mm'}(\beta)$ is called a *reduced Wigner matrix element.* The reduced Wigner matrix elements depend on the value of l.

3.2.3. Irreducible Spherical Tensors.

Spherical tensors have an important role in the modern description of NMR theory and NMR interactions. In the description of NMR phenomena, it would be convenient to use the more familiar Cartesian tensors in order to understand better the meaning of different Hamiltonian terms. However, from a mathematical point of view this is not a convenient choice because the Cartesian representation of a tensor is reducible and does not correspond to definite projection of quantum numbers, and therefore complicates the transformation under a rotational operation [17].

The Cartesian representation of tensor of second rank (A) can be decomposed into three irreducible tensors, with a total of nine components (a_{ij}). A scalar (rank-0) which is a single component equal to the trace of the tensor, an antisymmetric tensor (rank-1) having three components, and a symmetric tensor (rank-2) with trace equal to 0 and five components (Fig. 3.3).

The spherical representation of irreducible tensors is much more easier to deal with under rotational operations. The exact form of a tensor depends on the coordinate system or *reference frame* choice. If a two reference frames F and F' related by rotations are considered, the rotations from frame F to frame F' are described by a set of Euler angles $\Omega_{FF'}$. An *irreducible spherical tensor* having a rank denoted by l has $2l+1$ components denoted by m which takes integer numbers from $-l$ to l (in the context of this thesis irreducible spherical tensors of rank-0, 1 or 2 will be considered). It is defined by its transformation under rotations of the coordinate system as:

$$[A_{lm}]^{F'} = \sum_{m'=-l}^{l} D^{l}_{mm'}(\Omega_{FF'})[A_{lm'}]^{F} \tag{3.22}$$

An *irreducible spherical tensor operator (ISTO)* may be defined as a basis set representation of $2l+1$ operators $\mathcal{A}_{lm}$ with $m=(-l,-l+1,\ldots, l)$ with analogous rotational properties to those of irreducible spherical tensors:

$$[\hat{\mathcal{A}}_{lm}]^{F'} = \sum_{m'=-l}^{l} D^{l}_{mm'}(\Omega_{FF'})[\hat{\mathcal{A}}_{lm'}]^{F} \tag{3.23}$$

3.2.4. An ISTO Representation of the Spin Hamiltonian

The nuclear *spin Hamiltonian* can be written as a summation of different spin interactions Λ:

$$\hat{\mathcal{H}}_{spin}=\sum_{\Lambda}\hat{\mathcal{H}}^{\Lambda}_{spin} \tag{3.24}$$

In the Cartesian basis the spin Hamiltonian for an interaction Λ may be represented as [18]:

$$\hat{\mathcal{H}}^{\Lambda}_{spin}=C^{\Lambda}\mathbf{X}\cdot\mathrm{A}^{\Lambda}\cdot\mathbf{Y} \tag{3.25}$$

where $\mathbf{X}$ and $\mathbf{Y}$ are vector operators, C^{Λ} is a coefficient which depends on the spin interactions and A^{Λ} is a rank-2 tensor that depends on the interaction Λ and contains the dependence on spatial orientation.

The spin Hamiltonian of an interaction Λ can equivalently be expressed in terms of irreducible spherical tensor operators as scalar products of two irreducible spherical tensor operators [19], [20]:

$$\hat{\mathcal{H}}^{\Lambda}_{spin}=C^{\Lambda}\sum_{l}\sum_{m=-l}^{l}(-1)^{m}[\mathcal{A}^{\Lambda}_{lm}]^{F}[\mathcal{T}^{\Lambda}_{l-m}]^{F} \tag{3.26}$$

The spherical tensor representation of the spin Hamiltonian separates the *spatial tensor* $[\mathcal{A}^{\Lambda}_{l}]$ and the *spin-field tensor* $[\mathcal{T}^{\Lambda}_{l}]$. In appendix A, the form of the spatial and the spin-field of each spin interaction is given.

The spin-field tensor is composed of a spin and a field part. Normally, the field is an static external magnetic field and not subject to rotations. However the spin part can be rotated by external r.f. fields. Therefore, the internal Hamiltonian will no longer be written in terms of components $[\mathcal{T}^{\Lambda}_{l}]$ of the spin but in terms of pure irreducible spherical spin tensors $[T^{\Lambda}_{\lambda}]$ of rank λ. In this case, the rank is not the same for the spatial and spin tensors. In addition, a spatial tensor $[A^{\Lambda}_{\lambda}]$ can be defined, which is related to the spatial tensor $[\mathcal{A}^{\Lambda}_{l}]$ by numerical factors. The forms of these two tensors is given in appendix A.

At this point is useful to clarify the notation used, since this notation will be used from now on in the discussion of this thesis. Quantum numbers l, m, λ, μ summarize the transformation of the Hamiltonian under rotations: l is the spatial rotational rank and λ is the rank with respect to rotations of the spin polarization. The component indices m and μ take values $m = -l,-l+1,...,+l$ and $\mu = -\lambda,\lambda+1,...,+\lambda$.

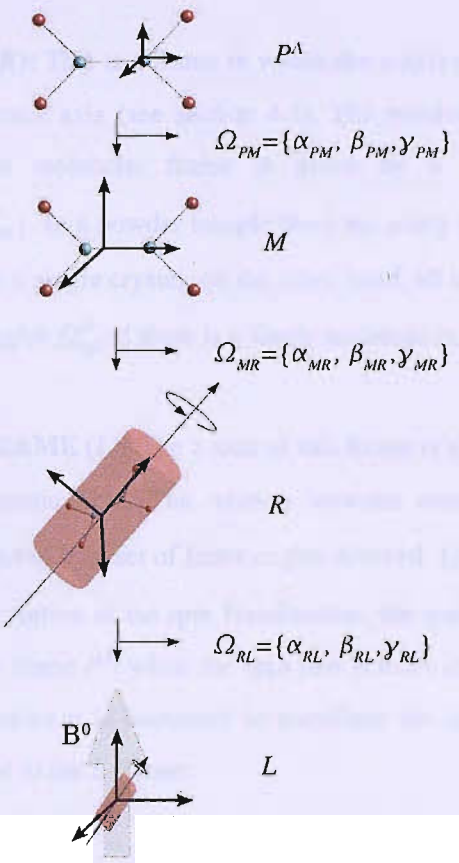

Fig. 3.4. The different reference frames used in NMR and their relative orientations given by the Euler angles.

3.3. Reference Frame Transformations

The exact form of a spherical tensor depends on the reference frame chosen to express it. In this section the common reference frames used in solid-state NMR will be defined and described.

1. **PRINCIPAL AXIS SYSTEM (PAS or P^{Λ}):** The principal axis system P^{Λ} of a spin interaction Λ is defined as the reference frame in which the tensor that describes the spin interaction is diagonal. Each interaction has its own PAS.

2. **MOLECULAR FRAME (M):** This is the system used to describe the molecular orientation and is chosen arbitrarily. The PAS frames for each interaction is related to the common M frame by a set of Euler angles, $\Omega_{PM}^{\Lambda}=\{\alpha_{PM}^{\Lambda}, \beta_{PM}^{\Lambda}, \gamma_{PM}^{\Lambda}\}$. A set of these Euler angles gives the orientation of a spin interaction with respect to the molecular structure.

3. **ROTOR FRAME (*R*):** This is a frame in which the z-axis direction of this frame coincides with the rotor axis (see section 4.1). The relative orientation between this frame and the molecular frame is given by a set of Euler angles $\Omega_{MR}^{\Lambda}=\{\alpha_{MR}^{\Lambda},\beta_{MR}^{\Lambda},\gamma_{MR}^{\Lambda}\}$. In a powder sample there are many Euler angles Ω_{MR}^{Λ} randomly distributed. In a single crystal, on the other hand, all the molecules have the same set of Euler angles Ω_{MR}^{Λ} if there is a single molecule in the unit cell.

4. **LABORATORY FRAME (*L*):** The z-axis of this frame is aligned in the direction of the external magnetic field. The relation between rotor orientation and the laboratory frame is given by a set of Euler angles denoted $\Omega_{RL}^{\Lambda}=\{\alpha_{RL}^{\Lambda},\beta_{RL}^{\Lambda},\gamma_{RL}^{\Lambda}\}$.

In the spherical tensor description of the spin Hamiltonian, the spatial tensor is normally expressed in the principal axis frame P^{Λ}, while the spin part is more conveniently expressed in the laboratory frame. Therefore it is necessary to transform the spatial part of the spin Hamiltonian from the P^{Λ} frame to the L frame:

$$[\mathcal{A}_{lm}^{\Lambda}]^{L}=\sum_{m'=-l}^{l}D_{mm'}^{l}(\Omega_{PL}^{\Lambda})[\mathcal{A}_{lm'}^{\Lambda}]^{P} \tag{3.27}$$

where Ω_{PL}^{Λ} is the set of Euler angles relating the P and L frames. The equation (Eq. (3.26)) for the spin Hamiltonian of an interaction Λ becomes:

$$\hat{\mathcal{H}}_{spin}^{\Lambda}=C^{\Lambda}\sum_{l}\sum_{\lambda}\sum_{m,m'=-l}^{l}\sum_{\mu=-\lambda}^{\lambda}(-1)^{m}[\mathcal{A}_{lm'}^{\Lambda}]^{P}D_{mm'}^{l}(\Omega_{PL}^{\Lambda})[\mathcal{T}_{\lambda\mu}^{\Lambda}]^{L} \tag{3.28}$$

3.4. External Spin Interactions

In general, an NMR experiment involves an external static field magnetic field and transverse r.f. fields that are generated by the spectrometer and controlled externally. The external spin Hamiltonian may be written as:

$$\hat{\mathcal{H}}_{spin}^{ext}=\hat{\mathcal{H}}_{j}^{Z}+\hat{\mathcal{H}}_{j}^{RF}(t) \tag{3.29}$$

where the first term of Eq. (3.29) is the interaction of the spin system with a strong longitudinal static field denoted by $\mathbf{B}^{0}$ and the second is the interaction with a transverse oscillating radio frequency (r.f.) $\mathbf{B}_{\mathbf{RF}}$ generated by a coil.

3.4.1. Zeeman interaction

Considering a spin ensemble of isolated spins of the same type placed in a strong static magnetic field, the interaction between the spin nuclear magnetic moment and the static field $\mathbf{B}^0$ is called the *Zeeman interaction*. The static field breaks the degeneracy of the spin states and induces a preferential orientation of the nuclear spin along the z-axis of the L frame. This situation corresponds to unequally populated energy levels.

The strong static field along the z-direction of the laboratory frame is written as follows:

$$\mathbf{B}^0 = B^0 \mathbf{e}_z \tag{3.30}$$

The spin Hamiltonian of the Zeeman interaction for an I-spin labelled j can be written as:

$$\hat{\mathcal{H}}_j^Z = -\mu_I^j \cdot \mathbf{B}^0 = -\gamma_I^j \hat{\mathbf{I}}_j \mathbf{B}^0 = -\gamma_I^j B^0 \hat{I}_{jz} = \omega_0 \hat{I}_{jz} \tag{3.31}$$

where γ_I is the gyromagnetic ratio, I_{jz} is the z-component of the spin operator, $\mathbf{B}^0$ is the magnetic field along the z-direction and ω_0 is the Larmor frequency which is equal to the different in energy between two spin levels:

$$\omega_0 = -\gamma B^0 \tag{3.32}$$

The Zeeman Hamiltonian may be written in terms of ISTOs as follows:

$$\hat{\mathcal{H}}_j^Z = [A_{00}^Z] T_{10}^j = \omega_0 T_{10}^j \tag{3.33}$$

3.4.2. High-Field Approximation

Since the Zeeman Hamiltonian is much larger than the other spin interactions, it is possible, as a very good approximation, to ignore all the non-secular components of the spin interactions.

In terms of quantum mechanics, it is possible to treat the internal Hamiltonian as a perturbation of the Zeeman Hamiltonian [15]. This interaction Hamiltonian can be decomposed into commuting terms and non-commuting terms, with the matrix representation of this interaction contains diagonal (commuting terms) and off-diagonal terms (non-commuting terms). In the case of the *high-field approximation* or *secular approximation* only commuting terms (diagonal terms) are taken into account in order to calculate the energy levels. In terms of spherical tensors, this corresponds to the selection of the spin operators of the form $[T_{\lambda 0}^A]^L$. Non-commuting terms produce small perturbations of the NMR spectrum called *dynamic frequency shifts* [21]. These effects are very small and they are ignored in this thesis.

3.4.3. Interaction with a Radio-Frequency Field

In general, it is almost impossible to observe an NMR signal using the longitudinal spin magnetization along z-axis of L frame in the usual conditions (see [22] for a way of detection of longitudinal magnetization). The transverse magnetization is detected after a rotation of the magnetization of 90 degrees using a r.f pulse. The majority of modern NMR experiments involve multiple rotations and energy transitions in the spin system through r.f. pulses. In general the NMR spectrometer generates a r.f. field $\mathbf{B}_{RF}$ using a r.f. coil along the x-axis of the laboratory frame. This r.f. field is broken down into pulses that oscillate at the reference frequency ω_{ref}. A perfect rectangular pulse has the form:

$$\mathbf{B}_{RF}(t)=\begin{cases} B_{RF}\cos(\omega_{ref}t+\phi_p)\mathbf{e}_x & \text{during an r.f. pulse} \\ 0 & \text{otherwise} \end{cases} \tag{3.34}$$

where the amplitude of the r.f. pulse is denoted by B_{RF}, and ϕ_p is the phase of the pulse. This oscillatory field can be decomposed into two *rotating components* with the same frequency but opposite sign of rotation. The component that rotates in the same sense as the spin precession is called the *resonant component* of the r.f. field. The component rotating in the opposite sense to the Larmor frequency is the *non-resonant* r.f. field component. As an excellent approximation, if $\omega_{ref}\approx\omega_0$, only the resonant part has an important influence on the nuclear spin.

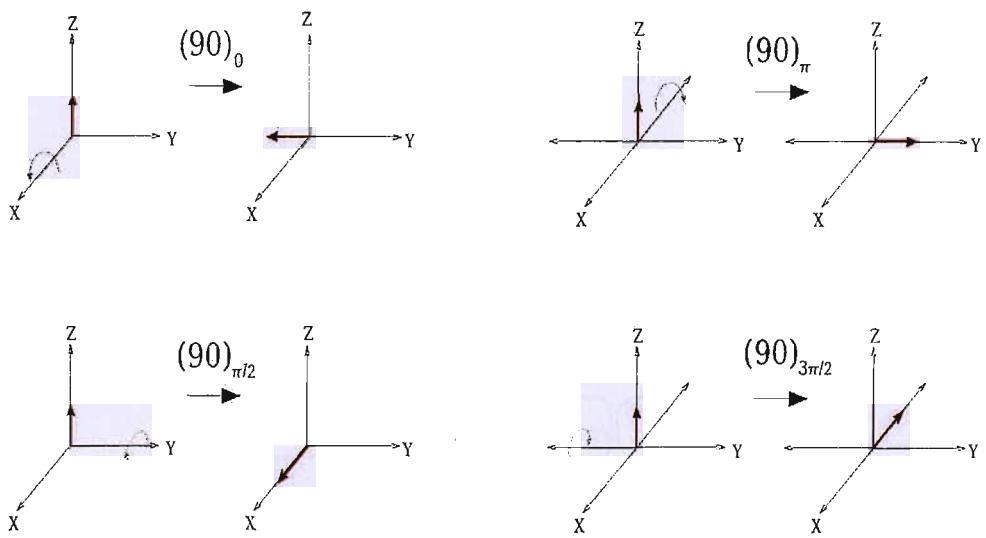

Fig. 3.5. A vectorial representation of the effect of four 90^0 pulses with phases 0, $\pi/2$, π and $3\pi/2$. In the NMR jargon these four pulses are known as "x-pulse", "y-pulse", "-x-pulse" and "-y-pulse", respectively.

The Hamiltonian resulting from the interaction between the resonant component of the r.f. field and the nuclear spin is:

$$\hat{\mathcal{H}}_j^{RF}(t)=-\frac{1}{2}\gamma_I^j B_{RF}\{\cos(\omega_{ref}t+\phi_p)\hat{I}_{jz}+\sin(\omega_{ref}t+\phi_p)\hat{I}_{jy}\} \qquad (3.35)$$

It is useful to visualize the situation in a *rotating frame of reference*. The description in this frame is useful because of the time-dependence of the Hamiltonian. The rotating frame is a coordinate system in which the z-axis coincides with the z-axis of laboratory frame L but the x-axis and y-axis rotate in the same direction and with the same frequency of the resonant component as the r.f. field B_{RF}.

The r.f. Hamiltonian expressed in the rotating frame becomes:

$$\hat{\mathcal{H}}_j^{RF}=\omega_{nut}^j(\hat{I}_{jx}\cos\phi_p+\hat{I}_{jy}\sin\phi_p) \qquad (3.36)$$

where ω_{nut}^j is called *nutation frequency* of the r.f. field:

$$\omega_{nut}^j=\frac{1}{2}|\gamma_I^j B_{RF}| \qquad (3.37)$$

The r.f. pulse is characterized by a *flip angle* β and a phase ϕ_p The flip angle is the angle by which the spin polarization is rotated by the pulse:

$$\beta_p=\omega_{nut}\tau_p \qquad (3.38)$$

where τ_p is the duration of the pulse. Short and strong pulses excite a wide range of frequencies while weak and long pulses are more frequency-selective. Fig. 3.5 shows different rep-

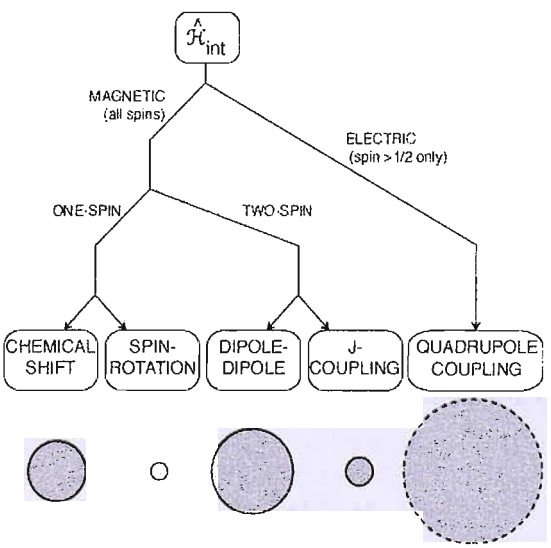

Fig. 3.6. The internal spin interactions and their relative size (From [6]).

resentations of an r.f. pulse and a vectorial representation of the effect of an r.f. pulse on the spin magnetization of an isolated spin in a strong static magnetic field.

3.5. Internal Spin Interactions

The nuclei are surrounded by magnetic and electric fields originating from the molecular environment. The nuclear interaction of a spin with these fields is expressed as a internal Hamiltonian $\hat{\mathcal{H}}_{spin}^{int}$ [6]. This internal Hamiltonian in diamagnetic solids contains the following terms: *chemical shift interaction, direct dipole-dipole couplings, J-couplings and the quadrupolar interaction.*

$$\hat{\mathcal{H}}_j^{int} = \hat{\mathcal{H}}_j^{CS} + \hat{\mathcal{H}}_{ij}^{DD} + \hat{\mathcal{H}}_{ij}^{J} + \hat{\mathcal{H}}_j^{Q} \tag{3.39}$$

The quadrupolar interaction, which is an interaction with an electric field, only appears for nuclei with spin >1/2. Fig. 3.6 shows the different interactions described in this thesis and their relative size.

3.5.1. Chemical Shift

The strong static field $\mathbf{B}^0$ induces *currents* in the clouds of electrons surrounding the nuclei. The circulation of this current produces an *induced magnetic field* $B_{induced}^{j}$ which is added to the main field to produce a *local magnetic field* that causes a shift in the Larmor frequency. The new Larmor frequency is called *the chemically shifted Larmor frequency* [6]:

$$\mathbf{B}_{local}^{j} = \mathbf{B}^0 + \mathbf{B}_{induced}^{j} \tag{3.40}$$

The induced magnetic field depends on the electronic distribution surrounding the nucleus and the main magnetic field $\mathbf{B}^0$.

$$\mathbf{B}_{induced}^{j} = \delta^j \mathbf{B}^0 \tag{3.41}$$

where δ^j is the *chemical shift tensor* (CS) of the spin *j* following the *deshielding convention* (other conventions can be used [23], [24]). This tensor is a rank-2 Cartesian tensor represented by a 3×3 matrix.

$$\delta^j = \begin{vmatrix} \delta_{xx}^j & \delta_{xy}^j & \delta_{xz}^j \\ \delta_{yx}^j & \delta_{yy}^j & \delta_{yz}^j \\ \delta_{zx}^j & \delta_{zy}^j & \delta_{zz}^j \end{vmatrix} \tag{3.42}$$

The induced magnetic field in a matrix form is:

$$\begin{pmatrix} B^{j,x}_{induced} \\ B^{j,y}_{induced} \\ B^{j,z}_{induced} \end{pmatrix} = \begin{pmatrix} \delta^j_{xx} & \delta^j_{xy} & \delta^j_{xz} \\ \delta^j_{yx} & \delta^j_{yy} & \delta^j_{yz} \\ \delta^j_{zx} & \delta^j_{zy} & \delta^j_{zz} \end{pmatrix} \cdot \begin{pmatrix} 0 \\ 0 \\ B^0 \end{pmatrix} \tag{3.43}$$

$$\begin{pmatrix} B^{j,x}_{induced} \\ B^{j,y}_{induced} \\ B^{j,z}_{induced} \end{pmatrix} = \begin{pmatrix} \delta^j_{xz} B^0 \\ \delta^j_{yz} B^0 \\ \delta^j_{zz} B^0 \end{pmatrix} \tag{3.44}$$

Since the electronic distribution is not spherical around the nuclei, the induced magnetic field has a component not only along the z-direction of the *L* frame but also along the x-direction and the y-direction.

The CS tensor may be decomposed to three irreducible tensors:

$$\delta^j = \delta^j_{iso} + \delta^j_{asymm} + \delta^j_{aniso} \tag{3.45}$$

- A rank-0 tensor δ_{iso}, called the *isotropic chemical shift*. This tensor is equal to the

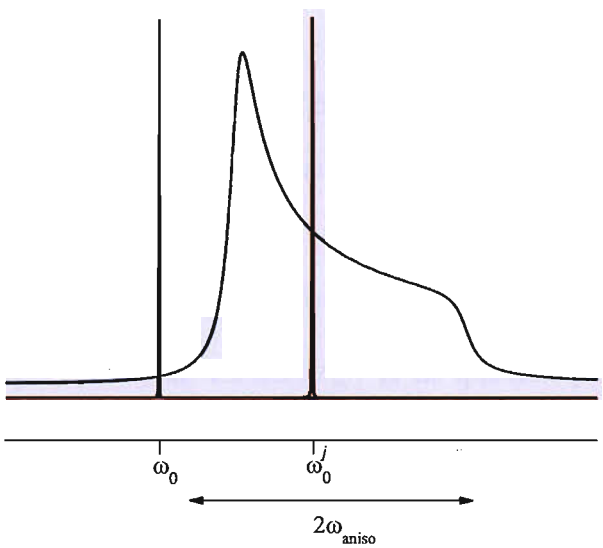

Fig. 3.7. The figure shows simulated NMR spectrum lineshapes of a single ^{13}C nucleus in a powder sample at a main magnetic field of 400 MHz. In the spectrum shown by the black line, the isoCS and the CSA are equal to 0 and the spectrum shows a single line at the Larmor frequency. If the isotropic chemical shift is introduced, the spectrum shows a single peak but at the chemically shifted Larmor frequency (red line). The blue line represents the powder spectrum when the CSA is introduced. In this case, the spectrum shows the characteristic powder lineshape for $\eta = 0$.

trace of the CS tensor and is a scalar:

$$\delta_{iso}^{j}=\frac{1}{3}Tr(\delta^{j})=\frac{1}{3}(\delta_{xx}^{j}+\delta_{yy}^{j}+\delta_{zz}^{j}) \tag{3.46}$$

- A rank-1 tensor. This tensor can be ignored under the high field approximation because it has no secular part.
- A rank-2 tensor, called the *chemical shift anisotropy* (CSA). This part of the CS gives useful information about the geometry and the orientation of the electronic distribution around the nucleus. The three diagonal elements of the CSA are called the *principal values of the CSA tensor* and they are denoted by δ_{xx}^{P}, δ_{yy}^{P}, δ_{zz}^{P}. By convention [25], the three principal values are ordered as follow:

$$\delta_{zz}^{P}-\delta_{iso}^{j}\geqslant\delta_{xx}^{P}-\delta_{iso}^{j}\geqslant\delta_{yy}^{P}-\delta_{iso}^{j} \tag{3.47}$$

Two useful parameters to describe the CSA are the anisotropy of the anisotropic chemical shift frequency ω_{aniso} and the biaxiality parameter η:

$$\omega_{aniso}=\omega_{0}\Delta_{aniso}^{j}=\omega_{0}(\delta_{zz}^{P}-\delta_{iso}^{j}) \tag{3.48}$$

$$\eta=\frac{\delta_{yy}^{P}-\delta_{xx}^{j}}{\delta_{zz}^{P}-\delta_{iso}^{j}} \tag{3.49}$$

The CS Hamiltonian can be expressed as:

$$\hat{\mathcal{H}}_{j}^{CS}=-\mu_{I}^{j}\cdot\mathbf{B}_{induced}^{j}=-\gamma_{I}^{j}\delta^{j}\mathbf{B}^{0}\hat{\mathbf{I}}=-\gamma_{I}^{j}\mathbf{B}^{0}\hat{\mathbf{I}}(\delta_{iso}^{j}+\delta_{aniso}^{j}) \tag{3.50}$$

Normally the Zeeman and CS Hamiltonians are expressed together. This Hamiltonian expressed in terms of ISTOs becomes:

$$\hat{\mathcal{H}}_{j}^{CS}=\sum_{l}\sum_{m=-l}^{l}(-1)^{m}[\mathcal{A}_{lm}^{CS}]^{P}[\mathcal{T}_{l\,m}^{CS}]^{L} \tag{3.51}$$

where $[\mathcal{A}_{lm}^{CS}]^{P}$ is the space part of the CS and $[\mathcal{T}_{lm}^{CS}]^{L}$ is the spin-field part (this part contains information about the spin and the field) of the CS. If the high-field approximation is applied Eq. (3.51) is equal to:

$$\hat{\mathcal{H}}_{j}^{CS}=\sum_{l}\sum_{\lambda}[A_{l0}^{CS}]^{P}[T_{\lambda 0}^{CS}]^{L} \tag{3.52}$$

The spin-field and space parts have the components shown in Appendix A, and can be rearranged to give the following an expression for the CS Hamiltonian:

$$\hat{\mathcal{H}}_{j}^{CS}=\omega_{0}^{j}[T_{1\,0}^{j}]^{L}+[A_{20}^{CS}]^{P}[T_{20}^{CS}]^{L} \tag{3.53}$$

In order to express the space part in the laboratory frame, we need a transformation from L to P, accomplished via the intermediate rotor frame R:

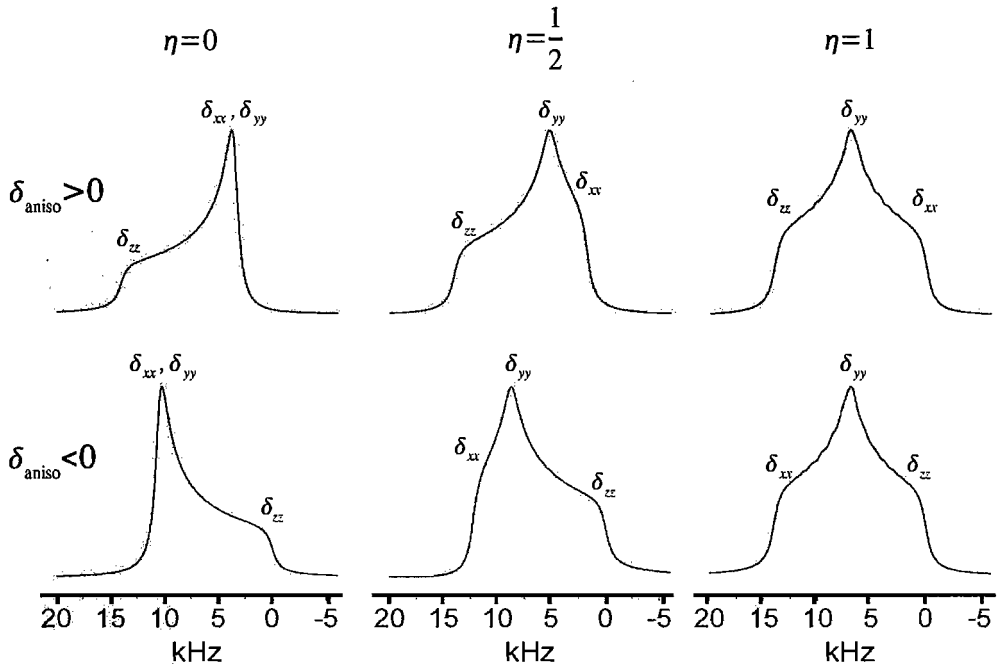

Fig. 3.8. Powder patterns observed in static solid-state NMR spectra.

$$[A_{20}^{CS}]^L = \sum_{m=-2}^{2} \sum_{m'=-2}^{2} [A_{2m'}^{CS}]^P D_{m'm}^2(\Omega_{PR}^{CS}(t)) D_{m0}^2(\Omega_{RL}^{CS}) \tag{3.54}$$

The Hamiltonian for CS including the Zeeman interaction and taking into account the reference frame transformations is:

$$\hat{\mathcal{H}}_j^{CS} = \omega_0^j [T_{10}^j]^L + \sum_{m=-2}^{2} \sum_{m'=-2}^{2} \omega_{aniso} [A_{2m'}^{CS}]^P D_{m'm}^2(\Omega_{PR}^{CS}(t)) D_{m0}^2(\Omega_{RL}^{CS}) [T_{10}^j]^L \tag{3.55}$$

where ω_0^j is the *chemically shifted Larmor frequency* and $[A_{2m}^{CS}]^P$ is a second-rank tensor.

The CS is an important interaction for the application of NMR to chemistry because of its dependence on the electronic environment of the nucleus. It is indispensable in study of the spectral assignment of spin sites [26], molecular orientation [13], [27] and mobility of molecular groups [24], [28].

3.5.2. Direct Dipolar-Dipolar couplings

A nuclear spin itself generates a magnetic field that can interact with other nuclear spins. Since this interaction is mutual the first spin also interacts with the magnetic field generated by the second spin.

This interactions between spins is propagated through the space between them, and is therefore called *the through-space dipole-dipole coupling*. Other names are the *direct di-*

pole-dipole coupling, the dipole-dipole coupling or *the DD-coupling*.

In the Cartesian basis the Hamiltonian of the dipole-dipole coupling between two spins I_i and I_j can be expressed as:

$$\hat{\mathcal{H}}_{ij}^{DD} = \mathbf{I}_i \mathbb{D} \mathbf{I}_j \tag{3.56}$$

where $\mathbb{D}$ is an axially symmetric Cartesian tensor with zero trace [19]. This interaction is analogous to the interaction between two magnetic dipoles:

$$\hat{\mathcal{H}}_{ij}^{DD} = b_{ij}(3(\hat{\mathbf{I}}_i \cdot \mathbf{e}_{ij})(\hat{\mathbf{I}}_j \cdot \mathbf{e}_{ij}) - \hat{\mathbf{I}}_i \cdot \hat{\mathbf{I}}_j) \tag{3.57}$$

where $\mathbf{e}_{ij}$ is a unit vector parallel to the internuclear axis between the two nuclei.

With the high-field approximation the homonuclear dipole-dipole Hamiltonian is:

$$\begin{aligned} \hat{\mathcal{H}}_{ij}^{DD} &= b_{ij}\tfrac{1}{2}(3\cos^2\Theta_{ij} - 1)(3\hat{I}_{iz}\hat{I}_{jz} - \hat{\mathbf{I}}_i \cdot \hat{\mathbf{I}}_j) \\ &= b_{ij}\tfrac{1}{2}(3\cos^2\Theta_{ij} - 1)(2\hat{I}_{iz}\hat{I}_{jz} - \tfrac{1}{2}(\hat{I}_i^- \hat{I}_j^+ + \hat{I}_i^+ \hat{I}_j^-)) \end{aligned} \tag{3.58}$$

where $\frac{1}{2}(\hat{I}_i^- \hat{I}_j^+ + \hat{I}_i^+ \hat{I}_j^-)$ is called the *"flip-flop" term,* which is of importance in the measurement of distances in *homonuclear multiple-spin systems* (chapter 8), Θ_{ij} is the angle between the dipolar vector and the static field and b_{ij} is the *dipole-dipole coupling constant*:

$$b_{ij} = -\frac{\mu_0}{4\pi}\frac{(\gamma_I^j)^2\hbar}{r_{ij}^3} \text{ for homonuclear spins} \tag{3.59}$$

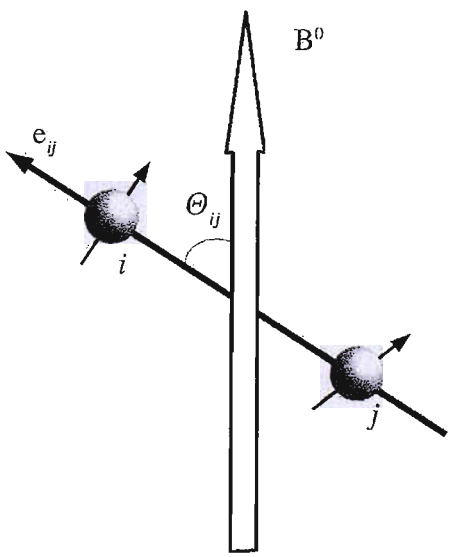

Fig. 3.9. Angle Θ_{ij} between the static magnetic field B^0 and the internuclear vector $\mathbf{e}_{ij}$ between the spins I_i and I_j.

where γ_I and γ_S are the gyromagnetic ratios of spins I and S and r_{ij} is the distance between two spins. The interaction is scaled by the gyromagnetic ratio of the nuclei involved in the interaction and depends on the inverse cube of the distance. This property is extremely important for extracting distance and geometrical information from solid-state NMR experiments [29]. It is important to note that the Hamiltonian of the dipolar interaction depends on the orientation, but the dipole-dipole coupling constant is invariant under a change of orientation [6].

In the high-field approximation, the dipole-dipole Hamiltonian in the laboratory frame can be written in terms of spherical tensors operators as:

$$\hat{\mathcal{H}}_{jk}^{DD}=[A_{20}^{DD}]^L[T_{20}^{DD}]^L \tag{3.61}$$

where the first term is the spatial part, which depends on the angle Θ and the second term is the spin part (see Appendix A and [30]).

In the case of heteronuclear spin system the Hamiltonian the flip-flop term disappears in the high-field approximation and the expression can be written as:

$$\hat{\mathcal{H}}_{jk}^{DD}=b_{ij}(1-3\cos^2\Theta_{ij})I_{iz}S_{jz}=[A_{20}^{DD_{IS}}]^L[T_{10}^{I_i}]^L[T_{10}^{S_j}]^L \tag{3.62}$$

3.5.3. *J*-couplings

In a molecule in which different atoms are chemically bonded, the nuclear spins of these bonded atoms are also coupled by the influence of the bonding electrons. This through-bond interaction is called the indirect *spin-spin coupling*, *J-coupling*, or *indirect dipole-dipole coupling*. This is an important interaction for the determination of chemical structure and study of bonding between two atoms [31], [32], [33].

The Hamiltonian for a *J*-coupling interaction between spins i and j is expressed as:

$$\hat{\mathcal{H}}_{ij}^{J}=\mathbf{I}_i\mathbb{J}\mathbf{I}_j \tag{3.63}$$

where $\mathbb{J}$ is a Cartesian tensor of rank-2 and $\mathbf{I}_i$ and $\mathbf{I}_j$ are are the spin operators for spins i and j. The tensor $\mathbb{J}$ can be decomposed into irreducible tensors of rank-0, rank-1 and rank-2:

$$\mathbb{J}=J^{(0)}+J^{(1)}+J^{(2)} \tag{3.64}$$

where $J^{(0)}$ is the isotropic part of the *J*-coupling. The Hamiltonian of the isotropic part of the *J*-coupling is given by:

$$\hat{\mathcal{H}}_{ij}^{J_{iso}}=2\pi J_{ij}\mathbf{I}_i\cdot\mathbf{I}_j \tag{3.65}$$

where J_{ij} is the homonuclear *isotropic J-coupling* constant in Hz. The tensor $J^{(1)}$ is the anti-symmetric *J*-coupling which may be ignored to first order [19]. The tensor $J^{(2)}$ is a rank-2 tensor and represents the orientation dependence of the *J*-coupling which is difficult to observe because the irreducible tensor for the anisotropic part of the J-coupling has the same form and behaviour under rotations as the usually much larger dipole-dipole coupling [6], [30].

The Hamiltonian for the isotropic *J*-coupling in terms of irreducible spherical tensors can be written as (see Appendix A):

$$\hat{\mathcal{H}}_{ij}^{J_{iso}}=[A_{00}^{J}]^{L}[T_{00}^{jk}]^{L} \tag{3.66}$$

3.5.4. Quadrupolar Interactions

The quadrupolar interaction for spin *j* can be expressed as:

$$\hat{\mathcal{H}}_{j}^{Q}=\mathbf{I_j}\mathbb{Q}\mathbf{I_j} \tag{3.67}$$

where $\mathbb{Q}$ is the quadrupolar tensor. The Hamiltonian under the high-field approximation is:

$$\hat{\mathcal{H}}_{j}^{Q}=\omega_{Q}^{j}(3I_{jz}^{2}-\mathbf{I_j}\cdot\mathbf{I_j}) \tag{3.68}$$

where ω_{Q}^{j} is the nuclear quadrupolar frequency. In some cases, the high-field approximation is not applicable to the quadrupolar Hamiltonian. For further reading about NMR of quadrupolar nuclei see [34], [35], [36] and [37].

3.6. Density Operators

In section 3.1 the Zeeman eigenstates for a spin-½ have been defined. However the possible states for a spin-½ are not restricted to the Zeeman eigenstates, and include superpositions of the Zeeman states:

$$|\psi(t)\rangle=C_{\alpha}(t)|\alpha\rangle+C_{\beta}(t)|\beta\rangle \tag{3.69}$$

where C_{α} and C_{β} are complex numbers called *superposition coefficients* which must satisfy the normalization condition:

$$C_{\alpha}{}^{2}+C_{\beta}{}^{2}=1 \tag{3.70}$$

In a sample composed by an ensemble of spins, the total magnetization is the sum of each small contribution of each individual spin as described above. In practice, this calculation is impossible due to the enormous number of spins contained in a real sample.

However, there is an alternative formalism, called the *density operator*, which overcomes this problem and provides an elegant tool to calculate an overall spin state for a *spin ensemble.*

Consider an ensemble of N spins in superposition states $|\psi_k(t)\rangle$. The expectation value of an operator $\hat{Q}$ over the spin ensemble is given by:

$$\overline{\langle \hat{Q}_{obs} \rangle} = \sum_{k=1}^{N} \langle \psi_k(t) | \hat{Q} | \psi_k(t) \rangle \tag{3.71}$$

This expression can be written as:

$$\begin{aligned} \overline{\langle \hat{Q}_{obs} \rangle} &= \mathrm{Tr}\{ \sum_{k=1}^{N} |\psi_k(t)\rangle\langle\psi_k(t)| \hat{Q} \} \\ &= \mathrm{Tr}\{ (\ \ _1(t)\rangle\langle\ \ _1(t) + \ \ _2(t)\rangle\langle\ \ _2(t) + \cdots + \ \ _N(t)\rangle\langle\ \ _N(t)\ ) \hat{Q} \} \end{aligned} \tag{3.72}$$

where the overbar indicates the average outcome of many measurements [6].

It is possible to define the density operator $\hat{\rho}(t)$ as :

$$\begin{aligned} \hat{\rho}(t) &= \overline{|\psi_k(t)\rangle\langle\psi_k(t)|} \\ &= \mathbb{N}^{-1} (\ \ _1(t)\rangle\langle\ \ _1(t) + \ \ _2(t)\rangle\langle\ \ _2(t) + \cdots + \ \ _N(t)\rangle\langle\ \ _N(t)\ ) \end{aligned} \tag{3.73}$$

where the overbar indicates an average over the ensemble of N spins. Then, the macroscopic observation of $\hat{Q}$ for the entire ensemble is equal to:

$$\overline{\langle \hat{Q} \rangle} = \mathrm{Tr}\{ \hat{\rho}(t) \hat{Q} \} \tag{3.74}$$

The density operator in the Zeeman basis can be written [30] as:

$$\hat{\rho}(t) = \sum_{r,s} \rho_{rs}(t) |r\rangle\langle s| \tag{3.75}$$

The representation of the density operator has diagonal elements $\rho_{rr}(t)$ which are the *populations* and $\rho_{rs}(t)$ which are the *coherences* between states $|r\rangle$ and $|s\rangle$.

If the spin states $|r\rangle$ and $|s\rangle$ are eigenstates of $\hat{I}_z$ with eigenvalues equal to M_s and M_r, then the order of the coherence between eigenstates $|r\rangle$ and $|s\rangle$ is:

$$p_{rs} = M_r - M_s \tag{3.76}$$

Consider an ensemble of spins I which it is left undisturbed in a strong magnetic field. In this situation, after a time the system adopts a state called *thermal equilibrium.* The thermal equilibrium density operator of the system at temperature T expressed as:

$$\hat{\rho}_{eq} = \frac{\exp\{-\hbar \hat{\mathcal{H}}_I^Z / k_B T\}}{\mathrm{Tr}\{\exp\{-\hbar \hat{\mathcal{H}}_I^Z / k_B T\}\}} \tag{3.77}$$

where k_B is the *Boltzmann constant*. Considering the high-temperature approximation ($k_B T$

$\gg |\hbar\omega_0|$) the expression for the density operator can be simplified as :

$$\hat{\rho}_{eq} \simeq \frac{1}{2}(\hat{1} + \mathbb{B}\hat{I}_z) \tag{3.78}$$

where $\mathbb{B}$ is the *Boltzmann factor*:

$$\mathbb{B} = \frac{\hbar\gamma_I B_0}{k_B T} \tag{3.79}$$

In practice, the only term to use in calculations is $\hat{I}_z$ since the unity operator is constant.

3.7. Time Evolution

The evolution of the density operator under the effect of a Hamiltonian is determined by the *Liouville-von Neumann equation*:

$$\frac{d}{dt}\hat{\rho}(t) = -i[\hat{\mathcal{H}}(t), \hat{\rho}(t)] \tag{3.80}$$

Solving this differential equation for a known initial density operator $\hat{\rho}(t_0)$ of the spin ensemble at time point t_0, the density operator $\hat{\rho}(t)$ at time t gives:

$$\hat{\rho}(t) = \hat{U}(t, t_0)\hat{\rho}(t_0)\hat{U}^{\dagger}(t, t_0) \tag{3.81}$$

where the operator $\hat{U}(t, t_0)$ is known as the *propagator* which solves the equation:

$$\frac{d}{dt}\hat{U}(t, t_0) = -i\hat{\mathcal{H}}(t)\hat{U}(t, t_0) \tag{3.82}$$

In order to determine the propagator operator, two cases can be considered:

1. If the Hamiltonian $\hat{\mathcal{H}}$ is time-independent, Eq. (3.82) can be easily integrated and the propagator is described by:

$$\hat{U}(t, t_0) = \exp\{-i\hat{\mathcal{H}}(t - t_0)\} \tag{3.83}$$

2. If the Hamiltonian is time-dependent the propagator can be represented as:

$$\hat{U}(t, t_0) = \hat{T}\exp\{-i\int_{t_0}^{t} dt'\hat{\mathcal{H}}(t')\} \tag{3.84}$$

where $\hat{T}$ is the Dyson operator [30], [16], [25].

3.8. Average Hamiltonian Theory

In the previous section the way to calculate propagators has been given when the

Hamiltonian is time-dependent. In general solving Eq. (3.82) is difficult and an analytical solution for $\hat{U}(t,t_0)$ cannot be obtained. The *Average Hamiltonian Theory* (AHT) [25], [38] allows one to obtain an approximate solution for the propagator.

AHT assumes that the time-dependent Hamiltonian $\hat{\mathcal{H}}(t)$ under the effective evolution during a time interval t_c can be described by an effective average Hamiltonian $\bar{\mathcal{H}}$. This is possible if:

- The Hamiltonian is periodic.
- The observations are stroboscopic and synchronized with the period of the Hamiltonian.

Thus, the propagator $\hat{U}(t,t_0)$ can be written as:

$$\hat{U}(t,t_0)=\hat{T}\exp\{-i\int_{t_0}^{t}dt'\hat{\mathcal{H}}(t')\}=\exp\{-i\bar{\mathcal{H}}t\} \tag{3.85}$$

Applying the *Magnus expansion* [39] to $\hat{U}(t_c,t_0)$:

$$\hat{U}(t_c,t_0)=\exp\{-i(\bar{\mathcal{H}}^{(1)}+\bar{\mathcal{H}}^{(2)}+\bar{\mathcal{H}}^{(3)}+\cdots)t\} \tag{3.86}$$

taking into account the *Baker-Campbell-Hausdorff formula* [25], the first two terms are equal to:

$$\bar{\mathcal{H}}^{(1)}=\frac{1}{t}\int_{t_0}^{t}\hat{\mathcal{H}}(t)dt \tag{3.87}$$

$$\bar{\mathcal{H}}^{(2)}=-\frac{i}{2t}\int_{t_0}^{t}dt'\int_{t_0}^{t'}[\hat{\mathcal{H}}(t'),\hat{\mathcal{H}}(t)]dt \tag{3.88}$$

Each of these terms is an Hermitian operator and the truncation of the expansion leaves a Hermitian operator. The Magnus expansion converges rapidly if the condition give below is satisfied:

$$\left\|\hat{\mathcal{H}}(t)\right\|t\ll 1 \tag{3.89}$$

Additionally, it is possible to increased the speed of convergence of the Magnus expansion by expressing the Hamiltonian $\hat{\mathcal{H}}(t)$ in an appropriate frame called the *interaction frame* or *toggling frame*.

The Magnus expansion may be truncated at different points, depending on the situation. In many cases, just using $\bar{\mathcal{H}}^{(1)}$ is not enough and one must include higher-order terms as well.

Suppose that the the total Hamiltonian can be defined as the sum of two Hamiltonians:

one large and easy to handle ($\hat{\mathcal{H}}_A$), another small but difficult to handle ($\hat{\mathcal{H}}_B$):

$$\hat{\mathcal{H}}_{total}=\hat{\mathcal{H}}_A+\hat{\mathcal{H}}_B \tag{3.90}$$

Generally, these two Hamiltonians do not commute and are time-dependent. In this condition, a propagator U for the evolution under $\hat{\mathcal{H}}_{total}$ can be defined:

$$U=U_A\tilde{U}_B \tag{3.91}$$

where U_A is a propagator that fulfills the next condition:

$$\frac{d}{dt}U_A=-i\mathcal{H}_A U_A \tag{3.92}$$

and $\tilde{U}_B$ is the propagator under interaction frame Hamiltonian and solves the equation:

$$\frac{d}{dt}\tilde{U}_B=-i\tilde{\mathcal{H}}_B\tilde{U}_B \tag{3.93}$$

The *interaction frame Hamiltonian* $\tilde{\mathcal{H}}_B$ can be obtained by the transformation:

$$\tilde{\mathcal{H}}_B=U_A^{\dagger}\mathcal{H}_B U_A \tag{3.94}$$

It is convenient to properly choose $\mathcal{H}_A$ and $\mathcal{H}_B$ to simplify the calculations. In NMR it is common to assign $\mathcal{H}_A=\mathcal{H}_{RF}$ and $\mathcal{H}_B=\mathcal{H}_{spin}$.

4. Solid-State NMR Techniques

Solid-state NMR has grown into an indispensable technique for structural determination, chemical analysis and study of dynamics in many systems, from biological systems such as proteins [40], [41], [33] to inorganic systems such as zeolites [42], [43]. However, in the beginning, the application of solid-state NMR was mainly restricted to physics because of its low-sensitivity and lack of resolution in comparison with NMR in liquids or oriented phases. In this section, the experimental solid-state NMR techniques used in this thesis will be described.

The resonance lines of small and isolated spin systems in *single crystals (ordered samples)* are well resolved, allowing the determination of the anisotropic spin interactions directly. However, it is usually quite difficult to obtain good single crystals for all samples. Therefore, solid-state NMR is commonly performed on *powders*, which are composed of many crystallites, each one with a *random orientation* with respect to the external field. Thus, the NMR spectrum of a powdered sample shows broad lines mainly due to the anisotropic part of the spin interactions. The introduction of the *MAS technique* [44], [45], [46] allows one to average out the anisotropic interactions to first order. Nowadays, the majority of solid-state NMR experiments are performed under MAS.

In general, NMR is a low-sensitivity technique because of the small population difference between energy levels and the low abundance and low gyromagnetic ratio of many nuclei. These features produce small signals difficult to distinguish from the spectral noise. To compensate for these effects, NMR uses a larger amount of sample than in other types of spectroscopy. The commonest method to enhance the signal in solid-state NMR is *cross-polarisation (CP)* [47]. This method is based on transferred magnetization from *"abundant" nuclei*, such protons, to *"rare" low-γ nuclei.*

An important issue in the solid-state NMR of biological samples is the effect of strong heteronuclear interactions between ^{1}H and other nuclei, like ^{13}C. The high abundance and high gyromagnetic ratio of ^{1}H make the dipolar interactions between the protons and other nuclei quite strong and difficult to remove under MAS conditions. Usually, these heteronuclear dipolar interactions broaden the NMR signal of other nuclei, such as ^{13}C. Therefore, it is important to *decouple* these heteronuclear interactions to get a high-resolution spectrum of "rare" nuclei in the present of "abundant" nuclei. Strong irradiation on the "abundant" nuc-

lei without phase or amplitude modulation, knows as *continuous wave decoupling (CW)* [48], [49], has been one of the most common solutions for this problem but more efficient ways of decoupling have been proposed such as the TPPM [50] and SPINAL [51] decoupling schemes.

The combination of CP and MAS techniques, plus heteronuclear decoupling, has become the standard way of obtaining high resolution solid-state NMR spectra of ^{13}C in biological samples [52]. These techniques remove to first order the anisotropic interactions of the spin system which contain important information about the structure of the system. Therefore, it is important to reintroduce these interactions by using *recoupling pulse sequences* to get this important structural information [40].

4.1. Magic-Angle Spinning

The static NMR spectrum of a solid sample is dominated by broad lineshapes, with low resolution, due to anisotropic interactions as DD-couplings or CSA (see Fig. 4.2). The spectral resolution can be increased if the anisotropic part of the spin Hamiltonian is removed. This can be achieved by using *magic-angle spinning (MAS).*The vast majority of solid-state NMR experiments with high resolution are performed under MAS. This technique, introduced by Lowe [44] and Andrew et al [45] in the 1950's, consists of rotating the sample rap-

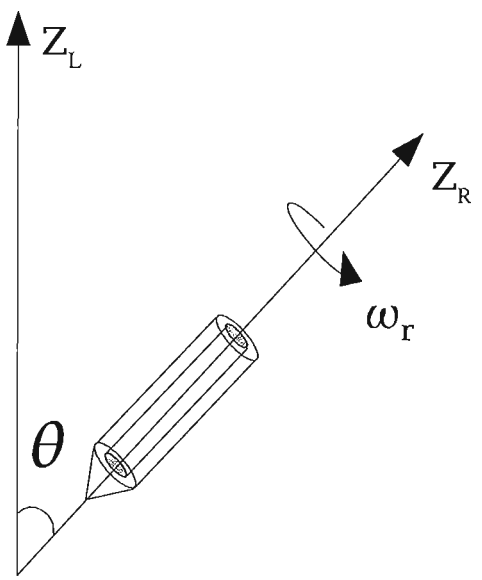

Fig. 4.1. Fig. 5.5. Macroscopic sample rotation at the magic-angle (θ) at a spinning frequency of ω_r. The axis Z_L is the z-axis of the laboratory frame, which coincides with the direction of the main magnetic field and Z_R is the z-axis of the rotor frame.

idly around an axis with an angle of β_{RL} equal to 54.7^0 with respect to the main field, called the magic-angle (Fig. 4.1). Generally, the sample is spun at a frequency between a few hundred Hz and 50 kHz.

MAS averages out to zero all the spin interactions whose anisotropic part can be described by second-rank irreducible spherical tensors (for example CSA, DD-coupling), if the spinning frequency is high enough with respect to the interaction size. This is quite an astonishing result but if we consider the form of the Hamiltonian for one of these interactions under the secular approximation and considering the restriction to time averaging it follows that:

$$D^2_{m0}(\Omega^{\Lambda}_{PL}) = D^2_{00}(\Omega^{\Lambda}_{PL}) = \frac{1}{2}(3\cos^2\beta_{PL} - 1) \tag{4.1}$$

If β_{PL} is equal to the magic-angle, this term is 0 and the secular Hamiltonian is made to vanish.

In powder samples the angle β_{PL} takes all possible values, since each crystallite has a different orientation with respect to the main field. In this case, when the sample is spun rapidly around a spinning axis with an angle β_{RL} with respect to the main magnetic field $\mathbf{B}^0$, it can be shown that the average value of $3\cos^2\beta_{PL} - 1$ for the interaction is determined by the angle β_{RL} [53], [54]. If this angle is equal to 54.7^0 the average value of $3\cos^2\beta_{PL} - 1$ is equal

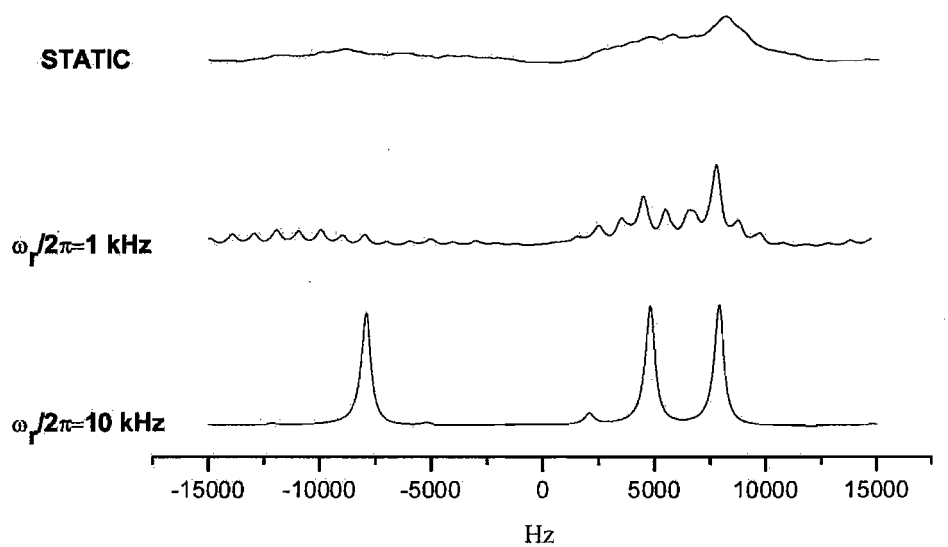

Fig. 4.2. ^{13}C simulated spectra of $^{13}C_3$-alanine at a magnetic field of 400 MHz. The figure shows the static spectrum, the spectrum at MAS frequency of 1 kHz and the spectrum at MAS frequency of 10 kHz.

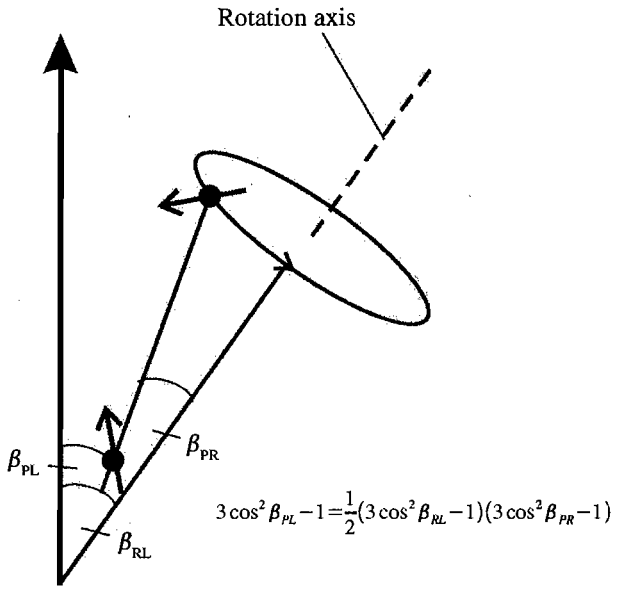

Fig. 4.3. Macroscopic sample rotation at the magic angle to the main magnetic field $\mathbf{B}^0$. The following geometrical relationships are shown: β_{PL} is the angle between the z-axis of the laboratory frame (L) and the z-axis of the principal axis fame of the interaction (PAS), β_{PR} is the angle between z-axis of the PAS frame of the interaction and the z-axis of the rotor frame and β_{RL} is the frame between the z-axis of the L frame and z-axis of the R frame. The angles β_{PL} and β_{PR} are fixed for each crystallite orientation but β_{RL} is controlled externally. If the angle β_{RL} is 54.7^0 the spatial part of the spin interaction is averaged out to zero.

to 0 and the anisotropic part of the interaction is made to vanish.

4.2. Cross-Polarisation

MAS is an essential tool in solid-state NMR in order to increase spectral resolution. However solid-state NMR of "rare" nuclei, such ^{13}C, has a low sensitivity. There are three reasons why the sensitivity of "rare" nuclei can be low:

1. Low gyromagnetic ratio.
2. Low natural abundance.
3. Usually the relaxation time T_1 is quite long.

A practical approach, in order to detect these rare spins, is to transfer magnetization from the abundant to the rare spins through the DD couplings [56], [19], [30]. The most

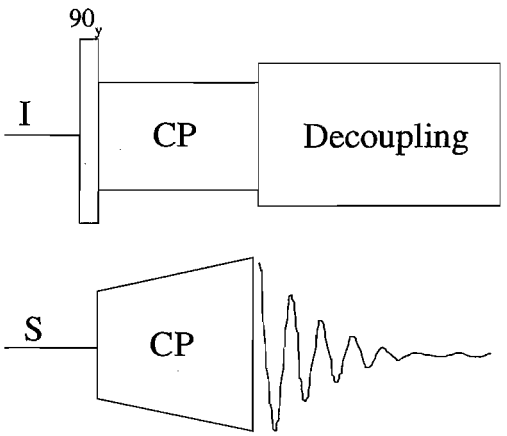

Fig. 4.4. The ramped cross-polarisation sequence [55].

popular scheme in solid-state NMR is a method called *cross-polarisation (CP)* [47]. The sequence is shown in Fig. 4.4 in which ^{1}H and ^{13}C are the "abundant" and the "rare" species. A 90 degree pulse on the proton channel creates ^{1}H magnetization. After this pulse, spin lock fields are applied on both channels. In order to transfer magnetisation, these two fields have to fulfil the Hartmann-Hahn condition [56]:

$$\text{Under static conditions: } \omega_{rf}^{I}=\omega_{rf}^{S} \Rightarrow \gamma_I B_{rf}^{I}=\gamma_S B_{rf}^{S} \tag{4.2}$$

$$\text{Under MAS conditions: } \omega_{rf}^{I}=\omega_{rf}^{S}+n\omega_r \Rightarrow \gamma_I B_{rf}^{I}=\gamma_S B_{rf}^{S}+n\omega_r \tag{4.3}$$

where B_{rf}^{I} and B_{rf}^{S} are the field strengths applied to each nucleus and n is an integer. The mechanism of CP through the DD couplings is explained in terms of thermodynamics and quantum mechanics in [19], [30], [24].

By using CP, the theoretical signal enhancement is expected to be proportional to γ_I/γ_S, depending on the proportions of I and S spins. An improvement in reliability and reproducibility of the CP experiment can be achieved by using the *ramped-CP experiment* [55]. In the ramped-CP experiment, the contact pulse on one of the spins (it can be either) is steadily increased in amplitude over the contact period. In this case, for systems ^{13}C-^{1}H, the enhancement of ^{13}C signal is usually a factor of 3.

4.3. Heteronuclear Decoupling

For the application of solid-state NMR to biological systems high resolution is essential.

However, in biological samples, strong ^{13}C-^{1}H heteronuclear interactions are of the order of 20-30 kHz, which are difficult to remove by MAS. Additionally, in the present of strong homonuclear dipolar couplings, the *non commutation* with the heteronuclear dipolar couplings leads to a high-order interactions, resulting in an incomplete averaging of the heteronuclear interactions [57]. Therefore, rf irradiation techniques are needed to decouple these strong heteronuclear interactions in biological samples (Fig. 4.6). In this section, heteronuclear decoupling methods used for the work in this thesis will be discussed.

A common method used to eliminate heteronuclear couplings in solid-state NMR spectroscopy is a technique called *continuous wave decoupling (CW).* CW decoupling works by rotating the spin state of ^{1}H spins, thus, the dipolar interaction is averaged out every 2π rotation while the spin state of the ^{13}C spins is not modified.

Under MAS, sample rotation and CW rf irradiation can interfere with each other, if their

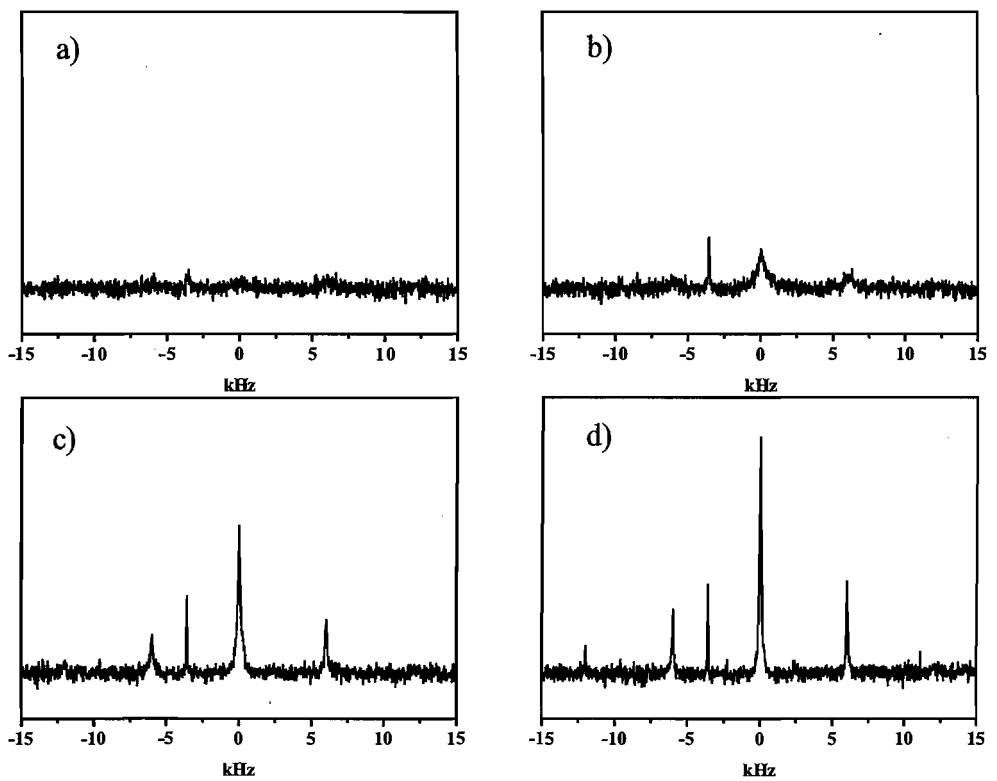

Fig. 4.5. CP-MAS experiments at different CW decoupling rf fields of: a) $\omega_{nut}/2\pi$ = 0 kHz, b) $\omega_{nut}/2\pi$ = 41.7 kHz, c) $\omega_{nut}/2\pi$ = 83.3 kHz, and d) $\omega_{nut}/2\pi$ = 113 kHz. The experiments were performed on a 400 MHz spectrometer using a 3.2 mm rotor at MAS of 6 kHz. The sample was 2,3-[$^{13}C_2$]-diammonium fumarate 10% diluted in natural abundance diammonium fumarate DAF (for the molecular structure see chapter 6). Each experiment was recorded in 4 scans and the delay between transients was 5 s.

timescales are comparable, leading to inefficient heteronuclear decoupling. Therefore, there are two different regimes in which CW decoupling is efficient: *high power CW decoupling* and *low power CW decoupling* [57]. In the first one, high CW irradiation (50-250 kHz) is applied while the spinning frequency is maintained in a low-moderate regime (up to 25 kHz). In this regime the linewidth decreases when the rf irradiation is increased (Fig. 4.6). The second approach is applied under high spinning frequency (>30 kHz) and the CW rf field is maintained under 50 kHz [57]. Similar regimes have been found in the work presented in chapter 6 for the effect of CW decoupling irradiation during application of DQ homonuclear dipolar recoupling symmetry-based sequences.

One of the limitations of CW decoupling is that *off-resonance effects* produce an incomplete heteronuclear decoupling. Residual line splittings increase with increasing MAS frequency and decoupling sidebands can be observed at the rf irradiation frequency. However, the introduction of *phase modulated decoupling sequences* [50], [51] has given a significant improvement in both linewidth and line intensity.

In the work of this thesis a phase-modulated sequence called *small incremental alternation (SPINAL)* [51] has been used for heteronuclear decoupling during acquisition of the FID. The SPINAL decoupling sequence is built of two elements, Q and $\bar{Q}$:

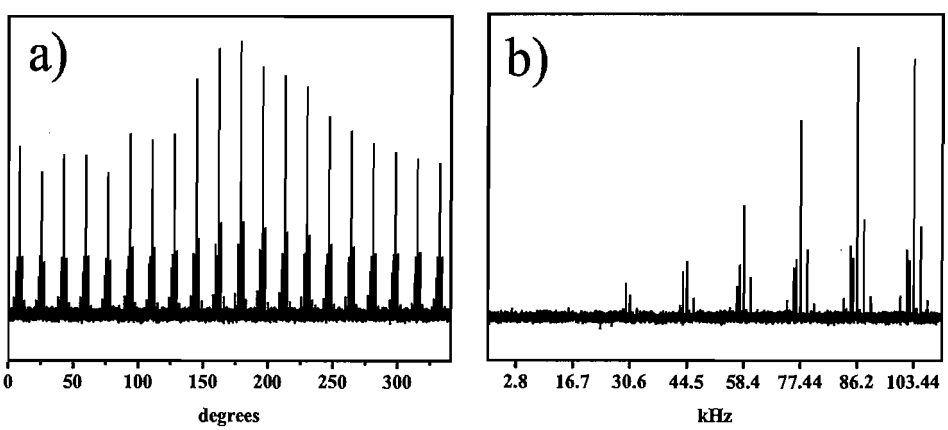

Fig. 4.6. a) Optimization of the flip angle in a SPINAL-64 sequence for a rf field of 82.6 kHz nutation frequency. It can be seen that there is a maximum of performance at a value close to 165°. b) Optimization of the rf field in a SPINAL-64 decoupling sequence. Both experiments were performed on a 400 MHz spectrometer using a 3.2 mm rotor at MAS of 6 kHz. The sample was 2,3-[$^{13}C_2$]-diammonium fumarate 10% diluted in natural abundance diammonium fumarate DAF (for the molecular structure see chapter 6). Each experiment was recorded in 4 scans and the delay between transients was 5 s.

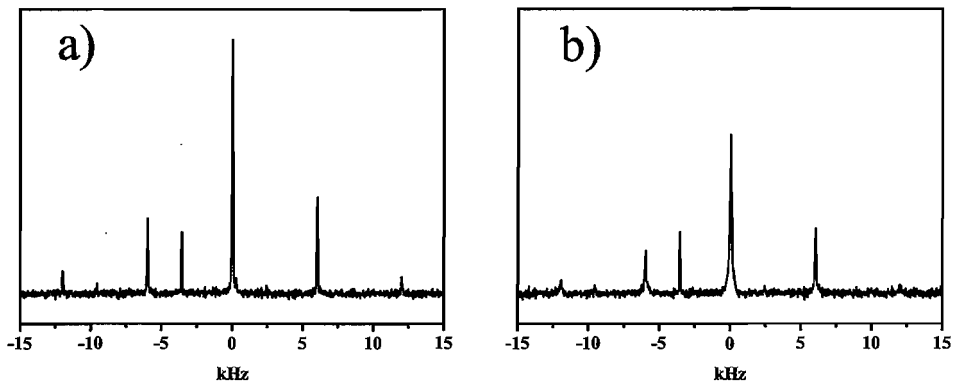

Fig. 4.7. a) CP-MAS experiment with SPINAL decoupling optimized for a ^{1}H nutation frequency of 86.2 kHz. b) CP-MAS with CW decoupling at a ^{1}H nutation frequency of 86.2 kHz. Both experiment were performed on a 400 MHz spectrometer using a 3.2 mm rotor at MAS of 6 kHz. The sample was 2,3-[$^{13}C_2$]-diammonium fumarate 10% diluted in natural abundance diammonium fumarate DAF (for the molecular structure see chapter 6). Each experiment was recorded in 4 scans and the delay between transients was 5 s.

$$Q = 165_{10^\circ}\ 165_{-10^\circ}\ 165_{15^\circ}\ 165_{-15^\circ}\ 165_{20^\circ}\ 165_{-20^\circ}\ 165_{15^\circ}\ 165_{-15^\circ} \tag{4.4}$$

$$\bar{Q} = 165_{-10^\circ}\ 165_{10^\circ}\ 165_{-15^\circ}\ 165_{15^\circ}\ 165_{-20^\circ}\ 165_{20^\circ}\ 165_{-15^\circ}\ 165_{15^\circ} \tag{4.5}$$

These elements can be combined into supercycles to build different SPINAL cycles:

$$\begin{aligned}
\text{SPINAL}-16 &= Q\bar{Q} \\
\text{SPINAL}-32 &= Q\bar{Q}\bar{Q}Q \\
\text{SPINAL}-64 &= Q\bar{Q}\bar{Q}Q\ \bar{Q}QQ\bar{Q} \\
\text{SPINAL}-128 &= Q\bar{Q}\bar{Q}Q\ \bar{Q}QQ\bar{Q}\ QQ\bar{Q}Q\ \bar{Q}\bar{Q}Q\bar{Q}
\end{aligned}$$

SPINAL-64 has been used in the present work for decoupling during acquisition.

From Fig. 4.7, it can be seen that the SPINAL-64 decoupling sequence provides a large improvement in performance compared with CW decoupling.

4.4. Dipolar Recoupling

It is useful to reintroduce the anisotropic interactions averaged out by MAS in order to obtain information about the environment of the nuclei. This is called *recoupling*. One of the interactions that is averaged out by MAS is the direct dipole-dipole coupling which is essential in structural determination because of the dependence of this interaction on the distance between nuclei. The dipolar couplings can be reintroduced by *dipolar recoupling*.

The principle of dipolar recoupling is to apply *rotor-synchronized pulse sequences*,

which are known as a *recoupling sequences*, in order to reintroduce the dipolar couplings while maintaining the high resolution achieved by MAS. In the case of dipolar recoupling, *homonuclear and heteronuclear dipolar recoupling* can be distinguished.

Dipolar recoupling sequences have the following applications:

- **Determination of Internuclear Distances:**

  In the simplest case the evolution of the NMR signal intensities is measured as a function of the time interval in which the dipolar recoupling sequence is applied. The evolution of the signal depends on the distance between pairs of nuclei.

- **Magnetization Exchange:**

  Magnetization is transferred betweens spins through dipolar couplings. These techniques allows to identify spins that are bonded or close to each other. Another important application is to enhance the sensitivity of low-γ nuclei by transferring magnetization from high-γ nuclei through heteronuclear dipolar couplings.

- **Determination of Bond-Angles and Torsional Angles:**

  The relative orientation of dipolar interactions can be determined by experiments involving dipolar recoupling sequences.

- **Excitation of Multiple-Quantum Coherences (MQC):**

  MQC can be excited by using dipolar recoupling sequences. These experiments are useful in the structural determination of spin clusters.

4.4.1. Homonuclear Dipolar Recoupling

Homonuclear dipolar recoupling reintroduces the direct coupling between identical

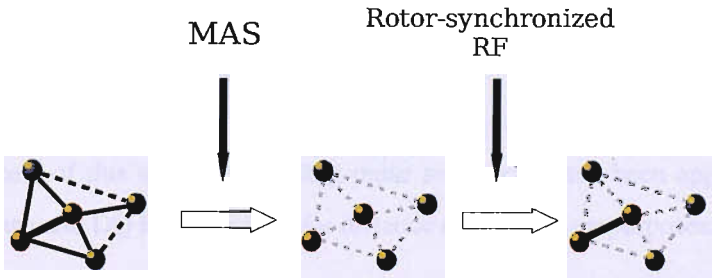

Fig. 4.8. Basic idea of recoupling in magic-angle spinning solid-state NMR. The anisotropic interactions are removed by fast MAS. Anisotropic interactions are reintroduced by a rotor-synchronized rf field.

spins. Consider a two-spin system $\hat{I}_i$ and $\hat{I}_j$. Different average Hamiltonians may be generated using a homonuclear dipolar recoupling sequence:

- **Homonuclear zero-quantum recoupling.**

  The first-order average Hamiltonian is given by:

$$\bar{\mathcal{H}}^{(1)}=\omega_{ij}\frac{1}{\sqrt{6}}(2\hat{I}_{iz}\hat{I}_{jz}-\frac{1}{2}(\hat{I}_i^-\hat{I}_j^+ + \hat{I}_i^+\hat{I}_j^-)) \tag{4.6}$$

  where the terms $\hat{I}_i^-\hat{I}_j^+$ and $\hat{I}_i^+\hat{I}_j^-$ are called zero-quantum terms. In terms of irreducible spherical tensors, the Hamiltonian contains two-spin terms with a total spin component of μ= 0. The rf pulse sequence generating this Hamiltonian is called a homonuclear zero-quantum recoupling sequence. This kind of Hamiltonian is perfect for exchange of magnetization. Additionally, it could be used for distance-measurement experiments.

- **Homonuclear single-quantum recoupling.**

  The first-order average Hamiltonian is given by:

$$\bar{\mathcal{H}}^{(1)}=\omega_{ij}\frac{1}{2}((\hat{I}_i^-\hat{I}_{jz}+\hat{I}_{iz}\hat{I}_j^-))+\omega_{ij}^*\frac{1}{2}((\hat{I}_i^+\hat{I}_{jz}+\hat{I}_{iz}\hat{I}_j^+)) \tag{4.7}$$

  In terms of irreducible spherical tensors, the Hamiltonian contains two-spin terms with a total spin component of μ=±1. The rf pulse sequence generating this Hamiltonian is called a homonuclear single-quantum recoupling sequence.

- **Homonuclear double-quantum recoupling.**

  The first-order average Hamiltonian is given:

$$\bar{\mathcal{H}}^{(1)}=\omega_{ij}\frac{1}{2}(\hat{I}_i^-\hat{I}_j^-)+\omega_{ij}^*\frac{1}{2}(\hat{I}_i^+\hat{I}_j^+) \tag{4.8}$$

  In terms of irreducible spherical tensors, the Hamiltonian contains two-spin terms with a total spin component of μ=±2. This kind of Hamiltonian has been extensively used to extract internuclear distance information. The rf pulse sequence generating this Hamiltonian is called a homonuclear double-quantum recoupling sequence.

In the context of this thesis, recoupling pulse sequences have been applied to produce ZQ Hamiltonians and DQ Hamiltonians for distance determination purposes.

4.4.2. Heteronuclear Dipolar Recoupling

Heteronuclear dipolar recoupling reintroduces the direct coupling between different

spins by a heteronuclear dipolar recoupling sequence. Consider a two-spin system I_i and S_j. Four different average Hamiltonians may be generated using a heteronuclear dipolar recoupling sequence:

- **Longitudinal two-spin recoupling.**

  The first-order average Hamiltonian is given by:

$$\bar{\mathcal{H}}^{(1)}=\omega_{ij}\hat{I}_{iz}\hat{S}_{jz} \tag{4.9}$$

  This Hamiltonian contains only terms with spin components $(\mu_I,\mu_S) = 0$. This average Hamiltonian has the same form as the Hamiltonian for the direct heteronuclear dipolar Hamiltonian of Eq.(4.9). Under this kind of average Hamiltonian the evolution of a heteronuclear multispin system is described by a superposition of the evolution of isolated spin pairs. This property has been exploited in distance measurement in heteronuclear multispin systems.

- **Heteronuclear zero-quantum recoupling.**

  The first-order average Hamiltonian is given by:

$$\bar{\mathcal{H}}^{(1)}=\omega_{ij}\hat{I}_i^-\hat{S}_j^+ + \omega_{ij}^*\hat{I}_i^+\hat{S}_j^- \tag{4.10}$$

  In terms of irreducible spherical tensors, the Hamiltonian contains two-spin terms with a total spin component of $(\mu_I,\mu_S) = (\pm1,\mp1)$. The r.f. pulse sequence generating this Hamiltonian is called a heteronuclear zero-quantum recoupling sequence.

- **Heteronuclear single-quantum recoupling.**

  The first-order average Hamiltonian is given:

$$\bar{\mathcal{H}}^{(1)}=\omega_{ij}\hat{I}_{iz}\hat{S}_j^- + \omega_{ij}^*\hat{I}_{iz}\hat{S}_j^+ \tag{4.11}$$

  In terms of irreducible spherical tensors, the Hamiltonian contains two-spin terms with a total spin component of $(\mu_I,\mu_S) = (\pm1,0)$ or $(\mu_I,\mu_S) = (0,\pm1)$.The rf pulse sequence generating this Hamiltonian is called a heteronuclear single-quantum recoupling sequence.

- **Heteronuclear double-quantum recoupling.**

  The first-order average Hamiltonian is given by:

$$\bar{\mathcal{H}}^{(1)}=\omega_{ij}\hat{I}_i^-\hat{S}_j^- + \omega_{ij}^*\hat{I}_i^+\hat{S}_j^+ \tag{4.12}$$

  In terms of irreducible spherical tensors, the Hamiltonian contains two-spin terms with a total spin component of $(\mu_I,\mu_S) = (\pm1,\pm1)$.The r.f. pulse sequence generating this Hamiltonian is called a heteronuclear double-quantum recoupling sequence.

In this thesis, different recoupling sequences [58], [59] have been used to minimize the interference of average heteronuclear Hamiltonians in homonuclear dipolar recoupling sequences.

4.4.3. Dipolar Recoupling Pulse Sequences

Solid-state NMR is based on two spin manipulations: (i) spatial manipulation by rotation of the sample at a frequency around an a fixed axis; and (ii) spin rotations by using applied r.f. pulses. For a long time both manipulations were used separately in order to decouple or recouple the desired spin interactions. However, at the beginning of the 1980s, the sample rotation and the r.f. pulse sequences were combined in a powerful way and the recoupling was born as it is known today.

The first successful homonuclear dipolar recoupling sequence was DRAMA [60], [61]. This sequence is composed of strong 90^0 pulses synchronized with the sample rotation. The RFDR scheme by Griffin and co-workers [62], [63] and [64] was a popular alternative. This pulse sequence is made of rotor-synchronized 180^0 pulses. While DRAMA produces a mixture of zero-quantum and double-quantum Hamiltonians, the RFDR sequence generates a pure zero-quantum Hamiltonian.

The next development in homonuclear dipolar recoupling was the introduction of HORROR [65]. This sequence produce an DQ Hamiltonian with high efficiency by controlling the angular orientation of the recoupled Hamiltonian but HORROR is only feasible for coupled spins with a small difference in chemical shifts. This problem was solved by the introduction of C7 and its variants [66], [67] and [68]. These sequences maintain a high DQ excitation while the control of the orientation-dependence is maintained.

The theory behind C7 is based on the symmetry properties of the spin interactions. An extension of this theory has led to the *rotor-synchronized symmetry-based pulse sequences* [58]. The symmetry classes for symmetry-based sequences have been divided into *C-symmetries* [59], [66], [69] and *R-symmetries* [59], [70]. These two symmetries lead to the two classes of symmetry-based sequences: CN_n^{ν} and RN_n^{ν}.

In the context of heteronuclear dipolar recoupling, the most successful method is REDOR [13], [71], in which 180 degree pulses are applied synchronized with the rotor frequency.

The symmetry-based sequences have been used as single-channel heteronuclear recoupling sequences [59], [70], [72], [73], [74]. Additionally, the concept of symmetry-based se-

quences can be generalized to the case of dual channel r.f. irradiation [59], [75]. These sequences can be used to enhance the signal of low-γ nuclei [76], [74] and for dipolar recoupling [73], [77] or heteronuclear decoupling [75].

Chapter 7 studies the effect of irradiation on the ^{1}H channel during DQ homonuclear dipolar recoupling. Symmetry arguments and theory have been used to find conditions under which we obtain high DQ efficiencies for homonuclear dipolar recoupling while reducing the interference from heteronuclear interactions [75].

In chapter 8, a ZQ dipolar recoupling CN_n^ν sequence is used for dipolar recoupling in multiple spin systems. The sequence has been designed to recouple dipolar couplings terms plus chemical shift terms, which are used to truncate the dipolar Hamiltonian, allowing different dipolar couplings in a multiple spin system to be treated independently [78].

5. Symmetry-Based Recoupling

Rotor-synchronized recoupling pulse sequences use symmetry properties of the spin interactions to generate an average Hamiltonian containing terms with the desired combinations of quantum numbers l, m, λ and μ (Table 5.1).

In order to obtain this effect, the spin and spatial trajectories have to be synchronized. This can be accomplished by setting up *periodic symmetry relationships* between the mechanical and the r.f. rotations. Two classes of symmetry of the rotor-synchronized pulse sequences have been identified: CN_n^ν *and* RN_n^ν *symmetry classes.*

The CN_n^ν sequences impose the Euler angle symmetry:

$$\begin{aligned} \beta_q\left(t+\frac{n\tau_r}{N}\right) &= \beta_0(t) \\ \gamma_q\left(t+\frac{n\tau_r}{N}\right) &= \gamma_0(t)-\frac{2\pi\nu}{N}q \end{aligned} \tag{5.1}$$

where N, ν and n are integers called *symmetry numbers* and τ_r is the *rotor period*. The integer q takes values q = 0, 1, ..., N-1.

Table 5.1. Rotational signatures of spin interactions in systems of spin-1/2.

Interaction	Space rank l	Space component m	Spin rank λ	Spin component μ
Isotropic CS	0	0	1	-1, 0, 1
CSA	2	-2, -1, 1, 2	1	-1, 0, 1
Homonuclear isotropic J-coupling	0	0	0	0
Homonuclear dipolar coupling	2	-2, -1, 1, 2	2	-2, -1, 0, 1, 2
Heteronuclear isotropic J-coupling	0	0	1	-1, 0, 1
Heteronuclear dipolar coupling	2	-2, -1, 1, 2	1	-1, 0, 1

In the case of RN_n^ν sequences, the Euler angle symmetry is given by:

$$\begin{aligned} \beta_q\left(t+\frac{n\tau_r}{N}\right) &= \beta_0(t)\pm q\pi \\ \gamma_q\left(t+\frac{n\tau_r}{N}\right) &= \gamma_0(t)-\frac{2\pi\nu}{N}q \end{aligned} \tag{5.2}$$

These symmetry classes manipulate the recoupling and decoupling of different spin terms by defining a set of selection rules of the Average Hamiltonian. Since the third Euler angle α_q is left completely free, there are many ways of implementing these two symmetry relationships. Two convenient possibilities will be described below.

The CN_n^ν and RN_n^ν rotor-synchronized sequences are applied at the Larmor frequency of

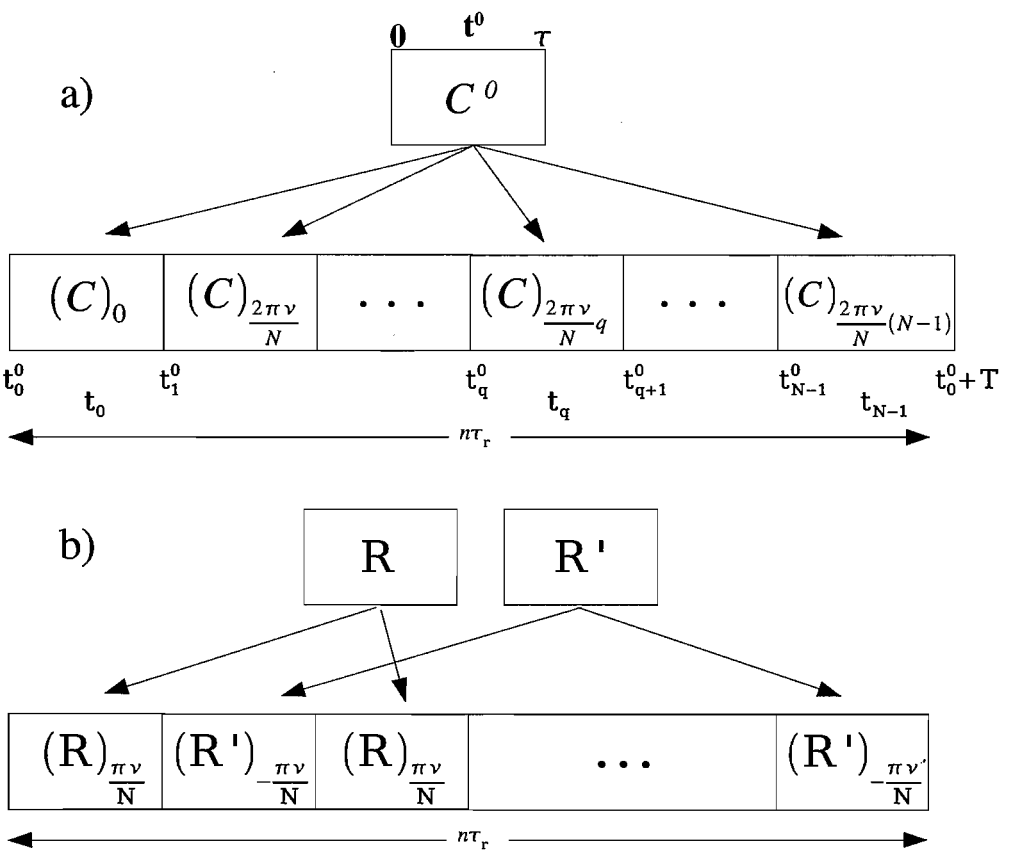

Fig. 5.1. a) One way of implementing a *C*-sequence. The sequence is built up from an element C^0, which is a rf cycle. The *C*-sequence is composed of *N* phase-shifted cycles. b) One way of implementing a *R*-sequence. The element *R* implements a π rotation about x-axis. The element *R'* is equivalent to R but with a change in the sign of all phases. The *R*-sequence is composed of N/2 *RR'* pairs. Figures taken from [59].

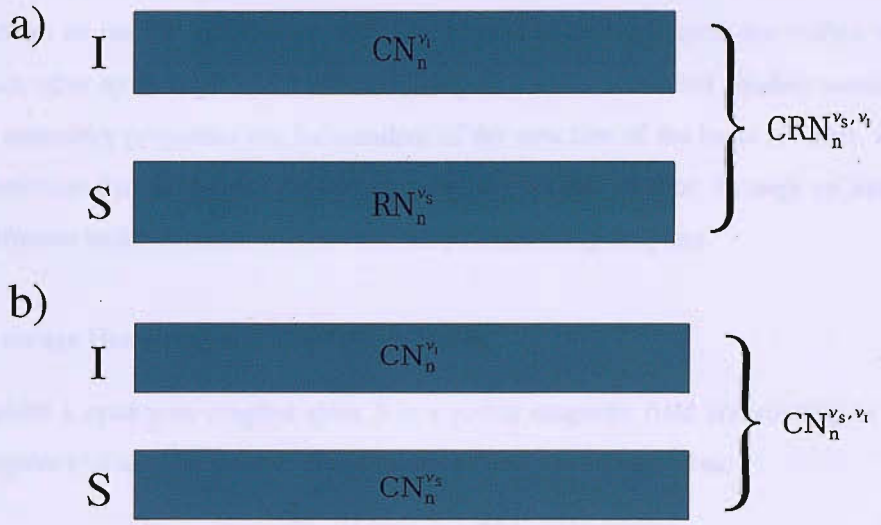

Fig. 5.2. a) A $CRN_n^{\nu_I,\nu_S}$ sequence scheme. b) A $CN_n^{\nu_I,\nu_S}$ sequence scheme. Figures taken from [59].

one spin species, for instance ^{13}C. However, rotor-synchronized pulse sequences can be applied simultaneously at the Larmor frequencies of two different spin species. In the case of applying simultaneously the CN_n^{ν} and RN_n^{ν} sequences at the Larmor frequencies of I and S spins, there are four possibilities of *dual-synchronized pulse sequences*:

- $CN_n^{\nu_I}$ is applied on I-spins and $CN_n^{\nu_S}$ on S-spins. This type is denoted $CN_n^{\nu_I,\nu_S}$.
- $CN_n^{\nu_I}$ is applied on I-spins and $RN_n^{\nu_S}$ on S-spins. This type is denoted $CRN_n^{\nu_I,\nu_S}$.
- $RN_n^{\nu_I}$ is applied on I-spins and $CN_n^{\nu_S}$ on S-spins. This type is denoted $RCN_n^{\nu_I,\nu_S}$.
- $RN_n^{\nu_I}$ is applied on I-spins and $RN_n^{\nu_S}$ on S-spins. This type is denoted $RN_n^{\nu_I,\nu_S}$.

In this chapter, the types $CRN_n^{\nu_I,\nu_S}$ and $CN_n^{\nu_I,\nu_S}$ will be described in sections 6.3 and 6.4. In chapter 7, these types of dual channel sequence have been used to get high DQ homonuclear excitation in ^{13}C while the effects of heteronuclear interactions with ^{1}H are minimized.

5.1. CN_n^{ν} Sequences

5.1.1. Definition

One possible implementation of the time-symmetry relationships defined in Eq. (5.1) is

given in Fig. 5.1. The idea is the repetition of a *basic element N* times over *n* rotor periods. This basic element *C* has to be a *cycle* in the sense of [79], inducing a rotation of the nuclear spin through an integer multiple of 360^0. The phases of each r.f. cycle are shifted with respect each other by an angle of $2\pi\nu/N$. The integers *n* and ν are called *winding numbers.*

The symmetry properties are independent of the structure of the basic element, with the only restriction that each cycle has to accomplishe a final rotation through an integer of 360^0. Different basic elements will be described in following chapters.

5.1.2. Average Hamiltonian and Selection Rules.

Consider a system of coupled spins *S* in a strong magnetic field and rotating at a spinning frequency of ω_r. The internal Hamiltonian at time t is expressed as:

$$\hat{\mathcal{H}}_{\text{int}}(t)=\sum_{\Lambda,l,m,\lambda}\hat{\mathcal{H}}^{\Lambda}_{lm\lambda 0}(t) \tag{5.3}$$

Because of the rotation of the system, the Hamiltonian is periodically modulated, so we can write:

$$\hat{\mathcal{H}}^{\Lambda}_{lm\lambda 0}(t)=\omega^{\Lambda}_{lm}\exp\{im\omega_r t\}T^{\Lambda}_{\lambda 0} \tag{5.4}$$

with complex amplitudes equal to:

$$\omega^{\Lambda}_{lm}=[A^{\Lambda}_{lm}]^R d^{l}_{m0}(\beta_{RL})\exp\{-im\alpha^{0}_{RL}\} \tag{5.5}$$

where α^{0}_{RL} denotes the initial position of the rotor and β_{RL} is the angle between the axis of rotation and the main magnetic field.

Consider a rotor synchronized pulse sequence and the definition of t_q as in Fig. 5.1. Eq. (5.4) may be expressed:

$$\hat{\mathcal{H}}^{\Lambda}_{lm\lambda 0}(t_q)=\hat{\mathcal{H}}^{\Lambda}_{lm\lambda 0}(t_0)\exp\{i\frac{2\pi m}{N}q\} \tag{5.6}$$

Before applying AHT the Hamiltonian has to be transformed into the interaction frame of the rf field. The interaction frame Hamiltonian at time point t_q can be written as:

$$\tilde{\mathcal{H}}_{\text{int}}(t_q)=\sum_{\Lambda,l,m,\lambda,\mu}\tilde{\mathcal{H}}^{\Lambda}_{lm\lambda\mu}(t_q)=d^{\lambda}_{\mu 0}(-\beta_q)\omega^{\Lambda}_{lm}\exp\{i\mu\gamma_q+im\omega_r t_q\}T^{\Lambda}_{\lambda\mu} \tag{5.7}$$

If the Euler angle symmetry for CN^{ν}_{n} sequences applies, the interaction frame Hamiltonian is:

$$\tilde{\mathcal{H}}^{\Lambda}_{lm\lambda\mu}(t_q)=\tilde{\mathcal{H}}^{\Lambda}_{lm\lambda\mu}(t_0)\exp\left\{i\frac{2\pi m}{N}q(mn-\mu\nu)\right\} \tag{5.8}$$

The interaction frame Hamiltonian for the CN^{ν}_{n} sequence can be analysed by using the

Magnus expansion [39]:

$$\bar{\mathcal{H}}=\bar{\mathcal{H}}^{(1)}+\bar{\mathcal{H}}^{(2)}+\cdots=\sum_{\Lambda,l,m,\lambda,\mu}\bar{\mathcal{H}}^{\Lambda}_{lm\lambda\mu}+\sum_{\Lambda_2 2,\Lambda_1 1}\bar{\mathcal{H}}^{\Lambda_2\times\Lambda_1}_{2;1}+\cdots \tag{5.9}$$

where the first-order term is given by :

$$\bar{\mathcal{H}}^{\Lambda}_{lm\lambda\mu}=T^{-1}\int_{t_0^0}^{t_0^0+T}\tilde{\mathcal{H}}^{\Lambda}_{lm\lambda\mu}(t) \tag{5.10}$$

and the second-order term is:

$$\bar{\mathcal{H}}^{\Lambda_2\times\Lambda_1}_{2;1}=(2iT)^{-1}\int_{t_0^0}^{t_0^0+T}dt'\int_{t_0^0}^{t'}dt\times[\tilde{\mathcal{H}}^{\Lambda_2}_{l_2m_2\lambda_2\mu_2}(t'),\tilde{\mathcal{H}}^{\Lambda_1}_{l_1m_1\lambda_1\mu_1}(t)] \tag{5.11}$$

where the vectors **1** and **2** represents the sets of quantum numbers (l_1, m_1, λ_1, μ_1) and (l_2, m_2, λ_2, μ_2) respectively.

From this analysis and using Eq. (4.12) the following *selection rules* [58] have been derived:

1. *First-order selection rules*:

$$\bar{\mathcal{H}}^{\Lambda}_{lm\lambda\mu}=0 \quad \text{if } mn-\mu\nu\neq NZ \tag{5.12}$$

2. *Second-order selection rules*:

$$\bar{\mathcal{H}}^{\Lambda_2\times\Lambda_1}_{2;1}=0 \quad \text{if} \quad \left\{\begin{array}{l} m_1n-\mu_1\nu\neq NZ, \\ \text{and} \\ m_2n-\mu_2\nu\neq NZ, \\ \text{and} \\ (m_2+m_1)n-(\mu_2+\mu_1)\nu\neq NZ \end{array}\right\} \tag{5.13}$$

where Z is any integer, including 0.

This equations have important consequences in the symmetry-based pulse sequence theory. The selection rules permit us to know which Hamiltonian terms are *symmetry-allowed* depending upon the symmetry parameters N, n and ν.

5.1.3. Scaling Factors

The selection rules in Eqs. (5.12) and (5.13) indicate the symmetry-allowed first- or second-order terms for CN^{ν}_{n} sequences with certain values for N, n and ν. However these selection rules do not say anything about the magnitude of the allowed terms. The magnitude of the allowed terms is given by the *scaling factor* [58].

In general, a symmetry-allowed term in the first order approximation has the form:

$$\bar{\mathcal{H}}^{\Lambda}_{lm\lambda\mu}=\kappa_{lm\lambda\mu}[A^{\Lambda}_{lm}]^{R}\exp\{-im(\alpha^{0}_{RL}-\omega_r t^{0}_{0})\}T^{\Lambda}_{\lambda\mu} \tag{5.14}$$

where $\kappa_{lm\lambda\mu}$ is the scaling factor of the symmetry-allowed term with quantum numbers l, m, λ, μ. The scaling factor value depends upon the symmetry numbers and the basic element used in the construction of the sequence. The form of the scaling factor for allowed terms in the first-order effective Hamiltonian for CN^{ν}_{n} sequences is:

$$\kappa_{lm\lambda\mu}=\tau^{-1}d^{l}_{m0}(\beta_{RL})\int_{t^{0}_{0}}^{t^{0}_{0}+\tau}dt_0\,d^{\lambda}_{\mu 0}(-\beta^{0})\exp\{i(\mu\gamma^{0}+m\omega_r t^{0})\} \tag{5.15}$$

where t^0, β^0 and γ^0 refer to time points and rf Euler angles within the first pulse sequence element C.

For second-order scaling factors see [80] for RN^{ν}_{n} and CN^{ν}_{n} sequences. A general scaling factor formula for any basic element is given in [59]. A *Mathematica* [81] package, which provides scaling factors and analysis of symmetry-based pulse sequences, is available on the web (*http://www.mhl.soton.ac.uk*).

5.2. RN^{ν}_{n} Sequences

5.2.1. Definition

One possible method of implementing the time-symmetry relationships defined in Eq. (5.2) is given in Fig. 5.1. The basic element R has to be a single rf pulse or sequence of rf irradiations which induce a rotation of the nuclear spins through 180^0 about the x-axis, with a duration equal to $\tau_E = n\tau_r/N$. The basic element R can contain rf pulses of any possible phase, but the overall rotation operator must obey Eq. (5.2). Additionally, we can define R' as second basic element identical to R but changing the sign of all rf phases. A RN^{ν}_{n} sequence is constructed by concatenating $N/2$ pairs of elements $R_{\phi}R'_{\phi}$, where ϕ is an overall phase shift equal to $\pi\nu/N$ radians.

5.2.2. Average Hamiltonian and Selection Rules

Following the same procedure as in section 5.1.2 and the Euler angle symmetry for a RN^{ν}_{n} sequence, the Hamiltonian for an interaction Λ at time t_q is:

$$\tilde{\mathcal{H}}^{\Lambda}_{lm\lambda\mu}(t_q)=\tilde{\mathcal{H}}^{\Lambda}_{lm\lambda\mu}(t_0)\exp\left\{i\frac{2\pi m}{N}q\left(mn-\mu\nu-\frac{\lambda N}{2}\right)\right\} \tag{5.16}$$

The AHT can be used to analyze the interaction frame Hamiltonian, as in section 5.1.2. The following selection rules are obtained for first-order and second-order Hamiltonian terms:

1. *First-order selection rules*:

$$\bar{\mathcal{H}}^{\Lambda}_{lm\lambda\mu}=0 \quad \text{if } mn-\mu\nu\neq\frac{N}{2}Z_{\lambda} \tag{5.17}$$

2. *Second-order selection rules*:

$$\bar{\mathcal{H}}^{\Lambda}_{lm\lambda\mu}=0 \quad \text{if} \quad \left\{\begin{array}{l} m_1 n-\mu_1\nu\neq\frac{N}{2}Z_{\lambda_1}, \\ \text{and} \\ m_2 n-\mu_2\nu\neq\frac{N}{2}Z_{\lambda_2}, \\ \text{and} \\ (m_2+m_1)n-(\mu_2+\mu_1)\nu\neq\frac{N}{2}Z_{\lambda_{2+1}} \end{array}\right\} \tag{5.18}$$

where Z_{λ} indicates any integer with the same parity as λ.

5.2.3. Scaling Factors

The magnitude of the symmetry-allowed terms for a RN^{ν}_{n} sequence is given by the scaling factor, which has the form:

$$\kappa_{lm\lambda\mu}=\tau^{-1}d^{l}_{m0}(\beta_{RL})\int_{t_0^0}^{t_0^0+\tau}dt_0 d^{\lambda}_{\mu 0}(-\beta^0)\exp\{i(\mu\gamma^0-\mu\frac{\pi\nu}{N}+m\omega_r t^0)\} \tag{5.19}$$

where t^0, β^0 and γ^0 refer to time points and rf Euler angles between the first pulse sequence element *R*. The scaling factor value depends upon the symmetry numbers and the basic element used in the construction of the RN^{ν}_{n}sequence.

5.3. CRN^{ν_I,ν_S}_{n} sequences

5.3.1. Definition

In a heteronuclear system, rotor-synchronized symmetry-based sequences can be applied simultaneously on both channels at the Larmor frequencies of the spins *I* and *S*. This type of

sequence is called a dual rotor-synchronized pulse sequence. There are four types of these dual channel sequences [59].

The type of mixed C and R sequence denoted as $CRN_n^{\nu_I,\nu_S}$ is defined in Fig. 5.2. $CRN_n^{\nu_I,\nu_S}$ involves an irradiation of a CN_n^{ν} sequences on channel S and a irradiation of a RN_n^{ν} on channel I, with the same number of basic elements N and total number of rotor periods n but different parameter ν. The symmetries of the Euler angles under the rf fields are analogous to those for the single channel rotor-synchronized sequences applied on each channel:

$$\begin{aligned} \beta_q^I\left(t+\frac{n\tau_r}{N}\right) &= \beta_0^I(t) \\ \gamma_q^I\left(t+\frac{n\tau_r}{N}\right) &= \gamma_0^I(t)-\frac{2\pi\nu}{N}q \end{aligned} \tag{5.20}$$

$$\begin{aligned} \beta_q^S\left(t+\frac{n\tau_r}{N}\right) &= \beta_0^S(t)\pm q\pi \\ \gamma_q^S\left(t+\frac{n\tau_r}{N}\right) &= \gamma_0^S(t)-\frac{2\pi\nu}{N}q \end{aligned} \tag{5.21}$$

Dual sequences involve irradiation of two spin species. This fact allows the possible recoupling or no recoupling of heteronuclear terms. Therefore this kind of sequence can be used for either recoupling or decoupling. In chapter 7, the principles of dual sequences are used to explain the interference of the heteronuclear decoupling during homonuclear recoupling [75].

5.3.2. Average Hamiltonian and Selection Rules

Following the same procedure detailed in previous sections, new set of selection rules can be extracted [59]. In this case, heteronuclear terms have to be included in the Hamiltonian:

$$\hat{\mathcal{H}}_{\text{int}}(t)=\sum_{\Lambda,l,m,\lambda_I,\lambda_S}\hat{\mathcal{H}}^{\Lambda}_{lm\lambda_I 0\lambda_S 0}(t) \tag{5.22}$$

where $\hat{\mathcal{H}}^{\Lambda}_{lm\lambda_I\lambda_S}(t)$ is equal to:

$$\hat{\mathcal{H}}^{\Lambda}_{lm\lambda_I\lambda_S}(t)=\sum_{\Lambda,l,m,\lambda_I,\lambda_S}\omega_{lm}^{\Lambda_{IS}}\exp\{im\omega_r t\}\times T^{\Lambda_I}_{\lambda_I 0}T^{\Lambda_S}_{\lambda_S 0} \tag{5.23}$$

After transformation of the Eq. (5.23) into the interaction reference frames at the Larmor frequencies of spin I and S, the Hamiltonian is given by:

$$\tilde{\mathcal{H}}^{\Lambda}_{lm\lambda_I\mu_I\lambda_S\mu_S}(t_q)=\tilde{\mathcal{H}}^{\Lambda}_{lm\lambda_I\mu_I\lambda_S\mu_S}(t_0)\exp\left\{i\frac{2\pi m}{N}q\left(mn-\mu_I\nu_I-\mu_S\nu_S-\frac{\lambda_S N}{2}\right)\right\} \quad (5.24)$$

the selection rules for first- and second-order Hamiltonians are obtained:

1. *First-order selection rules*:

$$\bar{\mathcal{H}}^{\Lambda}_{lm\lambda_I\mu_I\lambda_S\mu_S}=0 \quad \text{if } mn-\mu_I\nu_I-\mu_S\nu_S\neq\frac{N}{2}Z_{\lambda_S} \quad (5.25)$$

2. *Second-order selection rules*:

$$\bar{\mathcal{H}}^{\Lambda_2\times\Lambda_1}_{2;1}=0 \quad \text{if} \quad \begin{cases} m_1 n-\mu_{I1}\nu_I-\mu_{S1}\nu_S\neq\frac{N}{2}Z_{\lambda_{I1}+\lambda_{S1}}, \\ \text{and} \\ m_2 n-\mu_{I2}\nu_I-\mu_{S2}\nu_S\neq\frac{N}{2}Z_{\lambda_{I2}+\lambda_{S2}}, \\ \text{and} \\ (m_2+m_1)n-(\mu_{I2}+\mu_{I1})\nu_I-(\mu_{S2}+\mu_{S1})\nu_S\neq\frac{N}{2}Z_{\lambda_{I2}+\lambda_{I1}+\lambda_{S2}+\lambda_{S1}} \end{cases} \quad (5.26)$$

The first-order selection rules permit a classification of the pulse sequences on the basis of their recoupling and decoupling properties.

5.3.3. Scaling Factors

The general form of a first order symmetry-allowed term is:

$$\bar{\mathcal{H}}^{\Lambda}_{lm\lambda_I\mu_I\lambda_S\mu_S}=\kappa^{IS}_{lm\lambda_I\mu_I\lambda_S\mu_S}[A^{\Lambda_{IS}}_{lm}]^R\exp\{-im(\alpha^0_{RL}-\omega_r t^0_0)\}\times T^{\Lambda_I}_{\lambda_I\mu_I}T^{\Lambda_S}_{\lambda_S\mu_S} \quad (5.27)$$

where $\kappa^{IS}_{lm\lambda_I\mu_I\lambda_S\mu_S}$ is the scaling factor of the symmetry allowed term, which determines the magnitude of the allowed term.

For the CRN^{ν_I,ν_S}_n sequence the scaling factor has the form:

$$\kappa_{lm\lambda\mu}=d^l_{m0}(\beta_{RL})\exp\{-i\mu_S\frac{\pi\nu_S}{N}\}K^{IS}_{m\lambda_I\mu_I\lambda_S\mu_S} \quad (5.28)$$

where $K^{IS}_{m\lambda_I\mu_I\lambda_S\mu_S}$ is equal to [59]:

$$K_{lm\lambda_I\mu_I\lambda_S\mu_S}=\tau^{-1}\int_{t^0_0}^{t^0_0+\tau}dt_0 d^{\lambda_I}_{\mu_I 0}(-\beta^0_I)d^{\lambda_S}_{\mu_S 0}(-\beta^0_S)\times\exp\{i(\mu_I\gamma^0_I+\mu_S\gamma^0_S+m\omega_r t^0)\} \quad (5.29)$$

where t^0, β^0_I, γ^0_I, β^0_S and γ^0_S refer to time points and rf Euler angles within the first pulse sequence element R_S and C_I.

5.4. $CN_n^{\nu_I,\nu_S}$ sequences

5.4.1. Definition

Another symmetry-based dual sequence is the type of mixed C sequence denoted as $CN_n^{\nu_I,\nu_S}$ as defined in Fig. 5.1. This sequence involves a CN_n^{ν} sequence on channel *S* and a CN_n^{ν} sequence on channel *I*, with the same number of basic elements *N* and total number of rotor periods *n* but a different winding number ν [59]. The symmetries of the Euler angles under the rf fields in both channels are analogous to those for the single channel rotor-synchronized symmetry-based sequence CN_n^{ν} (Eq.5.1).

5.4.2. Average Hamiltonian and Selection Rules

Following the same procedure detailed in previous sections, new set of selection rules can be extracted [59]:

1. *First-order selection rules*:

$$\bar{\mathcal{H}}^{\Lambda}_{lm\lambda_I\mu_I\lambda_S\mu_S}=0 \quad if\ mn-\mu_I\nu_I-\mu_S\nu_S\neq NZ \tag{5.30}$$

2. *Second-order selection rules*:

$$\bar{\mathcal{H}}^{\Lambda_2\times\Lambda_1}_{2;1}=0 \quad if \quad \left\{\begin{array}{l} m_1 n-\mu_{I1}\nu_I-\mu_{S1}\nu_S\neq NZ, \\ \text{and} \\ m_2 n-\mu_{I2}\nu_I-\mu_{S2}\nu_S\neq NZ, \\ \text{and} \\ (m_2+m_1)n-(\mu_{I2}+\mu_{I1})\nu_I-(\mu_{S2}+\mu_{S1})\nu_S\neq NZ \end{array}\right\} \tag{5.31}$$

5.4.3. Scaling Factors

For the $CN_n^{\nu_I,\nu_S}$ sequence the scaling factor has the form:

$$\kappa_{lm\lambda\mu}=d^{l}_{m0}(\beta_{RL})K^{IS}_{m\lambda_I\mu_I\lambda_S\mu_S} \tag{5.32}$$

where $K^{IS}_{m\lambda_I\mu_I\lambda_S\mu_S}$ is equal to:

$$K_{lm\lambda_I\mu_I\lambda_S\mu_S}=\tau^{-1}\int_{t_0^0}^{t_0^0+\tau} dt_0\, d^{\lambda_I}_{\mu_I 0}(-\beta_I^0)d^{\lambda_S}_{\mu_S 0}(-\beta_S^0)\times\exp\{i(\mu_I\gamma_I^0+\mu_S\gamma_S^0+m\omega_r t^0)\} \tag{5.33}$$

where t^0, β_I^0, γ_I^0, β_S^0 and γ_S^0 refer to time points and rf Euler angles within the first pulse sequence element R_S and C_I.

6. Methods

6.1. Samples

The main topic of this thesis is the development and improvement of new solid-state NMR techniques for studies of biological systems like proteins and peptides. In the development of new methodology, it is important to test these new ideas on a *simple, stable and well characterized "model compound"*. In the present section, the crystal structure of a selection of different aminoacids and organic "model compounds" will be described.

6.1.1. Diammonium Fumarate

Diammonium fumarate (DAF) (Fig. 6.1) is the salt of the organic compound fumaric

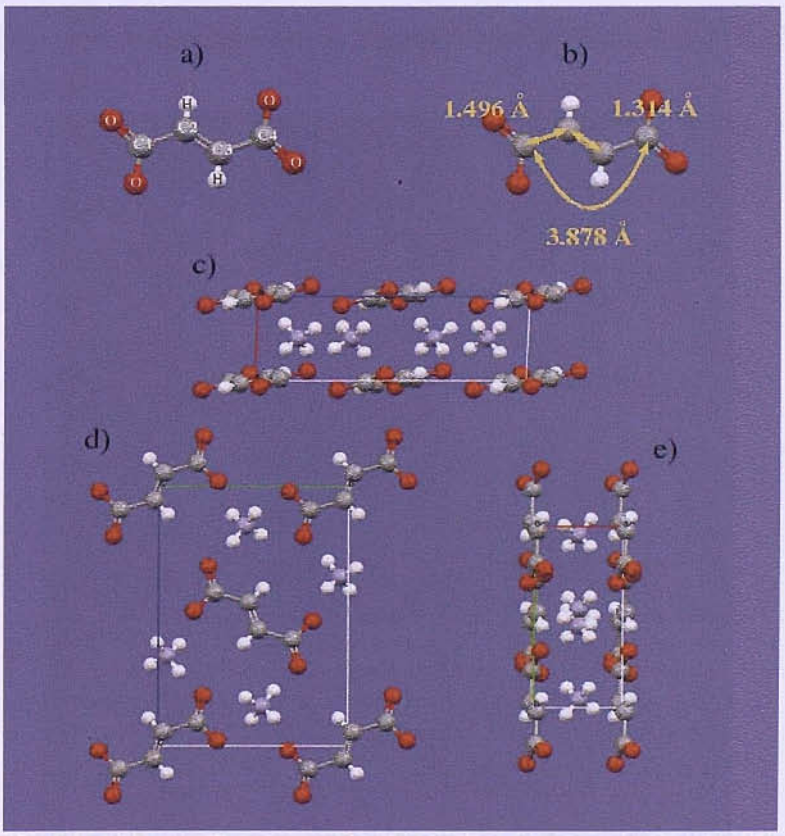

Fig. 6.1. a) Fumarate structure showing carbon atoms numbering used in this work. b) Distances between different carbon atoms in the fumarate group. c) DAF crystal structure viewed parallel to the crystallographic b-axis. d)DAF crystal structure viewed parallel to the crystallographic a-axis. e) DAF crystal structure viewed parallel to the crystallographic c-axis.

acid, a dicarboxylic acid, in which two ammonium groups substitute the protons of the acid groups. The XRD structure of diammonium fumarate (Fig. 6.1.c, d, e.)) is described in [82]. The structure file is available at the *Cambridge Structural Data Base (www.ccdc.cam.ac.uk/)* under the name NARDEP.

Diammonium fumarate selectively ^{13}C enriched in positions 2 and 3 and diluted to 10% in natural abundance DAF, diammonium [2,3-$^{13}C_2$]-fumarate (2,3-DAF), was used in the experiments described in chapter 7.

6.1.2. Glycine

Glycine is a nonpolar amino acid that contains two carbon atoms. One is in a carboxylic acid group while the α-carbon is bonded to the amino group (Fig. 6.2). Glycine is the simplest of the 20 natural amino acids. A precision neutron diffraction structure of glycine (Fig. 6.2) can be found in [83]. The structure file is available at the *Cambridge Structural Data Base (www.ccdc.cam.ac.uk/)* under the name GLYCIN03.

Some of the experiments described in chapter 7 were performed on [^{15}N, $^{13}C_2$]-glycine with 99% ^{13}C labelling.

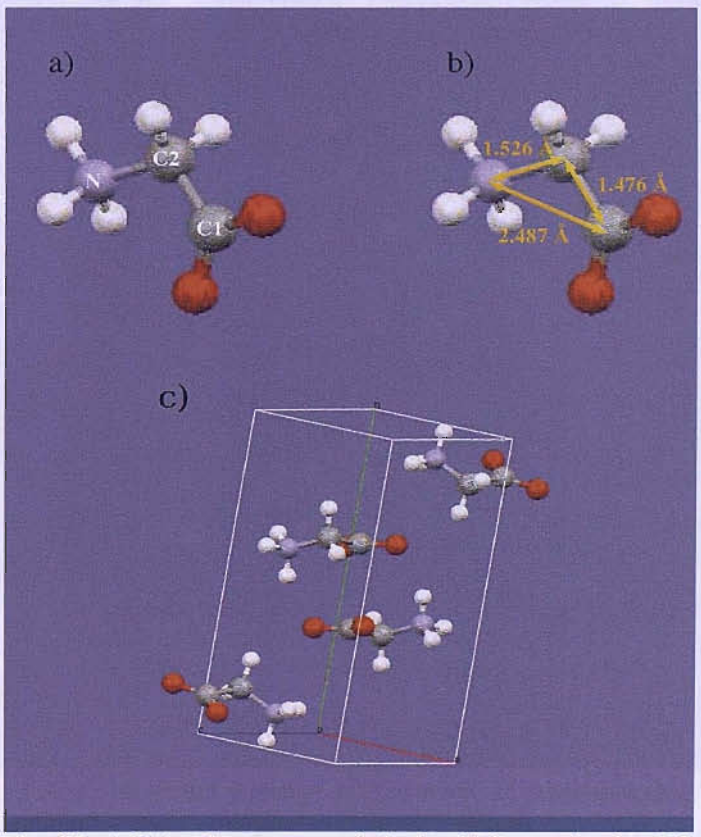

Fig. 6.2. a) Molecular structure of glycine. b) Intramolecular C-C and C-N distances in glycine. c) Crystal structure of glycine.

6.1.3. Alanine

Alanine is a common amino acid which is one of the 20 natural aminoacids. Alanine is one of the most widely used amino acids in protein construction, averaging about 9 percent of average protein composition. The molecular structure is based in a carbon chain, which is composed of three atoms of carbon. C1 forms part of the carboxylic group, C2 is attached to the amino group and a proton and C3 is a methyl group (Fig. 6.3). Precision neutron diffraction structure of L-alanine (Fig. 6.3) can be found in [84]. The structure file is available at the *Cambridge Structural Data Base (www.ccdc.cam.ac.uk/)* under the name LALNIN12.

The NMR experiments in chapter 7 were performed on [2,3-$^{13}C_2$]-L-alanine with 99% ^{13}C labelling (2,3-ALA). The experiments in chapter 8 were performed on fully ^{13}C labelled

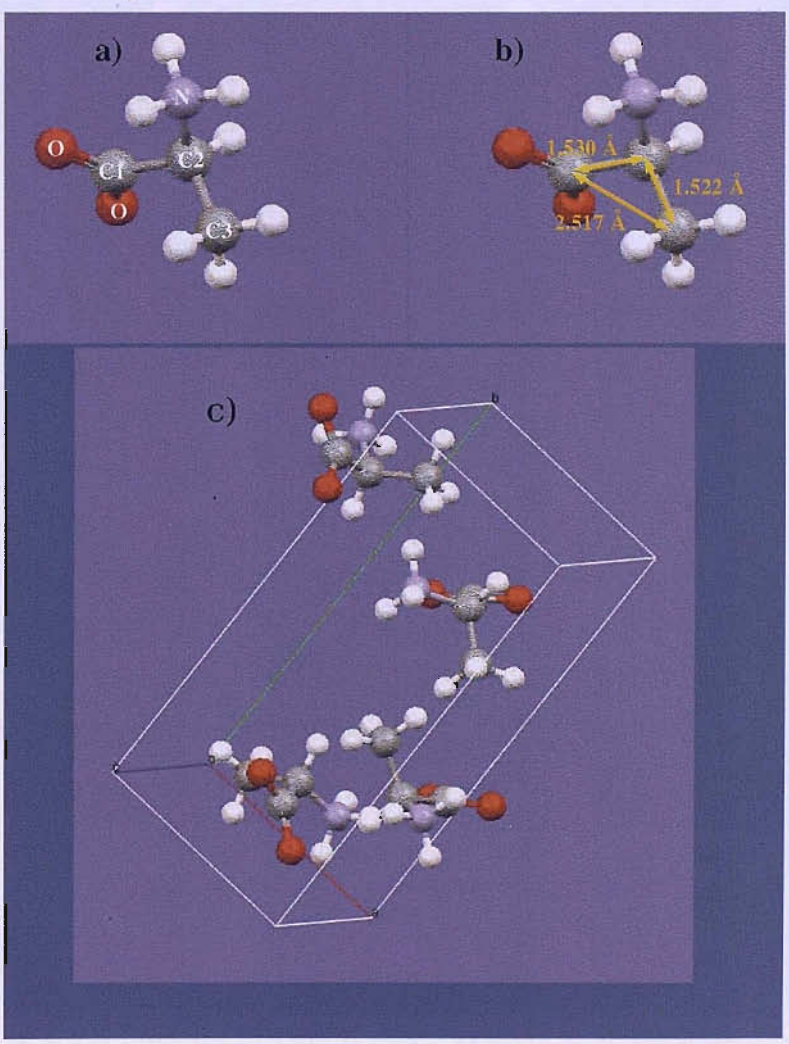

Fig. 6.3. a) Molecular structure of L-alanine. b) Intramolecular C-C distances in L-alanine. c) Crystal structure of L-alanine.

L-alanine ([2,3-$^{2}H_4$, ^{15}N, $^{13}C_3$]-alanine with 99% ^{13}C labelling).

6.1.4. Sodium Pyruvate

Sodium pyruvate (Fig. 6.4) is the sodium salt of the anionic form of the three-carbon alpha-keto acid, pyruvic acid. Pyruvate is a key compound in biological energy production because it is a key intermediate in the glycolytic and pyruvate dehydrogenase pathways.

The crystal structure of sodium pyruvate (Fig. 6.4.c.) can be found in [85]. Sodium pyruvate possesses a crystal structure formed by layers with a C-C distance between layers of approximately 3.67-3.77 Å (Fig. 6.4.d.). Pyruvate molecules within each layer face each po-

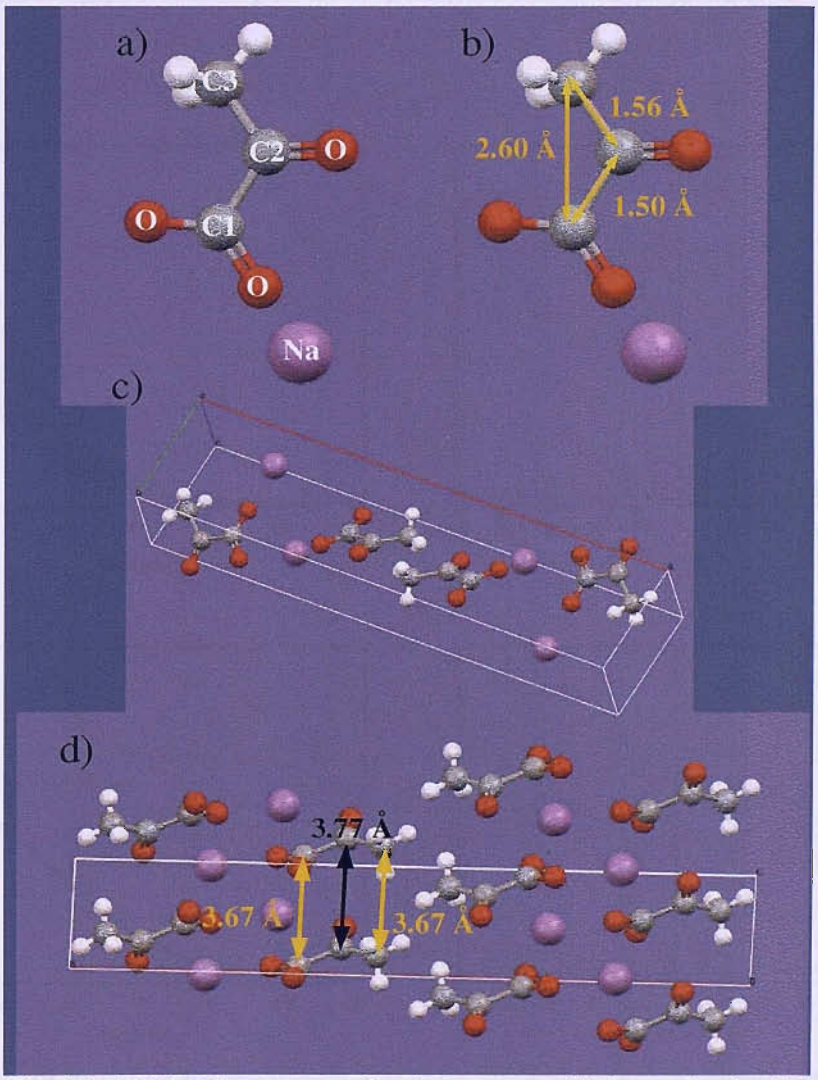

Fig. 6.4. a) Molecular structure of sodium pyruvate. b) Intramolecular C-C distances in sodium pyruvate. c) Crystal structure of sodium pyruvate. d) Intramolecular C-C distances between layers of sodium pyruvate.

lar part with the sodium in between. The structure file is available at the *Cambridge Structural Data Base (www.ccdc.cam.ac.uk/)* under the name NAPYRU01.

The experiments in chapter 8 use a fully ^{13}C labelled sample of sodium pyruvate ([$^{13}C_3$]-pyruvate) diluted in a proportion of 1/5 by natural abundance sodium pyruvate.

6.2. MAS Setup

In order to obtain high resolution in the spectrum and average out the isotropic interactions, the magic-angle has to be set with enough accuracy. The set-up of the magic-angle is done by observing a ^{79}Br MAS spectrum of potassium bromide (KBr) [52], [86].

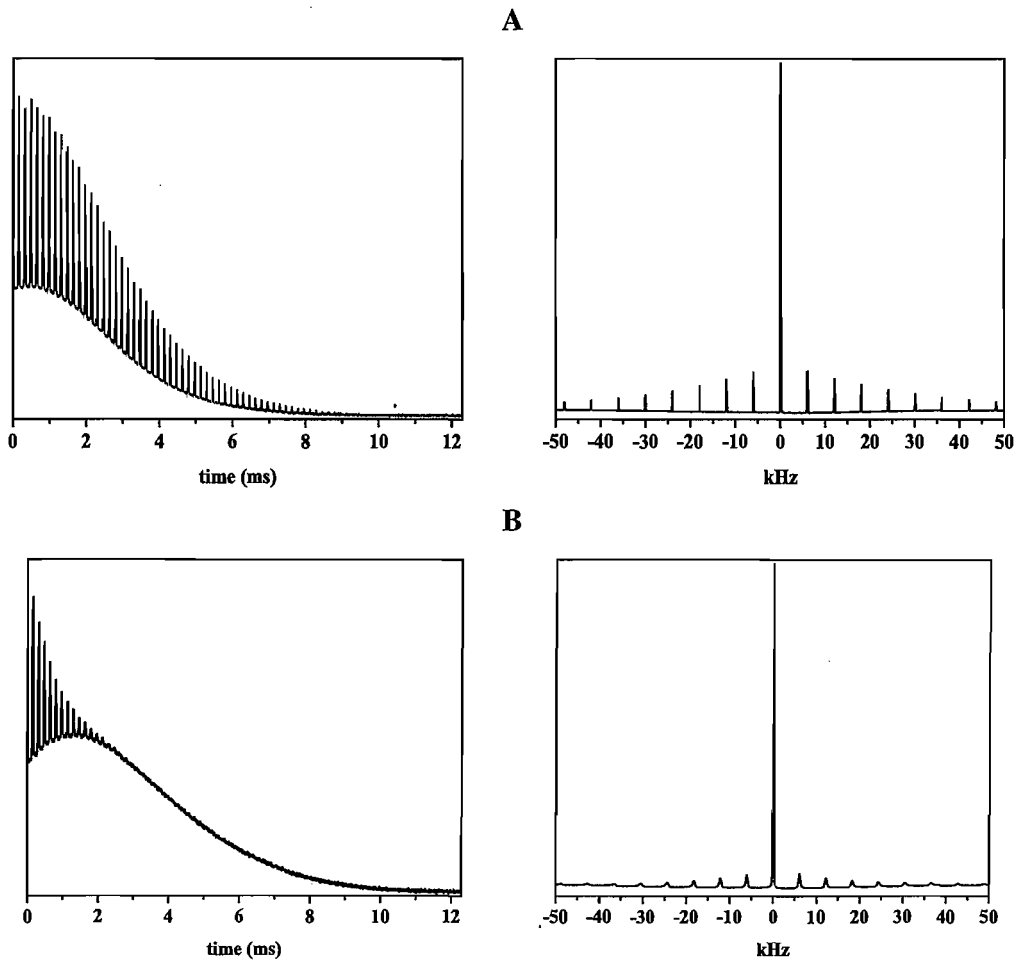

Fig. 6.5. **A.** ^{79}Br MAS FID and spectrum of KBr at the magic-angle with a spinning frequency of 7 kHz in a 400 MHz spectrometer using a 4 mm rotor. **B.** ^{79}Br MAS FID and spectrum of KBr off magic-angle with a spinning frequency of 7 kHz in a 400 MHz spectrometer, using a 4 mm rotor.

^{79}Br is an abundant quadrupolar nuclear spin with a half-integer spin quantum number (I=3/2), with a moderate quadrupole moment, and a gyromagnetic ratio very close to that of ^{13}C. KBr has a face-centered cubic crystal structure, with a small quadrupolar coupling that yields a relatively narrow line in the spectrum, leading to high sensitivity. The high sensitivity and convenient gyromagnetic ratio motivate the choice of KBr to set the magic-angle.

The ^{79}Br MAS signal of KBr is given by a single exponential decay with a number of spikes, called rotational echoes (Fig. 6.5). These rotational echoes are the result of the magnetization being refocused upon each rotor revolution and are separated by a rotor period. The frequency spectrum presents a central peak, corresponding to the central transition, and a series of small sidebands, corresponding to the rotational echoes which come from the satellite transitions (Fig. 6.5). The magic-angle can be optimized by maximizing both the number of spikes observed and their amplitudes. If the angle is away from 54.74^0 the number and intensity of the rotational echoes is reduced.

In all experiments in this thesis, the magic-angle has been adjusted by maximizing the number and amplitude of the rotational echoes observed in the ^{79}Br MAS spectrum of KBr.

6.3. Cross-Polarisation Setup

All CP experiments in this thesis have been done by using ramped-CP for cross-polarisation [55]. There are three important parameters to optimize in a ramped-CP experiment under MAS: the Hartmann-Hahn (HH) condition, the contact time and the ramp ratio (see Fig. 6.6).

To optimize the HH condition, the r.f. field intensity on the *I*-channel is fixed while the r.f. field on the *S*-channel is varied to maximize the signal, keeping the ramp equal to zero. This experiment produces a characteristic profile with bands of high polarisation separated by $n\omega_r$. The HH condition is strongly affected by molecular motion, temperature and spinning frequency. Normally, it is easier to find the condition at low spinning frequencies than at higher frequencies because dipolar interactions are removed by fast MAS. Additionally, cross-polarisation in groups with high mobility is more difficult because of the averaging of the DD-couplings by the motion. Once the HH condition has been optimized, the contact time is optimized by increasing the contact time with the ramp equal to zero until the largest signal is found. The last step is to array the ramp value in small steps until the signal is maximized.

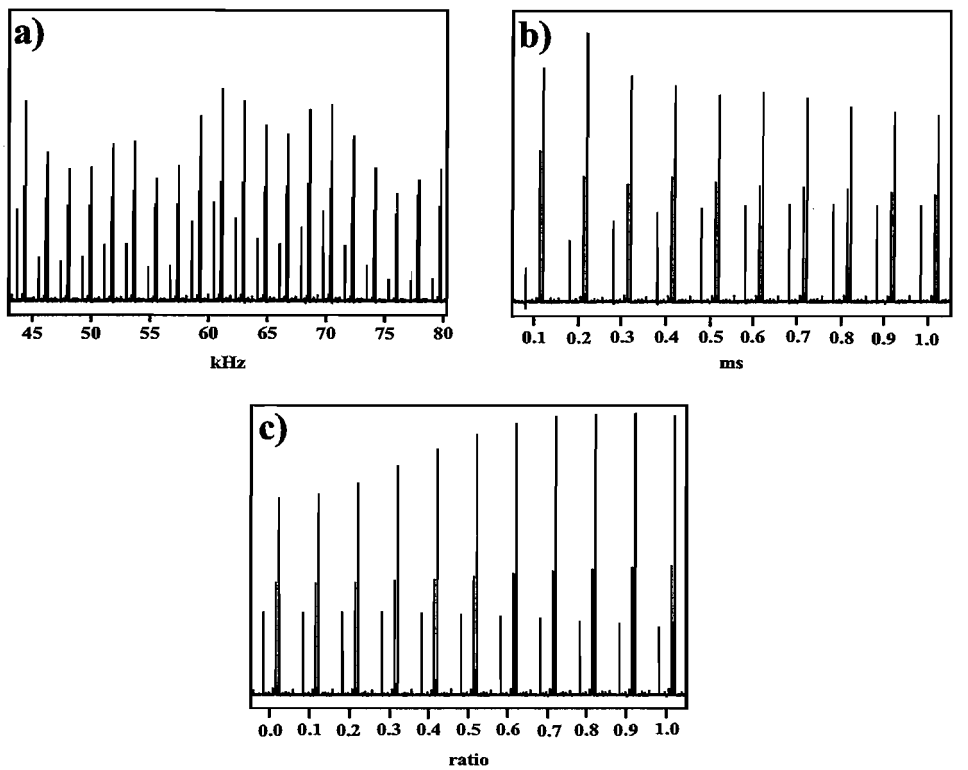

Fig. 6.6. a) Optimization of the Hartmann-Hahn condition. The figure shows the central condition of high cross-polarisation plus the first and second conditions around 52 kHz, 62 kHz and 72 kHz respectively. b) Contact time optimization. c) Optimization of the ramped ratio. This is the ratio of the amplitude value of the chosen Hartmann-Hahn condition to the maximum and minimum amplitude values contain in the ramp. All experiments were performed in a sample of U-$^{13}C_3$-alanine at $\omega_r/2\pi$ =10kHz.

6.4. Simulation Techniques

In the last thirty years, solid-state NMR has experienced an overwhelming development, involving a large repertoire of new experiments, designed to extract maximum information about the structure and dynamics of molecules in solid phases [87]. It is necessary to use *numerical simulations* to support the *experimental design, user-specific method implementation* and the *evaluation of spectral data.*

General programs have appeared in last years for simulation of NMR experiments: ANTIOPE [88], GAMMA simulation environment [89], SIMPSON [90], SPINEVOLUTION [91]. The simulations presented in this thesis have been performed using SIMPSON.

6.4.1. SIMPSON

SIMPSON [90] is a general **SIM**ulation **P**rogram for **SO**lid-state **N**MR spectroscopy and allows one to perform fast and accurate numerical simulations of solid-state NMR experiments. SIMPSON is designed to work as a *virtual spectrometer*. SIMPSON is a relatively easy to use, transparent and flexible program that uses the Tcl scripting language [92]. It has been optimised for fast calculations of multiple pulse experiments for rotating powder samples. It can also be used to test pulse sequences on relevant spin systems prior to spectrometer use. SIMPSON is available as open source software (General Public License) at `http://nmr.imsb.au.dk`.

7. Heteronuclear decoupling interference during symmetry-based homonuclear recoupling

7.1. Introduction

Recoupling methods reintroduce specific nuclear spin interactions that are normally average out by MAS, so that both the high spectral resolution afforded by MAS and the structural information provided by these nuclear spin interactions are preserved. An important set of tools to reintroduce these interactions are the symmetry-based sequences [58]. These sequences permit one to recouple selectively the interaction of interest under MAS. Particularly, two types of these sequences have been developed: CN_n^ν [59], [66], [69] and RN_n^ν sequences [59], [70].

Many important applications of symmetry-based sequences involve DQ homonuclear dipolar recoupling. These applications include two-dimensional DQ correlation spectroscopy [64], [68], [93], [94], [95], [96], [97], high-order multiple-quantum excitation in solids [98], [99], [100], [101], and the estimation of internuclear distances [41], [102], torsional angles [103], [104], [105], and motional order parameters [106].

In solid organic and biological samples, most of the applications of DQ dipolar recoupling concern ^{13}C nuclei introduced by isotopic labelling. In these samples, the ^{13}C nuclei experience strong ^{13}C-^{13}C homonuclear interactions accompanied by strong ^{1}H-^{13}C heteronuclear interactions. These ^{1}H-^{13}C heteronuclear interactions interfere with the ^{13}C-^{13}C homonuclear interactions, reducing the efficiency of the recoupling. This interference is suppressed normally by irradiating with a strong resonant rf field on ^{1}H while the recoupling is performed on the ^{13}C channel. The usual regime in this experiment is to maintain the spinning frequency low (up to 6 kHz), keeping a ratio of 2.5, or higher, between the ^{1}H rf field and the ^{13}C rf field[64], [68], [107]. In solid-state NMR, there is a movement to higher spinning frequencies and higher magnetic fields in order to get better resolution and sensitivity. The approach described above is not feasible for high MAS frequencies (around 10 kHz or more), since the required RF field on the ^{1}H channel would be unacceptably high.

One approach is to use symmetry-based sequences with lower ratios of ^{13}C nutation frequency to MAS frequency [108]. The disadvantage of this approach is that the required sequences have relatively small scaling factors and they are less robust with respect rf in-

homogeneity, and CSA interactions. Ishii [109] showed that for the pulse sequence fpRFDR (finite-pulse radio-frequency driven recoupling), it is possible to have good homonuclear dipolar recoupling at very high spinning frequencies (from 30 kHz). However, many solid-state NMR applications require relatively large sample volumes, for which the maximum available spinning frequencies are currently limited to around 15 kHz.

Hughes et al. [110] demonstrated that the ^{13}C DQ filtering efficiency obtained with a sequence without ^{1}H decoupling at 12 kHz spinning frequency was comparable to that obtained with high power ^{1}H decoupling at 7 kHz spinning frequency. This suggests that the no-decoupling regime appears at conveniently low spinning frequencies for the symmetry-based pulse sequences. This makes sense, since the symmetry-based design of these sequences ensures their high compensation for CSA, and by extension, for heteronuclear interactions in the absence of heteronuclear decoupling.

In this thesis, an experimental and theoretical investigation of heteronuclear interference during ^{13}C homonuclear dipolar recoupling, for the case of double-quantum homonuclear recoupling pulse sequences of the symmetry class CN_n^{ν} and RN_n^{ν} is presented (results for RN_n^{ν} have been published [75]). The effects of the spinning frequency, nutation frequency on both the ^{1}H and ^{13}C channels, and the symmetry numbers, is explored in both cases. Also, a study of the robustness of this sequences in the regime of no ^{1}H decoupling against rf inhomogeneity and phase transients is shown.

The work presented in this chapter has been done in collaboration with of D. H. Brouwer, G. Antonioli, A. Brinkmann and M. H. Levitt.

7.2. Heteronuclear decoupling interference during recoupling with RN_n^{ν} sequences.

7.2.1. Pulse sequence

The RN_n^{ν} sequences (see Fig. 7.1) used for dipolar recoupling belong to a series of sequences with symmetry numbers $RN_2^{(-1+N/2)}$ with N being an even number greater or equal to 12. Sequences of the series $RN_2^{(-1+N/2)}$ have been successfully used in distance measurements [102], [41], [33].

The basic element used in these sequences is a composite π-pulse:

$$R_0=R'_0=90_0270_{180} \tag{7.1}$$

with the flip angles and phases given in degrees. This basic element is particularly robust with respect to the chemical shift. The $RN_2^{(-1+N/2)}$ sequence is built of *N/2* pairs of elements $R_\phi R'_{-\phi}$, where $\phi=\frac{\pi((N/2)-1)}{N}$:

$$RN_\nu^{(-1+N/2)}=[R_\phi R'_\phi]^{N/2} \tag{7.2}$$

The nutation frequency is set so that one $RN_2^{(-1+N/2)}$ element occupies 2 rotor periods. In this case, the nutation frequency is exactly:

$$\omega_{nut}^{^{13}C}=\frac{N}{2}\omega_r \tag{7.3}$$

where ω_r is the spinning frequency.

A symmetry analysis of this series of sequences shows that first-order symmetry-allowed terms are of the form {l, m, λ, μ}= {2, -1, 2, 2}, {l, m, λ, μ}= {2, 1, 2, -2} (homonuclear dipolar double-quantum terms) and {l, m, λ, μ}= {0, 0, 0, 0} (homonuclear *J*-coupling terms). The scaling factors for each allowed term are indicated in Table 7.1. These scaling factors depend on the basic element, and symmetry numbers. However for the sequences $RN_2^{(-1+N/2)}$ with *N* greater or equal to 12, the scaling factors for the different allowed terms remain always equal.

Table 7.1. Symmetry-allowed first-order Hamiltonian terms and scaling factors of the series of sequences $RN_2^{(-1+N/2)}$ with *N* greater or equal to 12.

Symmetry-allowed first-order terms	DD {2, -1}, {2, 2}	DD {2, 1}, {2, -2}	J-couplings {0, 0}, {0, 0}
Scaling factors	0.17	0.17	1

Table 7.2.Number of second-order allowed terms for the sequence $R20_2^9$.

Symmetry-allowed second-order terms	DD	CSA	isoCS	rf	J
DD	44	20	4	4	0
CSA	20	8	0	0	12
isoCS	4	0	2	0	3
rf	4	0	0	2	2
J	0	12	3	2	0

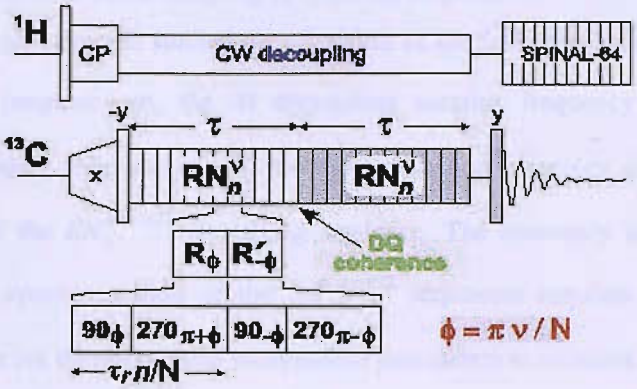

Fig. 7.1. Pulse sequence diagram for ^{13}C double-quantum homonuclear dipolar recoupling with a symmetry-based RN_n^ν recoupling sequence.

These sequences present a relatively low number of second order symmetry-allowed terms, producing a double-quantum dipolar recoupling that is quite clean and without too much interference from CSA-DD cross terms [70] (see Table 7.2). Also, these sequences are well compensated against offset effects in the ^{13}C carrier and rf imperfections [70]. However, these sequences are quite sensitive to the phase shift accuracy and the parameter ϕ has to be experimentally adjusted.

These sequences are incorporated into a double-quantum filtered (DQF) experiment as shown in Fig. 7.1. First, the proton magnetization is converted to transverse magnetization by applying a $\pi/2$ pulse of phase $\pi/2$. The ^{13}C transverse magnetization is enhanced by conventional ramped cross-polarisation from the protons, using simultaneous fields of phase 0 on the two channels. The ramp on ^{13}C-spin field improves reproducibility. A strong $\pi/2$ pulse on the ^{13}C channel transforms the transverse magnetization into longitudinal magnetization parallel to the main magnetization field. For a two-spin system, a R sequence of duration τ converts z-magnetization into double-quantum coherence. A second R sequence of duration τ, reconverts the double-quantum coherence into longitudinal magnetization. These elements have an additional overall phase shift $\Phi = \{\pi/2, \pi, 3\pi/2, 0\}$ in consecutive experiments, which selects NMR signals passing through double-quantum coherence. These two R sequences form the double-quantum filter. A final $\pi/2$ pulse with phase $\pi/2$ transforms the longitudinal magnetization into transverse magnetization. Precession of the trans-

verse magnetization induces a NMR signal, whose Fourier transform is the NMR spectrum. During the R sequences on the ^{13}C channel, we applied continuous wave (CW) decoupling on the ^{1}H channel and SPINAL decoupling [51] during acquisition.

The recoupling efficiency is studied as a function of the following parameters: the magic-angle-spinning frequency ω_r, the ^{1}H decoupling nutation frequency $\omega_{nut}^{^{1}H}$ during the homonuclear recoupling sequence, the ^{13}C recoupling nutation frequency $\omega_{nut}^{^{13}C}$, and the symmetry number N of the $RN_n^{-1+N/2}$ recoupling sequence. The symmetry number n is held fixed at n=2. The synchronization of the $RN_n^{-1+N/2}$ sequences requires the relationship $\omega_{nut}^{^{13}C} = N\omega_r/n$. There are therefore three independent parameters to consider.

7.2.2. Experimental

For all of the results presented below, the DQ efficiencies were estimated by the following procedure. For a given $RN_n^{-1+N/2}$ sequence and spinning frequency ω_r, the number of R elements giving the maximum DQF signal was determined. This number was held fixed while the efficiency was optimized by small adjustments to the ^{13}C RF power and R element phase shift ϕ (see Appendix B) . Once optimized, a series of ^{13}C DQ filtered spectra were obtained (with eight acquisitions each), with the strength of the ^{1}H decoupling during ^{13}C homonuclear recoupling incremented from 0 to 120 kHz in increments of 3 kHz. The DQ filtering efficiencies were calculated by comparing the integrals of the DQ filtered spectra to a cross-polarization spectrum obtained under identical conditions.

A range of MAS frequencies between 6 and 20 kHz and a series of $RN_n^{-1+N/2}$ sequences with n = 2, N = 12, 14, 16..., 40 and ν =−1+N/2 were studied. All experiments were performed in a field of 9.4 T using 3.2 mm zirconia rotors on a Varian *InfinityPlus* console. The ^{1}H nutation frequency during the SPINAL-64 decoupling sequence applied during signal acquisition was fixed at 100 kHz.

The experiments were performed on three of the model organic compounds described in chapter 6: diammonium-[2,3-$^{13}C_2$]fumarate diluted to 10% in natural abundance diammonium fumarate (DAF), [^{15}N,$^{13}C_2$]glycine with 99% ^{15}N and ^{13}C labelling (Gly), and [2,3-$^{13}C_2$] alanine with 99% ^{13}C labelling (Ala). These compounds broadly represent typical classes of ^{13}C spin systems involving CH, CH_2, and CH_3 groups, respectively. Fig. 7.2 shows the CP and DQF spectrum of each compound together with the chemical structure of each com-

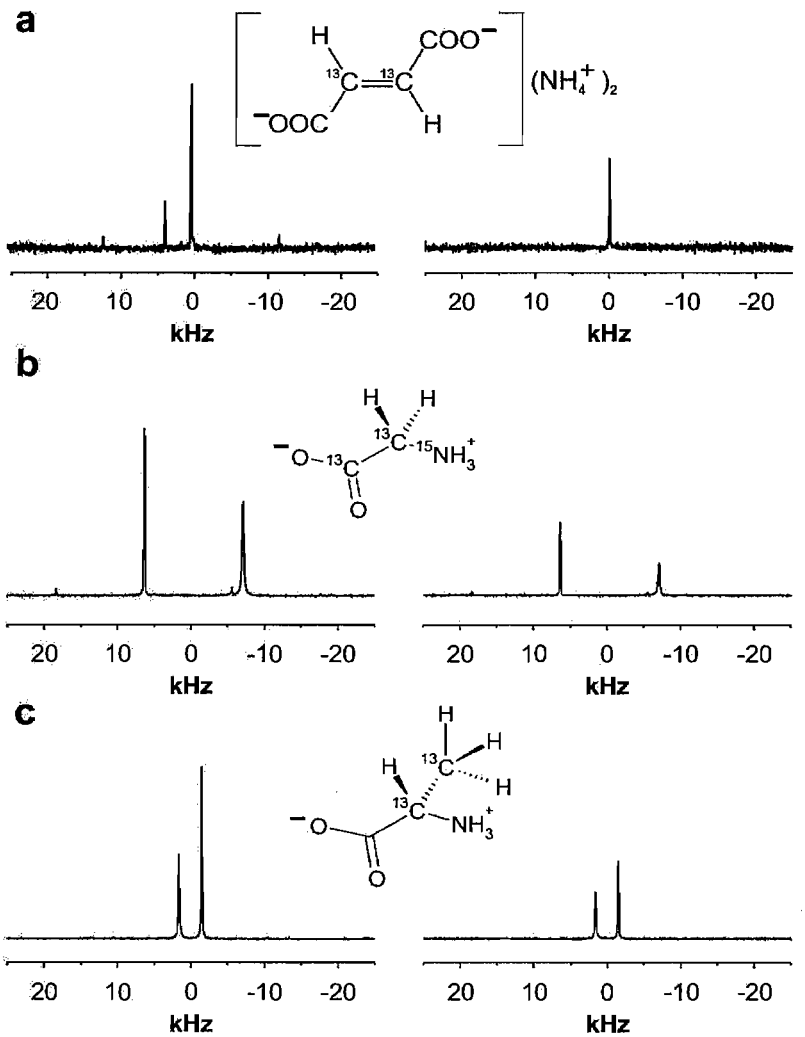

Fig. 7.2. Comparison of ^{13}C CP MAS NMR spectra with double quantum filtered spectra for: a) 10% labelled diammonium-[2,3-$^{13}C_2$]fumarate (DAF), b) [^{15}N,$^{13}C_2$]glycine and c) [2,3-$^{13}C_2$]alanine. The CP MAS NMR spectra are shown on the left column while the DQF spectra are shown on the right column.

pound.

7.2.3. Results

Diammonium-[2,3-$^{13}C_2$]fumarate:

In Fig. 7.3, the effect of the ^{1}H decoupling nutation frequency on the ^{13}C DQ filtering efficiency for 2,3-DAF at spinning frequencies of 6 and 12 kHz is shown. At a spinning frequency of 6 kHz (Fig. 7.3.a), sequences with low ^{13}C nutation frequency, whose symmetry numbers N have smaller values, present the typical behaviour in which the best DQ filtering

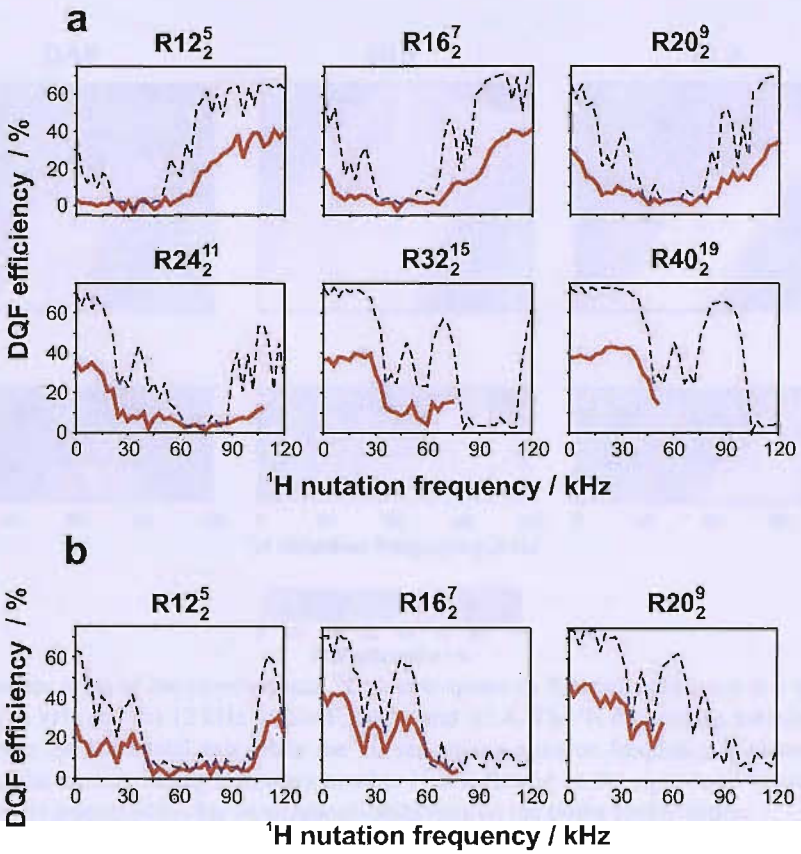

Fig. 7.3. Plots showing ^{13}C double-quantum filtered recoupling efficiency vs. ^{1}H decoupling nutation frequency for DAF at a) $\omega_r/2\pi$ = 6 kHz and b) $\omega_r/2\pi$ = 12 kHz. The recoupling sequence used in each case is indicated above each plot. The simulated data shown by the dashed blue line, while the experimental data is plotted as a solid red line. Some of the experimental data sets are incomplete due to limitations in the total RF power that can be delivered to the probe.

efficiency is achieved at a large value of the ^{1}H decoupling field. However, as the symmetry number N increases, and the ^{13}C nutation frequency is increased, the DQ filtering efficiency increases when no ^{1}H decoupling is applied. For the sequence with the largest N values ($R40_2^{19}$), and therefore the largest ^{13}C nutation frequency, the DQ filtering efficiency without ^{1}H decoupling is 37% and is comparable to the 40% recoupling efficiency obtained with the lowest N and maximum ^{1}H decoupling power $R12_2^5$. This result is quite important, since it means that it is possible to get good DQ filtering efficiency with no ^{1}H decoupling at all at low spinning frequencies. The regime of no decoupling is not restricted to high spinning frequencies but is also available if a high enough ^{13}C nutation frequency is chosen.

For $\omega_r/2\pi$=12 kHz (Fig. 7.3.b), the behaviour of the ^{13}C DQ filtering efficiency with respect to the ^{1}H decoupling interference follows the same trend as the one at 6 kHz spinning

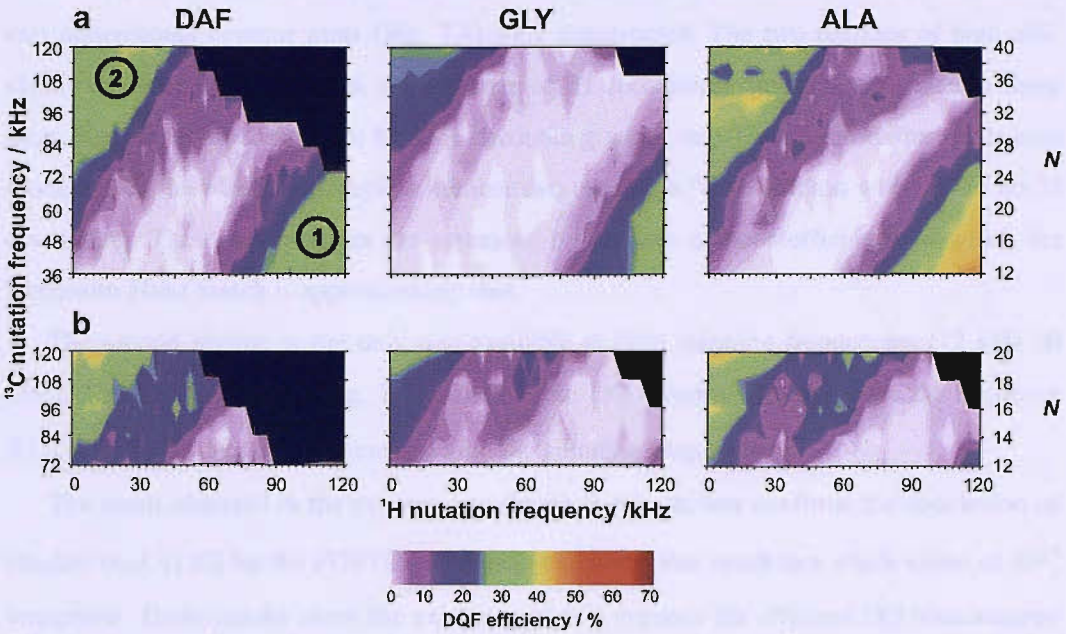

Fig. 7.4. Contour plots of the experimental ^{13}C double-quantum filtering efficiency at a spinning frequency of (a) 6 kHz and (b) 12 kHz for DAF, GLY, and ALA. The ^{1}H decoupling nutation frequency is plotted along the horizontal axis while the ^{13}C recoupling nutation frequency is plotted along the vertical axis. The corresponding symmetry number N is indicated on the right-hand vertical axis. The black regions are inaccessible, due to technical limitations on the probe performance.

frequency. However, the area of good decoupling is displaced to higher values of ^{13}C nutation frequency, making inaccessible regime number 2 for medium/high spinning frequencies (see Fig. 7.4). A respectable DQ filtering efficiency of 48% was achieved at $\omega_r/2\pi$=12 kHz using the sequence $R20_2^9$ without ^{1}H decoupling.

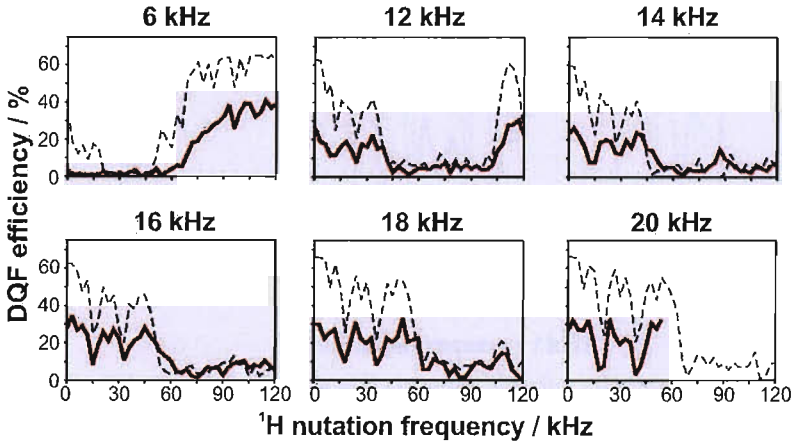

Fig. 7.5. Double-quantum filtering efficiencies for DAF using the recoupling sequence $R12_2^5$ as a function of the ^{1}H decoupling nutation frequency, at the indicated MAS frequencies. The experimental and simulated data are plotted as solid and dashed lines, respectively.

To display all these observations in a better format for the entire series of sequences, two dimensional contour plots (Fig. 7.4) were constructed. The two regimes of high efficiency of dipolar recoupling in the presence of ^{1}H decoupling can be clearly seen in these plots. Regime number one uses high ^{1}H decoupling while the ^{13}C nutation frequency is kept moderate. In the other hand, regime number two uses high ^{13}C irradiation with low or no ^{1}H decoupling. These two regimes are separated by an area of poor efficiency in which the Hartmann-Hahn match is approximately met.

The second regime is the only one available at high spinning frequencies (12 kHz-20 kHz). This can be seen in Fig. 7.7, in which the DQ filtering efficiency for the sequence $R12_2^5$ with no ^{1}H decoupling increases with the spinning frequency.

The result obtained in the experiments shown in this section confirms the conclusion of Hughes et al. [110] for the POSTC7 sequence, extending this result to a whole series of RN_n^ν sequences. These results show the existence of two regimes for efficient DQ homonuclear dipolar recoupling in presence of ^{1}H decoupling, separated by an area of poor efficiency which is close to the Hartmann-Hahn condition. The regime without proton decoupling allows good recoupling at moderate to high spinning frequency. This regime is quite conveni-

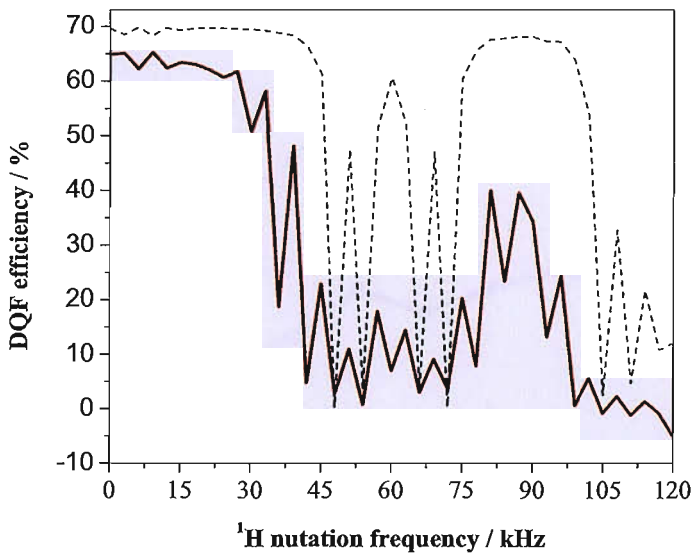

Fig. 7.6. Simulations of double-quantum filtering efficiencies with respect to the ^{1}H nutation frequency for two models of GLY, using the recoupling sequence $R40_2^{19}$. In the simulation represented in solid red, the GLY model includes the ^{1}H-^{1}H dipolar interactions. However, in the simulation shown by the dotted blue line, the GLY model used in the simulation has all ^{1}H-^{1}H dipolar interactions set to zero.

ent for biological samples, and it is expected to become popular in this field.

[^{15}N,$^{13}C_2$]Glycine:

The same studies were done for [^{15}N,^{13}C2]glycine for the same series of sequences and MAS frequencies. From Fig. 7.4, it can be shown that the behaviour of the ^{13}C DQ filtering efficiency in the presence of ^{1}H decoupling is qualitatively similar to that of 2,3DAF, but the region of poor decoupling is much broader. This is due to the strong ^{13}C-^{1}H homonuclear coupling of the two protons in the CH_2 systems but mainly to the stronger ^{1}H-^{1}H interactions as can be seen in the simulations shown in Fig. 7.6. Nonetheless, it was still possible to achieve a DQ filtering efficiency of 36% for glycine using the $R20_2^9$ sequence with no ^{1}H decoupling at 12 kHz spinning frequency and 18% using the $R12_2^5$ sequence with no ^{1}H decoupling at 20 kHz.

[2,3-$^{13}C_2$]alanine:

In this case, the data is similar to the 2,3DAF data but it was possible to achieve higher values of DQ filtering efficiency (48% using the $R20_2^9$ sequence with no ^{1}H decoupling at 12 kHz spinning frequency), since the ^{1}H–^{1}H homonuclear and ^{1}H-^{13}C heteronuclear interac-

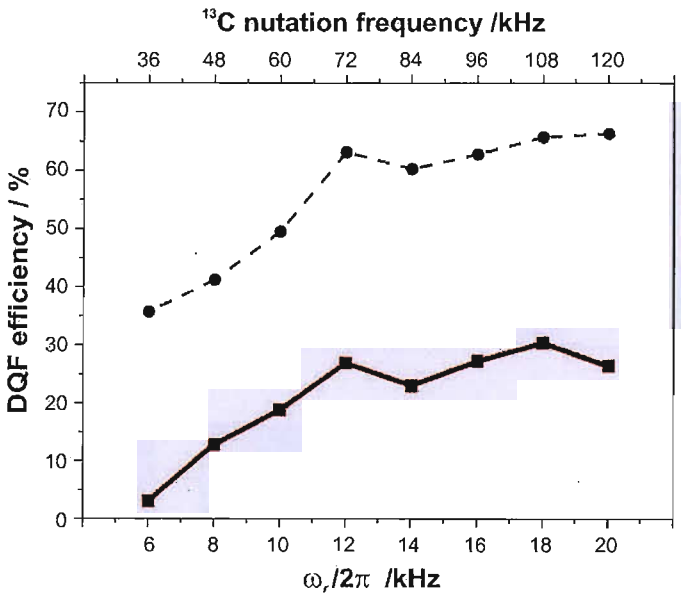

Fig. 7.7. Double-quantum filtering efficiencies for DAF using the recoupling sequence $R12_2^5$, without ^{1}H decoupling. The spinning frequency $\omega_r/2\pi$ is varied along the horizontal axis. The corresponding ^{13}C recoupling nutation frequency is given by $\omega_{nut}^{^{13}C}=6\omega_r$ for all points. The experimental and simulated data are plotted as solid and dashed lines, respectively.

tions are relatively weak due to the rapid rotation of the CH_3 group.

7.2.4. Numerical Simulations

Simulations of the effects of ^{1}H decoupling on ^{13}C homonuclear recoupling were performed using the SIMPSON platform [90]. The simulations considered the ^{13}C nuclei and their directly-attached ^{1}H nuclei in a single molecule of DAF, Gly, or Ala, ignoring the protons attached to nitrogens, the ^{15}N nucleus (in the case of Gly) and all intermolecular interactions. SIMPSON input files, containing full details of the simulated spin systems are provided in Appendix C. The results of these simulations are shown together with the experimental data in Fig. 7.3, Fig. 7.5, Fig. 7.6 and Fig. 7.7. The full set of simulations are displayed as contour plots in Fig. 7.8 to facilitate comparison with the experimental data displayed in Fig. 7.4.

The simulated efficiencies were typically 20–40% higher than those observed experimentally. This discrepancy may be attributed to long-range spin–spin interactions, instrumental imperfections (such as phase transients and RF inhomogeneity) and incoherent relaxation. Despite the discrepancy in the overall scale, all the main experimental trends are reproduced qualitatively in the simulations, including the existence of the two regimes, the

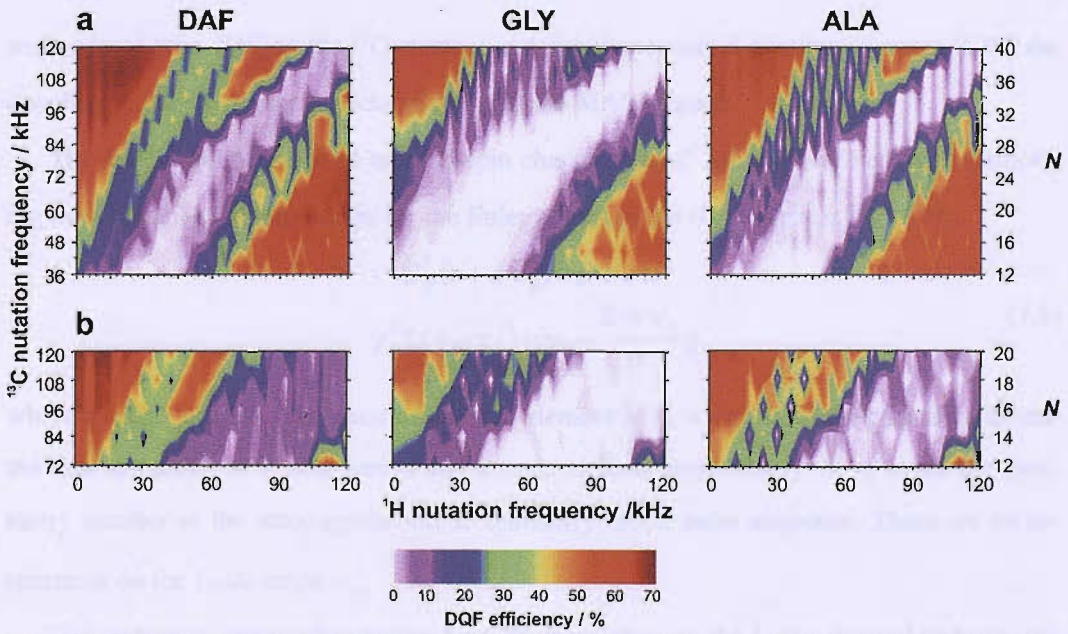

Fig. 7.8. Contour plots of the simulated ^{13}C double-quantum filtering efficiency at a spinning frequency of (a) 6 kHz and (b) 12 kHz for DAF, GLY, and ALA. The ^{1}H decoupling nutation frequency is plotted along the horizontal axis while the ^{13}C recoupling nutation frequency is plotted along the vertical axis. The corresponding symmetry number N is indicated on the right-hand vertical axis.

differences between Gly and the other compounds, and the periodic structures in the plots of DQ filtering efficiency vs. ^{1}H decoupling nutation frequency observed at high spinning frequency.

It has been verified by simulation that the large homonuclear coupling between the two H^{α} protons is responsible for the different behaviour of glycine, compared to DAF and Ala. If the ^{1}H–^{1}H coupling is removed, the simulated glycine plot is similar to that of DAF (Fig. 7.6).

7.2.5. Theory

The problem has been addressed using first-order Hamiltonian theory. The first-order Hamiltonian theory provides a sufficient framework to understand many of the features. In section 7.2.4, it is shown that the ^{1}H-^{1}H homonuclear couplings have a significant effect on the ^{13}C-^{13}C homonuclear dipolar recoupling. However, these effects appear as a secondary distortion and the main features observed in the contour plots can be explained by first-order Hamiltonian theory.

According to the results obtained in previous section and the pulse sequence scheme applied, it can be supposed that the sequence is a dual-channel rotor-synchronized pulse sequence. In the present case, this dual sequence is composed of a symmetry-based recoupling sequence of type RN_n^{ν} in the ^{13}C channel and simultaneously a continuous wave (CW) decoupling in the ^{1}H channel synchronized with the MAS rotation.

The RN_n^{ν} sequence applied to the *S*-spin channel ("rare" spins) is defined by the following time-symmetry relationships for the Euler angles of the rf propagator [58], [59]:

$$\begin{aligned} \beta_{rf}^{S}(t+q\tau_R) &= \beta + q\pi \\ \gamma_{rf}^{S}(t+q\tau_R) &= \gamma_0 - \frac{2\pi\nu_S}{N}q \end{aligned} \tag{7.1}$$

where q = 0, 1, ..., *N*-1. The duration of each element is $\tau_E = n\tau_R/N$, where τ_R and τ_E denote the time durations of a rotor period and a basic element respectively. *N*, *n*, ν_s are the symmetry number of the rotor-synchronized symmetry-based pulse sequence. There are no restrictions on the Euler angle α_{rf}^{S}.

The symmetry relationship angles for CW decoupling on the *I*-spin channel ("abundant" spins) need to be derived. A propagator can be described as a rotation through the Euler angles:

$$U_{rf}^{I}(t_q,t_0^0)=R_z^I(\alpha_{rf}^I)R_y^I(\beta_{rf}^I)R_z^I(\gamma_{rf}^I) \tag{7.2}$$

Also, assuming the phase of the decoupling field is equal to zero, the propagator for CW decoupling can be represented by:

$$U_{rf}^{I}(t_q,t_0^0)=\exp[-i\beta\omega_{rf}^I(t_q-t_0^0)I_x] \tag{7.3}$$

It proves convenient to express the *I*-spin rotation in an analogous form to the *S*-spin rotation. If an additional -π/2 rotation of the *I*-spin is introduced, we may write:

$$U_{rf}^{I}(t_q,t_0^0)R_y^I(-\pi/2)=R_z^I(\alpha_{rf}^I)R_y^I(\beta_{rf}^I)R_z^I(\gamma_{rf}^I) \tag{7.4}$$

Combining Eq.7.3 and Eq.7.4 and applying rotation sandwich relationships [6] the propagator for CW decoupling is given by:

$$\begin{aligned}U_{rf}^{I}(t_q,t_0^0)R_y^I(-\pi/2)=R_z^I(\alpha_{rf}^I)R_y^I(\beta_{rf}^I)R_z^I(\gamma_{rf}^I)=\exp[-i\beta\omega_{rf}^I(t_q-t_0^0)I_x]=\\ \exp[i\frac{\pi}{2}I_y]\exp[-i\beta\omega_{rf}^I(t_q-t_0^0)I_z]\exp[-i\frac{\pi}{2}I_y]\end{aligned} \tag{7.5}$$

From this relationship we can deduce the Euler angles:

$$\begin{aligned}\alpha_{rf}^I&=0\\ \beta_{rf}^I&=-\frac{\pi}{2}\\ \gamma_{rf}^I(t)&=-\omega_{rf}^I(t_q-t_0^0)\end{aligned} \tag{7.6}$$

This set of Euler angles does not show any time-symmetry dependence. However imposing the time-symmetry relationships: $t_q=t_0+q\tau_E$ and $\omega_{rf}^I n\tau_R=2\pi\nu_I$, the Euler angles assume the following time symmetry:

$$\begin{aligned}\beta_{rf}^I(t+q\tau_R)&=-\beta_{rf}^I(t)\\ \gamma_{rf}^I(t+q\tau_R)&=-\omega_{rf}^I(t_q-t_0^0)-\frac{2\pi}{N}\nu_I\end{aligned} \tag{7.7}$$

The time-symmetry of the Euler angles for CW decoupling is the same as for *C*-symmetry [58], [59]. The combination of the time relationships in Eq.(7.1) and Eq.(7.7) therefore defines a dual $CRN_n^{\nu_I,\nu_S}$ sequence on the *IS* spin system. Therefore, the effect of decoupling on DQ recoupling of *S*-spins can be investigated by following the theory developed for dual rotor-synchronized symmetry-based recoupling pulse sequences, providing

that the decoupling nutation frequency is $\omega_{rf}^{I} n \tau_R = 2\pi \nu_I$, and that the additional $\pi/2$ rotation given in Eq.(7.4) is included. In general, any rf field which does not fulfil Eq.(7.4) may be analysed by splitting the *I*-spin RF field term into two parts: a large part which fulfils Eq. (7.4), and a smaller perturbation term which is incorporated into the average Hamiltonian. To avoid this complication in the analysis, we supposed rf fields with an integer number of ν_I.

The first-order selection rule for a dual rotor-synchronized sequence of the type $CRN_n^{\nu_I,\nu_S}$ is given in Eq.(5.25). This selection rule gives the symmetry allowed first-order Hamiltonian terms as a function of the numbers (N, n, ν_I, ν_S) if the *I*-spin nutation frequency is an integer multiple of the spinning frequency. Additionally, the magnitude of the heteronuclear dipolar allowed-terms is given by the scaling factors $\kappa^{IS}_{2,m,1,\mu_I,1,\mu_S}$, which can be calculated in our case by Eq.(5.28). In general, for each combination of (N, n, ν_I, ν_S), several heteronuclear dipolar terms are allowed. A heteronuclear interference factor can be defined by taking the root-sum-square of the symmetry-allowed scaling factors:

$$\Re = \Re(N, n, \nu_I, \nu_S) = \left[\sum_{m,\mu_I,\mu_S} \left| \kappa_{2,m,1,\mu_I,\mu_S}(CRN_n^{\nu_I,\nu_S}) \right|^2 \right]^{1/2} \tag{7.8}$$

where the sum is taken over all symmetry-allowed combinations of quantum numbers (m, μ_S, μ_I). By calculating the number of heteronuclear allowed-terms and the heteronuclear interference factors for each combination of symmetry number (N, n, ν_I, ν_S), it is possible to

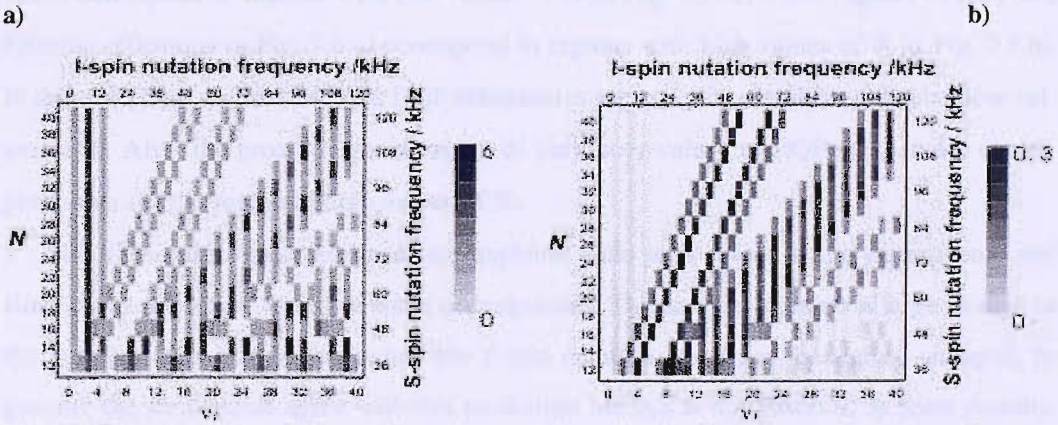

Fig. 7.9. a) Contour plot of the number of heteronuclear dipolar allowed-terms plotted as a function of the symmetry numbers ν_I and N, for the sets of sequences $CRN_n^{\nu_I,\nu_S}$, with n = 2 and ν_S = -1+N/2. The chosen parameter space corresponds to the simulation conditions in Fig. 7.8. The nutation frequencies for *S*-spin and *I*-spin at MAS frequency of 6 kHz are indicated in the right and top edges of the plot, respectively. b) This figure shows the heteronuclear recoupling factors $\Re$, as defined in Eq. (7.2), corresponding to the heteronuclear dipolar allowed-terms shown in Fig. 7.8.a).

evaluate the importance of these heteronuclear allowed-terms in the destruction of the homonuclear recoupling under certain conditions of CW decoupling while decoupling is applied in *S*-spin channel. These calculations were implemented in Mathematica 5.2 [81] running under Red Hat Linux 2.4.

The number of heteronuclear dipolar allowed-terms for each combination of symmetry number (N, n, ν_I, ν_S) at $\omega_r/2\pi$=6 kHz has been calculated and is plotted in Fig. 7.9.a). This plot has been produced in the same way as the contour plots shown in Fig. 7.8.a). Along the vertical axis, the condition $n = 2$ is kept fixed, while N and ν_S are varied simultaneously, according to the value $\nu_S = \frac{1}{2}N-1$. The horizontal axis shows the values of ν_I used in these calculations. The top horizontal axis and the right-hand vertical axis have been labelled according to the *I*-spin and *S*-spin nutation frequencies corresponding to the plotted values of ν_I and N, respectively, at the spinning frequency of $\omega_r/2\pi$=6 kHz.

Although there is a certain resemblance between the calculations shown in Fig. 7.9.a) and the simulations shown in Fig. 7.8.a., there are many differences that make it unsuitable to explain theoretically the experimental observations, considering only the number of heteronuclear dipolar allowed-terms. A more precise image of the problem is given if the heteronuclear interference factors are considered. The heteronuclear interference factor for each combination of (N, n, ν_I, ν_S) has been plotted in a contour plot in Fig. 7.9, following the same procedure as for Fig. 7.9.a), under the same conditions. Comparison of this plot with Fig. 7.8.a) shows a strong resemblance. Regions of high DQ filtering efficiency in Fig. 7.8.a) correspond to regions with low values of $\Re$ in Fig. 7.9.b), while regions of poor DQ filtering efficiency in Fig. 7.8.a) correspond to regions with high values of $\Re$ in Fig. 7.9.b). In this plot, both regimes of good DQF efficiencies appear quite clearly and display low values of $\Re$. Also, the broad diagonal region of very poor values of DQF efficiencies corresponds to a similar region of high values of $\Re$.

This first-order theoretical analysis explains quite well many of the experiments and simulations. However there are some discrepancies. The analysis predicts a large change in the heteronuclear interference when the *I*-spin nutation frequency is slightly changed. In general, the simulations agree with this prediction but this is not observed in some regions; for instance, in the diagonal broad region of very low efficiency the sensitivity to these changes in *I*-spin nutation frequency is small in the simulation. Also, this first-order analysis is not able to explain the behaviour observed in glycine due to the ^{1}H-^{1}H interaction. All these discrepancies can be attributed to second-order effects. Additionally, in the experi-

mental plots, the DQF efficiency could be broadened by effects such as rf inhomogeneity or phase imperfections.

7.3. Heteronuclear decoupling interference during recoupling with CN_n^ν sequences

7.3.1. Pulse Sequence Scheme

In this section, the effect of the CW heteronuclear ^{1}H decoupling on the performance of a group of sequences of symmetry CN_n^ν is presented. This CN_n^ν sequences belong to the series of sequences CN_2^1, where $7 \leq N \leq 20$. $C7_2^1$ is a successful sequence of this series that has been used as for dipolar DQ recoupling sequence [66], [67], [40] and has become almost a standard technique in solid-state NMR [87].

These sequences (Fig. 7.10) consist of N repetitions over two rotor periods of the basic element called a POST-element that describes a 2π rotation along x-axis in the rotating frame:

$$C_0 = 90_0 360_{180} 270_0 \tag{7.9}$$

The phases of consecutive elements are incremented by an angle equal to $\phi = 2\pi/N$. The nutation frequency is set so that one CN_2^1 occupies two rotor periods. In this case, the nutation frequency is exactly given by:

$$\omega_{nut}^{^{13}C} = N\,\omega_r \tag{7.10}$$

where ω_r is the spinning frequency.

The first-order average Hamiltonian has symmetry-allowed terms of the form $\{l, m, \lambda, \mu\} = \{2, -1, 2, -2\}$, $\{l, m, \lambda, \mu\} = \{2, 1, 2, 2\}$ (homonuclear dipolar double-quantum terms), $\{l, m, \lambda, \mu\} = \{0, 0, 1, 0\}$ (isotropic chemical shift) and $\{l, m, \lambda, \mu\} = \{0, 0, 0, 0\}$ (homonuclear J-coupling terms). Scaling factors for each allowed term are indicated in Table 7.3.

Table 7.3. Symmetry-allowed first-order Hamiltonian terms and scaling factors of the series of sequences CN_2^1.

Symmetry-allowed first order terms	DD $\{2, -1\}, \{2, -2\}$	DD $\{2, 1\}, \{2, 2\}$	isoCS $\{0, 0\}, \{1, 0\}$	J-couplings $\{0, 0\}, \{0, 0\}$
Scaling factors	0.15 - 0.17	0.15 - 0.17	0	1

Table 7.4. Number of second-order allowed terms for the sequence $C7_2^1$.

Symmetry-allowed second order terms	DD	CSA	isoCS	rf	J
DD	68	54	24	4	0
CSA	54	20	8	0	12
isoCS	24	8	6	4	3
rf	4	0	4	2	2
J	0	12	3	2	0

The number of second-order symmetry-allowed terms for the sequences CN_2^1 is higher than that for $RN_2^{(-1+N/2)}$. This is an inconvenient property that makes more attractive the use of the $RN_2^{(-1+N/2)}$ family of sequences for dipolar recoupling (see Table 7.4). However, the $RN_2^{(-1+N/2)}$ sequences are more difficult to implement, and the CN_2^1 series of sequences presents a more robust behaviour with respect to rf imperfections and phase transients [70], [29].

These sequences are incorporated into double-quantum filtered (DQF) experiments following the same procedure as for the series of $RN_n^{-1+N/2}$ sequences (see Fig. 7.10).

The recoupling efficiency is studied as a function of the following parameters: the magic-angle-spinning frequency $\omega_r/2\pi$, the ^{1}H decoupling nutation frequency $\omega_{nut}^{^1H}$ during the

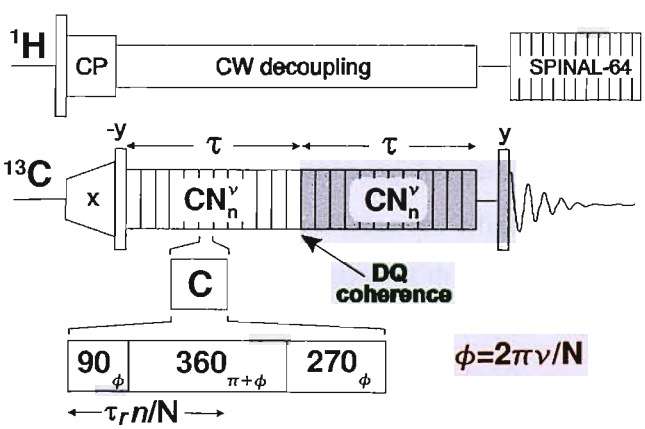

Fig. 7.10. Pulse sequence diagram for ^{13}C double-quantum homonuclear dipolar recoupling with a symmetry-based CN_n^ν recoupling sequence.

homonuclear recoupling sequence, the ^{13}C recoupling nutation frequency $\omega_{nut}^{^{13}C}$, and the symmetry number N of the CN_2^1 recoupling sequence. The symmetry numbers n and ν are held fixed at n=2. The synchronization requirements of the CN_2^1 sequences requires the relationship $\omega_{nut}^{^{13}C}=2N\omega_r/n$ for the basic element. There are therefore three independent parameters to consider.

7.3.2. Experimental

The DQ efficiencies were estimated according to the procedure described for $RN_n^{-1+N/2}$ sequences in section 7.2.2. The experimental parameters ϕ can be seen in Appendix B.

MAS frequencies of 6 and 12 kHz and a series of CN_2^1 sequences with N = 7, 8, 9, 10, ..., 20 were studied. All experiments were performed in a field of 9.4 T using 3.2 mm zirconia rotors on a Varian *InfinityPlus* console. The ^1H nutation frequency during the SPINAL-64 decoupling sequence applied during signal acquisition was fixed at 100 kHz.

Experiments were performed on the model organic compound described in chapter 6: diammonium-[2,3-$^{13}C_2$]fumarate 10% diluted in natural abundance diammonium fumarate (DAF).

7.3.3. Results

The results obtained in these experiments confirm the no ^1H decoupling regime observed for $RN_n^{-1+N/2}$ sequences, extending this result to the whole series of CN_2^1 sequences. The same two-dimensional contour plots of Fig. 7.4 were constructed for experiments at MAS frequencies of 6 and 12 kHz for CN_2^1 sequences (Fig. 7.11). However, the behaviour of these sequences with respect the ^1H decoupling presents some differences with respect to the $RN_n^{-1+N/2}$ sequences. Experiments at 6 kHz spinning frequency (Fig. 7.11) show the existence of the regime of low ^1H decoupling irradiation for efficient DQ homonuclear dipolar recoupling while the efficiencies in a second regime with high ^1H decoupling irradiation are quite low (10-30%) and the area occupied by this regime in the contour plot is highly reduced compared with the same regime for the series $RN_n^{-1+N/2}$. Additionally, the restricted areas due to high rf power (black regions) are higher due to the nutation frequency relationships of these sequences. A maximum of 40% recoupling efficiency was obtained with the sequence $C15_2^1$ and no ^1H decoupling while the maximum efficiency obtained with $C7_2^1$ and

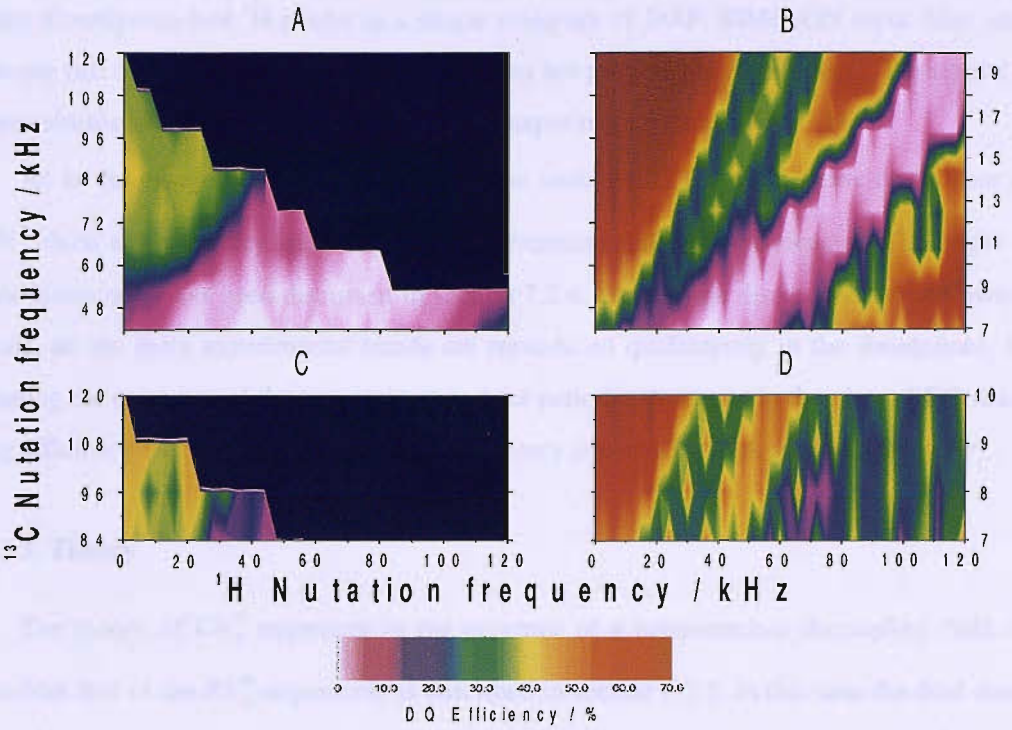

Fig. 7.11. Contour plots of the experimental (left) and simulated (right) ^{13}C double-quantum filtering efficiency at a spinning frequency of (A and B) 6 kHz and (C and D) 12 kHz for DAF using the family of sequences CN_2^1 with N bigger or equal to 7. The ^{1}H decoupling nutation frequency is plotted along the horizontal axis while the ^{13}C recoupling nutation frequency is plotted along the vertical axis. The corresponding symmetry number N is indicated on the right-hand vertical axis. The black regions are inaccessible, due to technical limitations on the probe performance.

120 kHz ^{1}H decoupling nutation frequency was 28%.

For $\omega_r/2\pi$= 12 kHz (Fig. 7.11.C), the behaviour of the ^{13}C DQ filtering efficiency with respect to the ^{1}H decoupling interference follows the same trend as the one at 6 kHz spinning frequency. However, due to the higher rf field at this spinning frequency in the ^{13}C channel only few sequences are available. A DQ filtering efficiency of 45% was achieved at $\omega_r/2\pi$=12 kHz using the sequence $C10_2^1$ without ^{1}H decoupling.

These results show that in order to perform DQF experiments using CN_2^1, sequences, the regime without decoupling is almost compulsory in order to get high DQF efficiency at almost any spinning frequency.

7.3.4. Numerical Simulations

Simulations of the effects of ^{1}H decoupling on ^{13}C homonuclear recoupling were per-

formed using the SIMPSON platform [90]. The simulations considered the ^{13}C nuclei and their directly-attached ^{1}H nuclei in a single molecule of DAF. SIMPSON input files, containing full details of the simulated spin systems are provided in Appendix C. The results of these simulations are shown together with the experimental data in Fig. 7.11.

As in the case of $RN_n^{-1+N/2}$ sequences, the simulated DQF efficiencies in the case of CN_2^1 show a discrepancy with respect to the experimental DQF efficiencies. The origin of this discrepancy has been discussed in section 7.2.4. Despite the discrepancy in the overall scale, all the main experimental trends are reproduced qualitatively in the simulations, including the existence of the two regimes and the periodic structures in the plots of DQ filtering efficiency vs. ^{1}H decoupling nutation frequency observed at high spinning frequency.

7.3.5. Theory

The theory of CN_n^{ν} sequences in the presence of a heteronuclear decoupling field resembles that of the RN_n^{ν} sequences, as described in section 6.2.5. In this case the dual channel sequence is denoted $CN_n^{\nu_I,\nu_S}$, where $\nu_I = \omega_{nut}^I n/\omega_r$. In this case the selection rule is given by Eq.5.32.

The heteronuclear interference factor can be calculated as:

$$\Re = \Re(N, n, \nu_I, \nu_S) = \left[\sum_{m,\mu_I,\mu_S} |\kappa_{2,m,1,\mu_I,\mu_S}(CN_n^{\nu_I,\nu_S})|^2 \right]^{1/2} \tag{7.11}$$

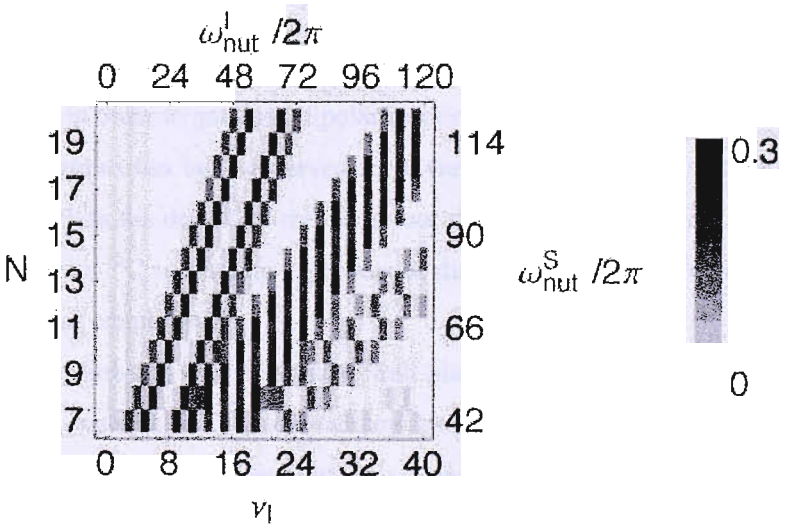

Fig. 7.12. a) Contour plot of the heteronuclear interference factor $\Re$ of symmetry-allowed terms plotted as a function of the symmetry numbers ν_I and N, for the sets of sequences $CN_n^{\nu_I,\nu_S}$, with $n = 2$ and $\nu_S = 1$, at a spinning frequency of 6kHz.

For the set of sequences CN_2^1 with the basic element $C^0 = 90_0360_{180}270_0$, a contour plot of $\Re$ against the symmetry numbers N and ν_1 is given in Fig. 7.12.

As in the case of the $RN_n^{-1+N/2}$ sequences, this first-order theoretical analysis explains quite well many of the experiments and simulation features for the CN_2^1 sequences. Similar discrepancies can be observed in the case of the CN_n^ν sequences as in the RN_n^ν case. These discrepancies may have a second-order interference origin, in the same way as for the $RN_n^{-1+N/2}$ sequences.

7.4. Conclusions

The main conclusion of these studies is the existence of an experimental regime of weak or absent *I*-spin decoupling irradiation during *S*-spin dipolar recoupling in which the heteronuclear interference is minimized, leading to high DQF efficiencies. This regime allows good recoupling performances at moderate to high spinning frequencies. However it is not restricted to low spinning frequencies if the nutation frequency on the *S*-channel is high enough. Therefore, this regime is a good match for most of the solid-state NMR experiments involving DQ dipolar recoupling, where high recoupling efficiencies and high resolution are very important. The second regime of good dipolar recoupling efficiency is the traditional regime in which the *I*-spins have a strong rf field while the *S*-spin rf field is moderated. This regime is available at low spinning frequencies up to 10 kHz for RN_n^ν sequences and under 6 kHz for CN_n^ν sequences. Therefore, in the case of CN_n^ν, the first regime is almost compulsory in order to get good dipolar recoupling efficiencies.

These two regimes has been observed for a variety of structural groups in a variety of samples. Nonetheless the details of the behaviour depends on the sample. The CH_2 groups are quite difficult for ^{13}C recoupling experiments, due to the strong ^1H-^{13}C heteronuclear and ^1H-^1H homonuclear couplings.

The first-order analysis describes quite well almost all the simulated and experimental observations. An explanation of the remaining discrepancies will require the consideration of second-order effects, simulations with larger numbers of spins and the inclusion of effects such as rf inhomogeneity

Additionally, these studies allow a comparison of the performance of $RN_n^{-1+N/2}$ and CN_2^1 homonuclear dipolar recoupling sequences. In terms of DQF efficiencies, both sequences

present same results without decoupling. However, the strong restriction in rf field that can be applied for the CN_2^1 sequences makes these sequences more favourable for homonuclear dipolar recoupling without *I*-spin decoupling at low to moderate spinning frequencies. For moderate to high spinning frequencies $RN_n^{-1+N/2}$ sequences are the only ones available in the absence of decoupling [33], [75].

8. Truncated Dipolar Recoupling

8.1. Introduction

Solid-state NMR is a useful tool to get structural information, especially in materials such as polymers, biomolecules and network solids. Dipolar recoupling is the most important methodology for extracting internuclear distances with high accuracy in the presence of MAS. The case of isolated pairs leads to particularly simple spin dynamics which has been extensively characterized, so distance determination in this systems is relatively simple. It is possible to engineer the necessary spin-pair distribution by isotopic labelling, but this is expensive and laborious.

The use of multiply-labelled samples would be more general and cost-effective, but due to the complicated spin dynamics of these systems it is more difficult to interpret the data [111]. Typically, the dynamics of multiple-spin systems are dominated by short-range couplings with a small influence from long-range couplings [112]. This property is unfavourable for structural studies since long-range couplings usually have more structural importance than short couplings.

Several experiments permit the estimation of individual long-range couplings in the presence of short-range couplings, but all of them have strong limitations. REDOR experiments [113] and RR experiments [112], [114], [115], [116] have been used to estimate long-range couplings in multiple-spin systems: REDOR is restricted to heteronuclear systems while RR experiments are restricted to certain ranges of CS differences.

This chapter describes a new recoupling concept in multiple-spin systems called *truncated dipolar recoupling (TDR)*. This new concept allows the selective determination of internuclear distances in a wide variety of homonuclear multiple-spin systems.

The work presented in this chapter has been done in collaboration with of G. Mollica, A. Gansmüller, M. Carravetta, G. Pileio, A. Bechmann, A. Sebald and M. H. Levitt.

8.2. Theory

The spin Hamiltonian in a homonuclear system of coupled spins-1/2 is given by:

$$\hat{\mathcal{H}} = \sum_j \hat{\mathcal{H}}_j + \sum_{j<k} \hat{\mathcal{H}}_{jk} \tag{8.1}$$

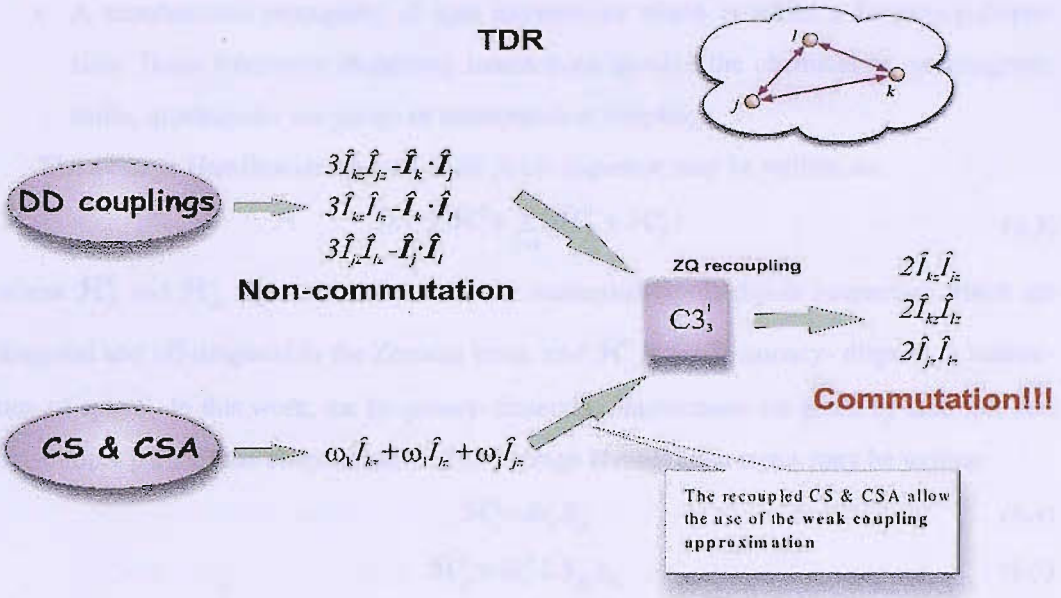

Fig. 8.1. Truncated Dipolar Theory Scheme.

where $\mathcal{H}_j$ is the individual spin-field interaction and $\mathcal{H}_{jk}$ represents the spin-spin interactions. The Hamiltonians of spin pairs in a multiple-spin system do not commute:

$$[\hat{\mathcal{H}}_{jk}, \hat{\mathcal{H}}_{kl}] \neq 0 \tag{8.2}$$

This non-commutativity makes it difficult to separate the effects of different spin-spin couplings. In this case, the stronger couplings dominate the spin dynamics of the system which makes it difficult to disentangle the weaker couplings, which are very important in structure determination.

In solution NMR, the spin Hamiltonian in Eq.(8.1) may be simplified by ignoring the off-diagonal terms in the Zeeman basis [6]. This simplification is possible if the Larmor frequency differences between all coupled spins greatly exceed the off-diagonal parts of the relevant coupling Hamiltonians (*weak coupling approximation*). The truncated coupling terms commute with each other and with the spin-field terms. This property is the basis of most solution NMR methodology.

The weak coupling condition also applies in solid-state NMR [117], [118]. However, in general, the recoupled dipole-dipole interactions created by applying a recoupling pulse sequences do not commute, leading to strong coupling in the case of more than two coupled spins.

It is possible to introduce the weak coupling approximation using truncated dipolar recoupling (TDR). This concept involves two essential features:

- zero-quantum recoupling of homonuclear dipole-dipole interactions [119].
- A simultaneous recoupling of spin interactions which provides a frequency-dispersion. These frequency dispersing interactions involve the chemical or paramagnetic shifts, quadrupolar couplings or heteronuclear couplings.

The average Hamiltonian under a TDR pulse sequence may be written as:

$$\bar{\mathcal{H}} \simeq \sum_j \bar{\mathcal{H}}_j^0 + \sum_{j<k} (\bar{\mathcal{H}}_{jk}^0 + \bar{\mathcal{H}}_{jk}^{\pm}) \tag{8.3}$$

where $\bar{\mathcal{H}}_{jk}^0$ and $\bar{\mathcal{H}}_{jk}^{\pm}$ represent the parts of the recoupled dipole-dipole interaction which are diagonal and off-diagonal in the Zeeman basis, and $\bar{\mathcal{H}}_j^0$ is the frequency- dispersing interaction of spin S_j. In this work, the frequency-dispersing interactions are given by isotropic and anisotropic parts of the chemical shift. The average Hamiltonian terms may be written:

$$\bar{\mathcal{H}}_j^0 = \bar{\omega}_0^j S_{jz} \tag{8.4}$$

$$\bar{\mathcal{H}}_{jk}^0 = \bar{\omega}_0^{jk} 2 S_{jz} S_{kz} \tag{8.5}$$

$$\bar{\mathcal{H}}_{jk}^{\pm} = \bar{\omega}_{jk}^{\pm} \frac{1}{2} (S_j^+ S_k^- + S_k^- S_k^+) \tag{8.6}$$

with:

$$\bar{\omega}_0^{jk} = \bar{\omega}_{jk}^{DD} + \pi J_{jk} \tag{8.7}$$

$$\bar{\omega}_{jk}^{\pm} = -\bar{\omega}_{jk}^{DD} + 2\pi J_{jk} \tag{8.8}$$

If the weak coupling approximation is satisfied for all spin pairs:

$$\bar{\omega}_0^j - \bar{\omega}_0^k \gg \bar{\omega}_{jk}^{\pm} \tag{8.9}$$

then the coupling terms may be truncated leading to a weakly-coupled spin system (Fig. 8.1). In this case couplings may be treated independently and the measurement of individual couplings in multiple spin systems may be implemented.

Two different implementation of the TDR theory are discussed in the present chapter:

1. Variable-time implementation
2. Constant-time implementation

8.3. Variable-Time Implementation

8.3.1. Pulse Sequence Scheme

The TDR concept has been implemented according to Fig. 8.2. This pulse sequence scheme is rather complex due to multiple factors that can affect the truncation of the dipolar couplings.

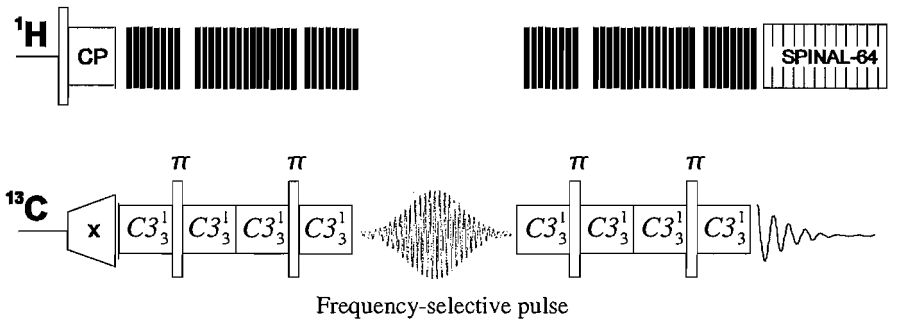

Fig. 8.2. TDR pulse sequence scheme implemented in a variable-time mode.

The pulse sequence is composed of three main parts on the ^{13}C channel:

- The zero-quantum recoupling sequence $C3_3^1$, which recouples the dipole-dipole coupling terms and chemical shift terms.
- A frequency-selective π-pulse for the selective inversion of the individual truncated couplings.
- A series of π-pulses between two $C3_3^1$ sequences to improve the ^1H decoupling.

The ^1H channel contains:

- A decoupling sequence which is synchronized with the $C3_3^1$ sequence on the ^{13}C channel.

Zero-quantum recoupling: The sequence $C3_3^1$.

The sequence $C3_3^1$ has the following form (see Fig. 8.3):

$$C3_3^1 = C_0 C_{2\pi/3} C_{4\pi/3} \tag{8.10}$$

where the basic element C_ϕ (double windowed POSTC-element [67]) is given by :

$$C_\phi = [\tau_r/4] - \underbrace{(90)_{0+\phi}\,(360)_{\pi+\phi}\,(270)_{0+\phi}\,(90)_{\pi+\phi}\,(360)_{0+\phi}\,(270)_{\pi+\phi}}_{\tau_r/2} - [\tau_r/4] \tag{8.11}$$

In this basic element τ_r is the rotor period, and ϕ is an overall phase which takes the values 0, $2\pi/3$ and $4\pi/3$ for each element of the $C3_3^1$ sequence. This sequence has a duration of three rotor periods and requires an rf field providing a nutation frequency of:

$$\omega_{nut} = |8\omega_r| \tag{8.12}$$

where ω_r is the spinning frequency.

The symmetry-allowed terms of the first-order average Hamiltonian and their scaling

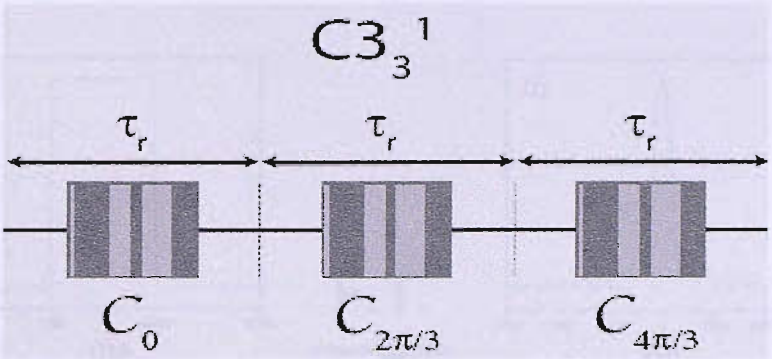

Fig. 8.3. Schematic representation of the sequence $C3_3^1$ using windowed double POSTC-element.

factors are given in Table 8.1.

The scaling factor for the isotropic chemical shift in the windowless double POSTC-element vanishes. However, the introduction of windows allows the evolution of CS during this short period and, therefore the scaling factor is increased up to a value of 0.5.

Frequency-selective pulse: the Gaussian pulse.

Regular high-power rf square pulses excite a broad region of the NMR spectrum. The excitation bandwidth of a pulse in the frequency domain can be evaluated by performing the Fourier transform of the time domain excitation function of a pulse, if a linear response approximation is assumed. The resulting excitation bandwidth is t_p^{-1}, where t_p is a width of the square pulse. In order to selectively excite a narrow region of the spectrum, the width of the square pulse has to be lengthened.

Table 8.1. Symmetry-allowed first order Hamiltonian terms and scaling factors of the $C3_3^1$sequence with the windowed double POSTC-element.

Symmetry-allowed first order terms	DD {2, 1},{2, 0}	DD {2,-1}, {2, 0}	DD {2, 2}, {2, 0}	DD {2,-2}, {2, 0}	J-couplings {0, 0}, {0, 0}
Scaling factors	0.14	0.14	0	0	1
Symmetry-allowed first order terms	CSA {2, 1},{1, 0}	CSA {2,-1}, {1, 0}	CSA {2, 2}, {1, 0}	CSA {2,-2}, {1, 0}	isoCS {0, 0}, {1, 0}
Scaling factors	0.19	0.19	0	0	0.5

This approach has an important drawback. The excitation profile of a long square pulse presents wiggles that can excite undesirable regions in the spectrum. This problem can be

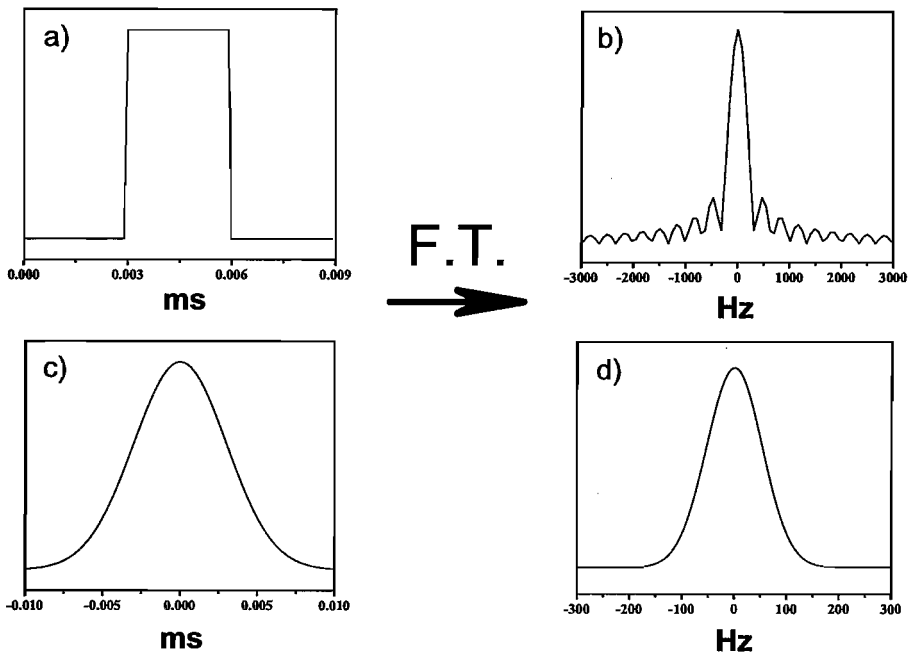

Fig. 8.4. a) Time profile of a rectangular pulse of a duration of 3 ms. b) Excitation frequency profile of the square pulse in a) obtained by the power spectrum of the Fourier Transform of the time domain profile. c) Time profile of a gaussian pulse of 3 ms. d) Excitation profile in the frequency domain for the gaussian pulse in c) obtained by the power spectrum of the Fourier Transform of the time domain profile.

solved by using with a shaped-amplitude pulse. Fig. 8.4 shows that the excitation profile for a pulse with Gaussian shape on the amplitude does not present lobes on either side of the principal excitation band. It is clear that this approach has to be employed if an accurate pulse shape is required [30], [120].

The experimental procedure, which will be described in detail in section 8.3.3, requires the selective excitation of either one or two sets of spins in two different experiments. The selective excitation of one set of spins can be done with a rf pulse if a normal Gaussian amplitude modulation is used. However, the selective excitation of two sets of spins needs two Gaussian pulses in the frequency domain. If the inverse Fourier Transform is performed on the frequency-domain function, the resultant function is a cosine-modulated Gaussian in the time domain. Therefore, in order to excite two set of spins a cosine-modulated Gaussian shape (Eq.(8.13)) was used for the rf pulse amplitude.

$$A = A_{\cos}\,\omega_{nut}\exp\left(-\pi\sigma^2 t^2\right) \tag{8.13}$$

where σ is half of the width of the Gaussian pulse and $A_{\cos}$ is the cosine modulation of the

Gaussian pulse, which is given by:

$$A_{\cos}=\cos(2\pi\omega_{mod}t) \tag{8.14}$$

where ω_{mod} is half of the difference in isotropic chemical shift between the selected spins.

The cosine modulation frequency is proportional to half of the difference in isotropic chemical shift frequencies between the two. This cosine-modulated Gaussian pulse can be used to excite one spin if the cosine-modulation frequency is set to zero.

In the scheme described in Fig. 8.2, the Gaussian pulse has a duration equal to an integer number of rotor periods.

Additionally, the selective pulse is used to refocus the chemical shift interactions. The cosine-modulated Gaussian π-pulse is located between the excitation and reconversion sequences in order to act as the π-pulse of a echo sequence that refocusses the chemical shift. Since the recoupled chemical shift terms are removed by this procedure, their precise form and orientation-dependence is unimportant. They should simply be large enough to truncate the recoupled dipolar interactions.

Proton decoupling.

The $C3_3^1$ sequence also recouples heteronuclear dipolar terms which may interfere with the homonuclear dipolar recoupling. In order to avoid this problem, a combination of continuous irradiation in the ^{1}H channel plus π-pulses in the ^{13}C channel is used. The continuous irradiation is synchronized with the ^{13}C irradiation and the rotation of the sample in order to have a 2πrotation of the ^{1}H spins. This renders the same spin state at the beginning

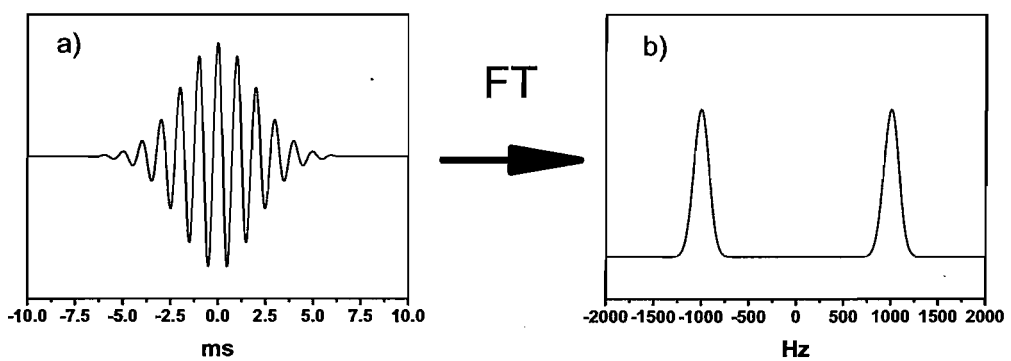

Fig. 8.5. a) Time profile of a cosine-modulated Gaussian pulse of 10 ms. b) Excitation profile of the Gaussian pulse shown in a) obtained by Fourier Transform of the time domain profile.

and at the end of the window. Two π-pulses are located inside the C blocks with the same number of these blocks on each side of the π-pulses, in order to refocus the heteronuclear interactions.

8.3.2. Simulating the TDR sequence

In order to show the validity of the TDR concept, numerical simulations were performed using SIMPSON [90] on a 3-spin and 2-spins models using parameters appropriate for $^{13}C_3$-L-alanine [121], at a magnetic field of 9.39 T and a spinning frequency of $\omega_r / 2\pi$ = 11.000 kHz (Fig. 8.7). The powder average was calculated using 256 pairs of Euler angles (α,β), distributed according to the REPULSION scheme [122], with the third Euler angle (γ) stepped through a full revolution in 20 steps. The start and detect operator in both cases is the I_x spin operator. In each simulation, the number of C blocks in the excitation and reconversion parts have been arrayed from 0 to 180 in steps of 3 blocks in a symmetric way. The signal is acquired at the end of each step. The result is a curve that decays and oscillates at the frequency of the selected dipolar coupling. Therefore, the modulation of the curve depends on the size of the dipolar coupling. For instance, if the distance between two spins is large, the resulting curve will be modulated by a small frequency because the dipolar coupling will be quite small. On the other hand, if the distance between two spins is small, the resulting curve will be strongly modulated by the dipolar frequency because the dipolar

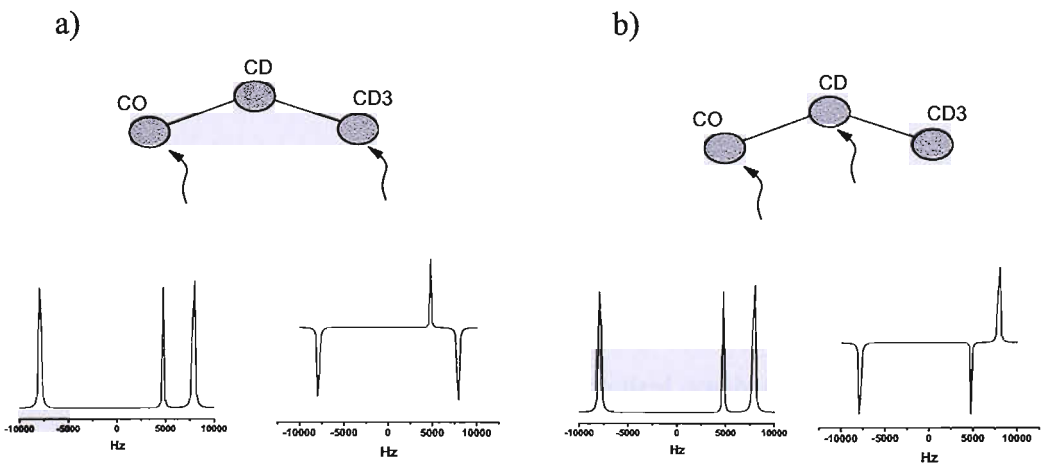

Fig. 8.6. Simulations showing the selective inversion of the pairs of spins by cosine-modulated Gaussian pulses. a) Selective inversion of the COCD3 pair of spins of alanine. b) Selective inversion of the COCD pair of spins alanine.

coupling will be bigger.

Fig. 8.7 shows two simulations of the variable-time implementation of the TDR sequence using selection of the spins by ideal doubly-selective π-pulses. The solid line shows the result of a simulation selecting ^{13}CO and $^{13}C\ ^{2}H_3$ and observing ^{13}CO. The dashed line represents a simulation in which the ideal double-selective π-pulses have been applied to ^{13}CO and $^{13}C\ ^{2}H$ and ^{13}CO is observed. The obtained curves have a different behaviour for long and short dipolar couplings (the distance between the ^{13}CO and $^{13}C^{2}H$ spins is 1.530 Å while the distance between the ^{13}CO and $^{13}C^{2}H_3$ is 2.517 Å). The short distance (dashed line) shows a faster decay and high frequency of oscillation but the long range (solid line) shows a slower decay and lower oscillation frequency. This is an indication that the dipolar couplings are truncated.

Fig. 8.7.b and Fig. 8.7.c show comparisons between 3-spin simulations (solid line) and

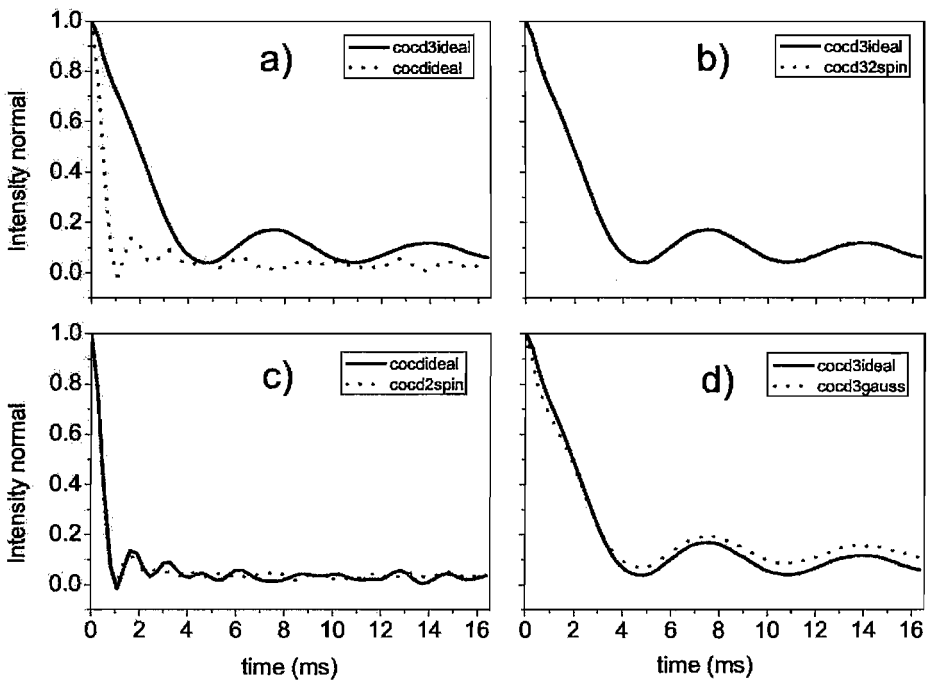

Fig. 8.7. a) Simulations of TDR experiments applying idealized doubly-selective pulses to ^{13}CO-$^{13}C\ ^{2}H$ (dashed line) and ^{13}CO-$^{13}C\ ^{2}H_3$ (solid line). The signal from the ^{13}CO is observed. b) Comparison between idealized simulation using 3-spin system (solid line) and 2-spin system (dashed line). In both simulations, idealized doubly-selective pulses have been used to select the ^{13}CO-$^{13}C\ ^{2}H_3$ spin-pair. The signal from the ^{13}CO is observed. c) Same as b) but for the ^{13}CO-$^{13}C\ ^{2}H$ spin-pair. d) Comparison between simulation using idealized doubly-selective pulse (solid line) and simulation using a realistic cosine modulated gaussian pulse (dashed line). The ^{13}CO-$^{13}C\ ^{2}H_3$ spin-pair has been selected in both simulations. The signal from the ^{13}CO is observed.

2-spin simulations (dashed line) for the cases described in Fig. 8.7a. The simulation in both cases are almost identical, showing some discrepancies at long times in which the effect of other interaction terms like J-couplings and higher order terms are relevant.

The last simulation Fig. 8.7.d shows a comparison between a simulation using a realistic cosine modulated gaussian pulse of a duration of 3 ms for the selective inversion and a simulation using the idealized selective pulse. ^{13}CO and $^{13}C\ ^{2}H_3$ are selected and ^{13}CO is observed in both cases. The offset of the Gaussian pulse was put between the ^{13}CO and $^{13}C\ ^{2}H_3$ peaks and the cosine modulation of the gaussian was equal to half of the difference in isotropic chemical shift between the ^{3}CO and $^{13}C\ ^{2}H_3$ peaks. The two simulations are almost identical. The small observed differences are probably due to imperfections in the performance of the selective Gaussian and *J*-coupling evolution during the long gaussian pulse.

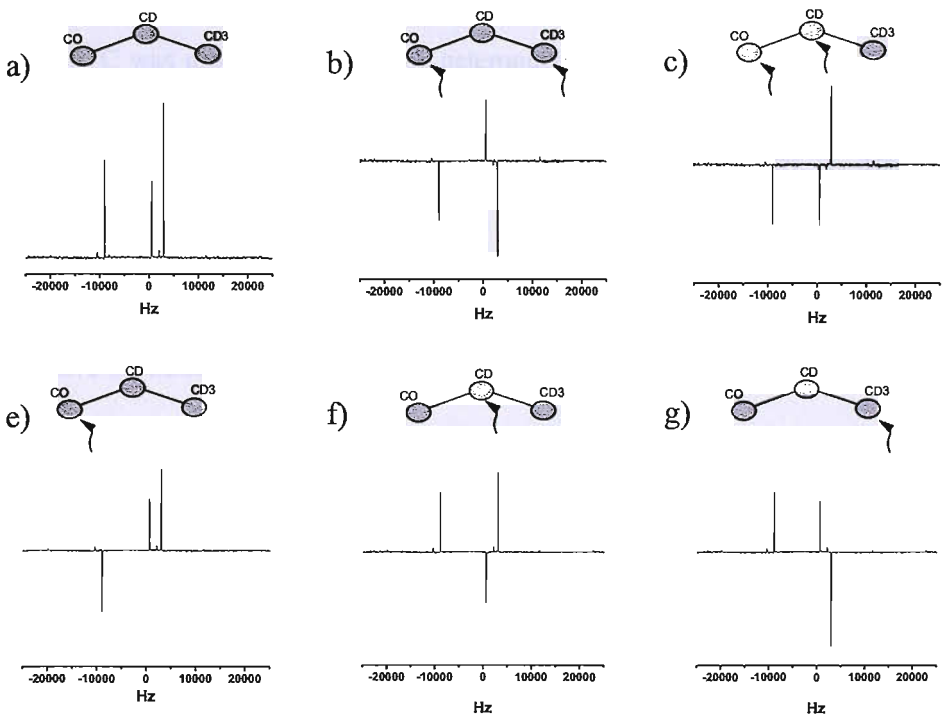

Fig. 8.8. This figure shows different selective inversions performed in the experiments described in section 8.3.3. These spectra show a very good performance of the gaussian pulses. a) The spectrum of [2,3-$^{2}H_4$, $^{13}C_3$, ^{15}N]-L-alanine without applying selective rotation. b) A doubly-selective cosine modulated gaussian is applied on CO and CD_3 sites. c) A doubly-selective cosine modulated gaussian is applied on CO and CD sites. c) A singly-selective cosine modulated gaussian is applied on CO site. d) A singly-selective cosine modulated gaussian is applied on CD site. d) A singly-selective cosine modulated gaussian is applied on CD_3 site.

All these simulations show the validity of the TDR concept for the estimation of selected internuclear couplings in strongly-coupled spin systems.

8.3.3. Experimental Results

Experiments in [2,3-$^{2}H_4$, $^{13}C_3$, ^{15}N]-L-alanine.

During previous experiments on fully protonated alanine, simulations and experiments were not in agreement due to fast decay on the experimental data. This strong damping in the curves is caused by the strong heteronuclear ^{1}H-^{13}C interactions. To avoid these kind of problems a deuterated sample of alanine or a sample without strong heteronuclear interactions, such as pyruvate, were used.

Experiments were performed on a 400 MHz Varian Spectrometer using a 3.2 mm probe. A spinning frequency of 11.000 kHz was used and a rf field of 88 kHz was applied in ^{13}C and ^{1}H channels during the recoupling *C* sequence and the ^{1}H decoupling scheme. A temperature of 70 ^{0}C was used to minimize the heteronuclear ^{1}H-^{13}C interactions with protons in the $^{15}NH_3$ group by increasing the rotational speed of this group. To a good approximation, if the rotation around the ^{13}C-^{15}N bond is sufficiently fast, the three ^{1}H-^{13}C heteronuclear couplings are averaged out to a small value.

CP was used to enhance the ^{13}C magnetization and SPINAL-64 decoupling [51] was applied during acquisition to decouple ^{1}H.

Selective excitation was done using a cosine-modulated Gaussian pulse with duration of

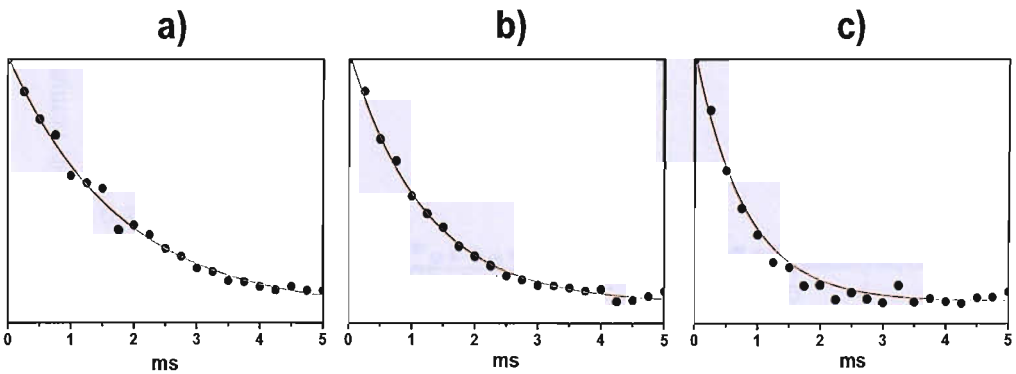

Fig. 8.9. a) Experimental single inversion of the CO spin. The decay has been fitted to an exponential decay. The time constant of the decay is τ_{dec}=1.79 ± 0.11 ms. b) Experimental single inversion of the CD spin. The decay has been fitted to an exponential decay. The time constant of the decay is τ_{dec}=1.22 ± 0.04 ms. c) Experimental single inversion of the CD_3 spin. The decay has been fitted to an exponential decay. The time constant of the decay is τ_{dec}=0.82 ± 0.03 ms. The decay rates have been used to correct the simulations for relaxation effects.

2.929 ms and $\sigma = 6.881\times 10^{6}$ s^{-2}. The offset frequency of this selective pulse was centered halfway between the isotropic chemical shifts of the selected ^{13}C spin pair. The frequency of the cosine modulation was equal to half of the difference in isotropic chemical shift frequencies between the selected ^{13}C spin pair. The difference in isotropic chemical shift frequencies for experimental data shown in Fig. 8.10 was 6437 Hz for the ^{13}CO-^{13}C ^{2}H pair and 7976 Hz for the ^{13}CO-^{13}C $^{2}H_3$ pair.

For each experiments, the number of C blocks in the excitation and reconversion parts was arrayed from 0 to 180 in steps of 3 blocks in a symmetric way. The obtained curves decay faster and oscillate less than the corresponding simulations. The fast damping in the experimental curves is related to the relaxation during the array of the C blocks.

In order to include this effect in the simulations, the relaxation decay was measured experimentally. This reference experiment was performed using the same procedure described above but with no cosine modulation of the Gaussian pulse and the offset frequency centered at the isotropic chemical shift of the selected ^{13}C spins. In this way only one set of spins is selected. Since the magnetization of the selected spins is only influenced by the relaxation, the signal decays exponentially without influence of the dipolar couplings. This reference experiment was done for each ^{13}C spin of alanine and their relaxation decay curves were extracted. Each curve was fitted by an exponential decay function and the relaxation times were extracted. The simulated curves were corrected by this exponential decay and

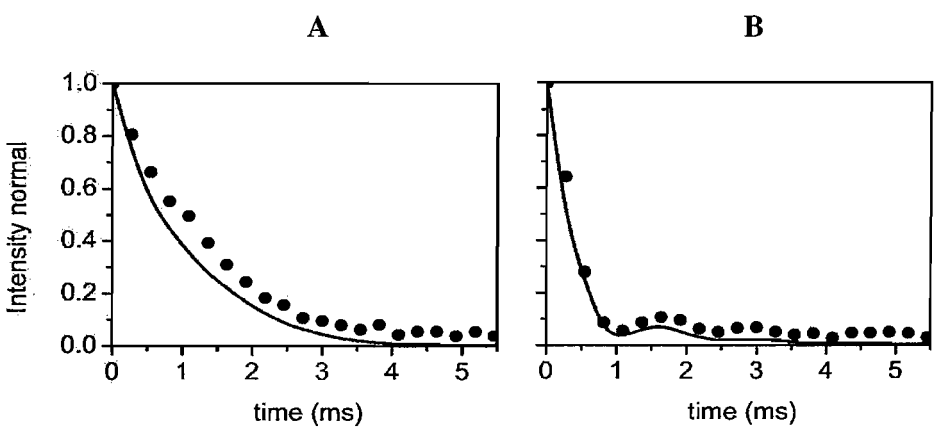

Fig. 8.10. Figure comparing simulations (solid line) and experimental results (dotted line). A). shows curve obtained when a cosine-modulated Gaussian pulse is applied to the ^{13}CO-^{13}C $^{2}H_3$ spin-pair (r_{jk} = 2.517 Å). The decay is quite slow and the oscillations are not present because of relaxation. B). The strong coupling within the ^{13}CO-^{13}C $^{2}H_3$ spin-pair (r_{jk} = 1.530 Å) produces a fast decay with a small oscillation which is damped by relaxation. In both cases the observed signal belongs to the ^{13}CO site.

compared with the experimental data.

Fig. 8.10 shows a comparison between the experiments and accurate simulations. The agreement between accurate simulations and experimental measurements is acceptable both for short- and long-range couplings. However, there are some discrepancies, especially at long excitation times, that can be due to ^{1}H relaxation effects and heteronuclear interactions, imperfect performance of the selective pulses and intermolecular interactions.

Experiments in U-[$^{13}C_3$]pyruvate.

The same experiments were performed on U-[$^{13}C_3$]pyruvate. The instrumental conditions were the same as for the [2,3-$^{2}H_4$, $^{13}C_3$, ^{15}N]-L-alanine case. The selective excitation was done using a cosine-modulated Gaussian pulse with duration of 2.929 ms. The frequency of the cosine modulation was equal to half of the difference in isotropic chemical shift frequencies between the selected ^{13}C spin pair. The difference in isotropic chemical shift frequencies for experimental data shown in Fig. 8.11 was 1857.6 Hz for ^{13}COO-^{13}CO pair and 7029.8 Hz for ^{13}COO-^{13}C $^{1}H_3$ pair.

Fig. 8.11 shows a comparison between experiments and accurate simulations. The relaxation decay was evaluated following the procedure described in the section 8.3.3 and all the simulations shown in Fig. 8.11 were corrected for the relaxation decay. Two types of simulations were performed. The first type of simulations does not take into account intermolecular dipolar couplings. These simulations are represented as a grey line in Fig. 8.11. It is clear that these simulations do not match the experimental curves. The second type of simulations take into account the intermolecular dipolar couplings. Considering the crystal structure of U-[^{13}C]-pyruvate shown in Fig. 6.4, in a non-diluted U-[^{13}C]-pyruvate sample, each ^{13}C nucleus has two other ^{13}C nuclei of the same kind at a distance of ~0.37 nm. In an isotopically diluted sample, on the other hand, the number of labelled neighbours is smaller and depends on the degree of isotopic dilution. The number of intermolecular dipolar couplings to consider in the simulations has been estimated from the degree of isotopic dilution in our sample. In our case there is a 25% of probability of having a ^{13}C nucleus close to another ^{13}C nucleus with a distance between them of ~0.37 nm. The intermolecular interactions contribute to in the decay curve in the singly-selective Gaussian pulse experiment, since one reason for this decay is the intermolecular dipolar interactions. The realistic simulation (solid line) including intermolecular dipolar coupling for our sample was obtained as follows:

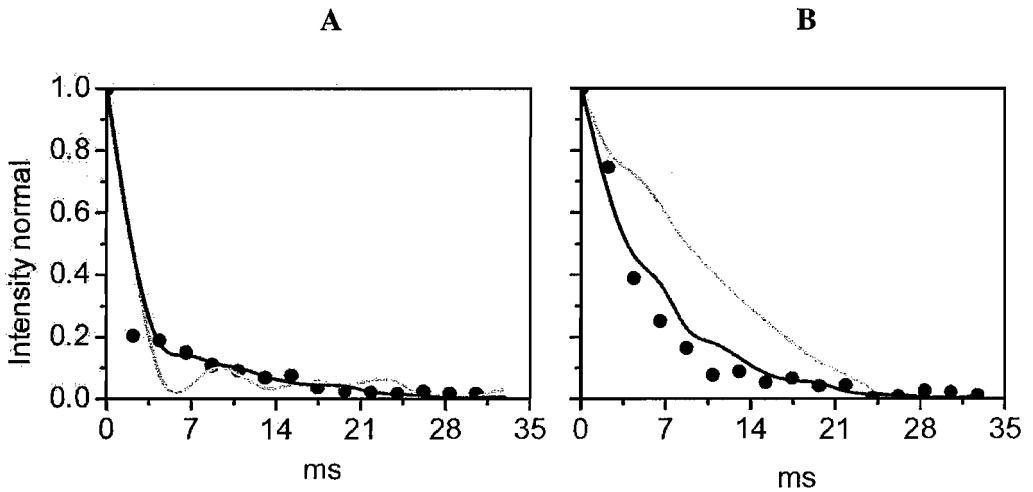

Fig. 8.11. A. Comparison between simulation taking into account the intramolecular interactions in the pyruvate system (solid black line), simulations without taking into account intermolecular interactions (solid grey line) and experimental results (filled circles). A). The selective Gaussian pulse has been applied to the ^{13}COO-^{13}COO spin-pair (r_{jk} = 0.156 nm). B). The selective Gaussian pulse has been applied to the ^{13}COO-$^{13}C\ ^{1}H_3$ spin-pair (r_{jk} = 0.260 nm).

$$S_{real}=0.75(S_{intra}\times SG_{decay})+0.25\,SG_{decay} \tag{8.15}$$

where SG_{decay} is the decay curve from the singly-selective Gaussian pulse experiment and S_{intra} is the three-spin simulation of the pyruvate system considering only intramolecular couplings.

Accurate simulations and experimental measurements are similar for both cases, short and long range couplings, although there is not a perfect match. These discrepancies are probably due to the complicated network of couplings in this sample. In our simulations many couplings have been ignored which may have an small effect. Also other issues such as ^{1}H relaxation effects, heteronuclear interactions and imperfect performance of the selective pulses could produce additional problems.

8.4. Constant-Time Implementation

8.4.1. Pulse Sequence Scheme

The constant-time scheme combines the zero-quantum recoupling sequence $C3_3^1$ with frequency selective pulses in a different way than in the variable-time scheme (Fig. 8.12). The approach described here involves a single radiofrequency channel. This scheme includes two shift-refocussed $C3_3^1$ sequences each of a duration of $\tau/2$, and two selective-Gaussian pulses with a π-pulse between them. Each selective Gaussian pulse rotates the res-

onant spins through an angle of $\pi/2$ while leaving off-resonant spins unperturbed. The two strong π-pulses in each TDR interval allow the removal of the chemical shift interactions.

The first Gaussian pulse has zero phase, while the second Gaussian pulse (drawn in black) has a phase ϕ_j which is varied between 0 and 2π. The intervals of $3\tau_r/4$ bracketing the selective pulses ensure that the starting point of the two $C3_3^1$ sequences are one-half of a rotor period out of phase with each other. Since the average dipole-dipole coupling Hamiltonian contains only $m=\pm1$ terms (see section 8.3.1), its sign is reversed by shifting the starting point t^0 of the $C3_3^1$ sequence by one half of a rotor period:

$$\overline{\omega}_{jk}^{DD}(t^0)=-\overline{\omega}_{jk}^{DD}(t^0+\tau_r/2) \tag{8.16}$$

If the J-couplings are ignored, the transverse magnetization created by the first $\pi/2$ rotation dephases under the recoupled spin-spin interactions over the first TDR interval $\tau/2$. However, since the TDR dipole-dipole Hamiltonian for the second sequence is opposite in sign to the first, all of these antiphase terms refocus by the end of the pulse sequence. The chemical shift anisotropy does not produce a net rotation over the free-evolution period because of the arrangement of $\tau_r/4$ and $3\tau_r/4$ intervals. The $\pi/2$ pulses after the second TDR interval converts the transverse magnetization into longitudinal magnetization. The last $\pi/2$ is phase-cycled to eliminate undesirable signals. This pulse converts the selected longitudinal magnetization back to longitudinal magnetization in order to be detected.

First, we are going to consider the case in which the phase (ϕ_j) of the second Gaussian is $\phi_j=\pi$. In this case, the rotations generated by the two Gaussian pulses cancel and the selective pulses can be ignored to a first approximation. The transverse magnetization generate by the first $\pi/2$ pulse evolves freely under the first quarter of a rotor period. After this interval the magnetization dephases under the first TDR interval. However, the second sequence is opposite in sign to the first due to the one-half of a rotor period of evolution between the two TDR blocks. All the terms generated by the first TDR interval are refocussed at the end of the second TDR interval. Therefore the NMR signal for the non-selected spins for the case of $\phi_j=\pi$ is not influences by the recoupled dipolar terms.

If the phase of the second Gaussian pulse is equal to zero, the selected spins S_j experience a π rotation which prevents the refocussing of the S_j-S_k dipole-dipole couplings. This π rotation of only one spin changes the sign of the TDR dipole-dipole Hamiltonian. Therefore, the rotation due to the one-half of rotor period is cancelled and the TDR dipole-dipole Hamiltonian for the second sequence is not opposite in sign to the first. The transverse magnetization of non-selected spins S_k is therefore reduced according to the strength of the

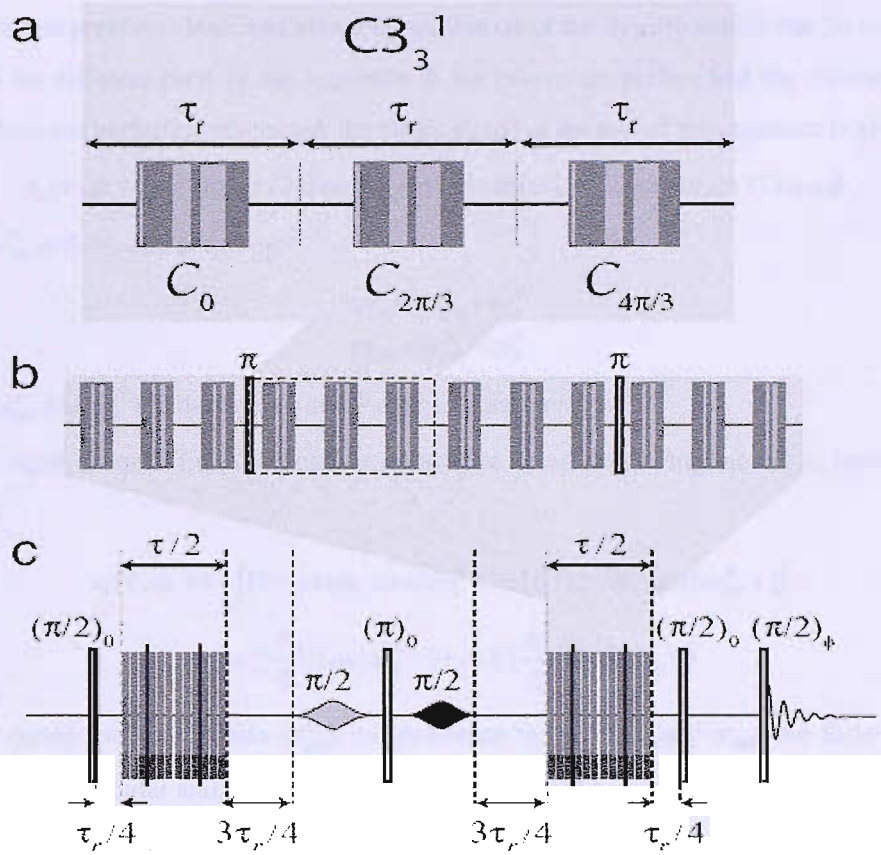

Fig. 8.12. (a) $C3_3^1$ pulse sequence, in which three radio-frequency cycles with overall phases {0, $2\pi/3$, $4\pi/3$} are applied in sequence. Each cycle has a duration of one rotor period. (b) Chemical shift refocussing is implemented by placing strong pulses at 1/4 and 3/4 of the total sequence duration. (c) The two TDR sequences bracket a combination of two weak rf pulses and one strong pulse, which has phase $\phi = 0$. The modulated weak pulses act as selective $\pi/2$ rotations on spins in site ϕ_j and have a duration equal to an integer number of rotor periods. The phase of the first selective $\pi/2$ pulse is zero, while the phase ϕj of the second selective pulse (shown in black) is varied from 0 to 2π in a series of experiments.

coupling $\overline{\omega}_{jk}^{DD}$ to the selected spins S_j, multiplied by the total recoupling interval τ.

The NMR signals from spins S_k which are not resonant with the Gaussian pulses increase as ϕ_j is increased from 0 to π, and then decreases again as ϕ_j is increased from π to 2π. The depth of this phase-dependence may be used to assess the magnitude of the corresponding coupling. The protocol operates in constant-time mode and hence is rather insensitive to relaxation interference [111], [123]. Many internuclear distances may be estimated in a single set of experiments.

8.4.2. Simulations and theoretical calculations

For the experiment described above the evolution of the density matrix can be evaluated through the different parts of the sequence. It the pulses are perfect and the chemical shift interactions are perfectly refocussed, the NMR signal at the end of the sequence is given by:

$$s_k(\tau,\phi_j)=\cos(\omega_{DJ}^{+}\tau/2)\cos(\omega_{DJ}^{-}\tau/2)+\sin(\omega_{DJ}^{+}\tau/2)\sin(\omega_{DJ}^{-}\tau/2)\cos\phi_j \quad (8.17)$$

where ω_{JD}^{+} and ω_{JD}^{-} are given by:

$$\begin{aligned}\omega_{JD}^{+}&=\omega_{DD}^{jk}+\omega_{J}^{jk}\\ \omega_{JD}^{-}&=\omega_{DD}^{jk}-\omega_{J}^{jk}\end{aligned} \quad (8.18)$$

where ω_{DD}^{jk} and ω_{J}^{jk} are the dipolar and J-coupling frequencies.

The signal form in Eq.(8.17) can be rearranged using simple trigonometric formulas as follows:

$$\begin{aligned}s_k(\tau,\phi_j)&=\frac{1}{2}[(1-\cos\phi_j)\cos(\omega_J^{jk}\tau)+(1+\cos\phi_j)\cos(\omega_{DD}^{jk}\tau)]\\ &=\sin^2(\frac{\phi_j}{2})\cos(\omega_J^{jk}\tau)+\cos^2(\frac{\phi_j}{2})\cos(\omega_{DD}^{jk}\tau)\end{aligned} \quad (8.19)$$

The signal contains (inside ω_{DD}^{jk}) a dependence on both $\beta_{MR}$and γ_{MR}, the Euler angles between the molecular and the rotor frame and thus should be averaged over all the possible orientations. The following integral should, therefore, be evaluated:

$$S_k(\tau,\phi_j)=\frac{1}{4\pi}\int_0^{2\pi} d\gamma \int_0^{pi} S_k(\tau,\phi_j)\sin\beta\, d\beta \quad (8.20)$$

The powder-average NMR signal of the observed spins S_k depends on the rf phase of the selective pulse $\phi_j$and the recoupling interval τ according to:

$$s_k(\tau,\phi_j)\simeq \sin^2(\frac{\phi_j}{2})\cos(\pi J_{jk}\tau)+\cos^2(\frac{\phi_j}{2})\frac{\pi\sqrt{2}}{4}J_{1/4}(\frac{\sqrt{6}}{4}k_{2120}b_{jk}\tau)J_{-1/4}(\frac{\sqrt{6}}{4}k_{2120}b_{jk}\tau) \quad (8.21)$$

where the scaling factor k_{2120} is equal to 0.140 for the case considered here. $J_{\pm 1/4}$ are quarter-integer-order Bessel functions [124]. b_{jk} is the dipole-dipole coupling constant which is proportional to the inverse cube of the internuclear distance.

To compare with theoretical curves, simulations were performed using SIMPSON [90] in a 3-spin model using parameters appropriate for U-[$^{13}C_3$]-L-alanine [121], at a magnetic field of 9.39 T and a spinning frequency of $\omega_r/2\pi$ = 11.000 kHz. The powder average was calculated using 256 pairs of Euler angles (α, β), distributed according to the REPULSION scheme [122], with the third Euler angle (γ) stepped through a full revolution in 20 steps.

Fig. 8.13 contains theoretical (solid black line) and simulated curves (dashed lines). It

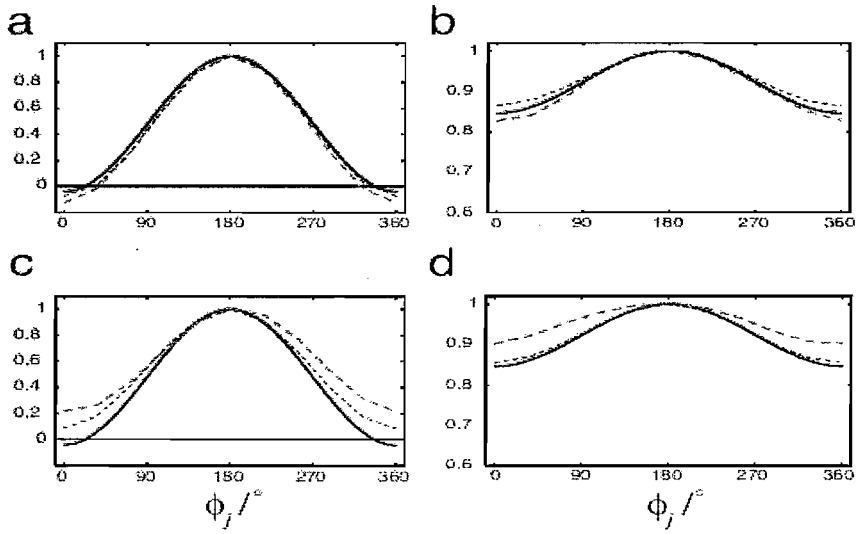

Fig. 8.13. Theoretical modulation curves using Eq.(8.21) (solid lines), and numerically simulated modulation curves using idealized selective pulses (thin dashed lines) or realistic selective pulses (dashed grey lines) for pairs of ^{13}C nuclei in $^{13}C_3$-L-alanine at a recoupling time of $\tau = 2.182$ ms and a spinning frequency $\omega_r / 2 = 11.000$ kHz. All curves are normalized to have a value of 1 at $\phi_j = \pi$. (a) The $^{13}CD_3$ site is observed with selective pulses applied to the ^{13}CD site ($r_{jk} = 0.152$ nm). (b) The $^{13}CD_3$ site is observed with selective pulses applied to the ^{13}CO site ($r_{jk} = 0.252$ nm); (c) The ^{13}CO site is observed with selective pulses applied to the ^{13}CD site ($r_{jk} = 0.153$ nm). (d) The site ^{13}CO is observed with selective pulses applied to the $^{13}CD_3$ site ($r_{jk} = 0.252$ nm).

can be observed that the depth of the modulation curves is deeper for the short internuclear distances (left column) than for the longer internuclear distances (right column).

Fig. 8.13 also shows SIMPSON simulations. Simulations using idealized selective rotations of zero duration on the selected spins are shown in dashed black lines while dashed grey lines show realistic simulations, in which the Gaussian pulse was simulated using a duration of 1.636 ms and an amplitude modulation function proportional to $\exp\{-at^2\}$ where $\sigma = 6.881 \times 10^6$ s^{-2}, as used in the experiments.

Simulations including idealized selective rotations (dashed black lines) agree quite well with theoretical calculations in both cases. This support the validity of the TDR concept. Realistic simulations (dashed grey lines) also agree well with the analytical formulae when the $^{13}CD_3$ site is observed while selective rotations are applied on the ^{13}CO or ^{13}CD sites (upper row). However, the agreement is less good when the ^{13}CO site is observed (lower row). This is due to the difficulty of achieving a clean discrimination between ^{13}CD and $^{13}CD_3$ sites by selective excitation.

8.4.3. Experimental Results

[$^2H_7$,$^{13}C_3$,^{15}N]-L-alanine was the test-sample used in our experiments. The sample was prepared by mixing [$^2H_4$,$^{13}C_3$,^{15}N]-L-alanine with 2,3-$^2H_7$,-L-alanine in a ratio 1:10 and re-crystallizing several times from ^2H_2O.

Experiments were performed on a 400 MHz spectrometer and a spinning frequency of 11.000 kHz. A 4 mm MAS rotor was used at room temperature. In all cases the recoupling interval was 2.182 ms. Each Gaussian pulse had a duration of 1.636 ms An interval of 120 seconds was left between transients, to allow recovery of the ^{13}C magnetization. To select individual spins the carrier was positioned in the centre of the spectrum, using a phase ramp to shift the selective rf field to the desired frequency.

Fig. 8.14 shows experimental signal amplitudes (dotted line) for the selection of $^{13}CD_3$ sites (top row) and selection of ^{13}CO sites (bottom row) compared with analytical formulae (solid lines) and accurate SIMPSON simulations (broken grey lines). The theoretical and analytical results have been adjusted to consider the natural abundance ^{13}C signals from un-

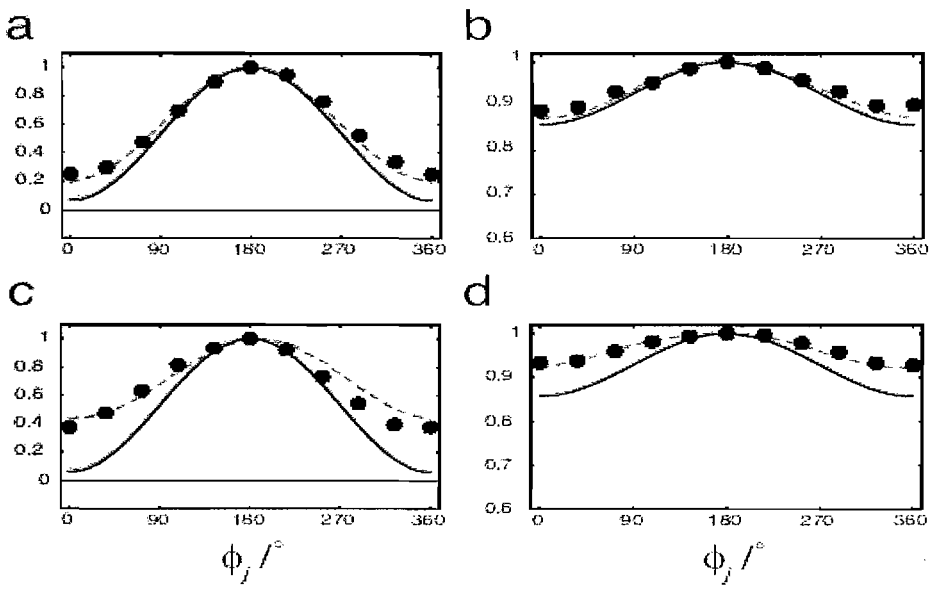

Fig. 8.14. Theoretical modulation curves using Eq.(8.21) (solid lines), numerically simulated modulation curves (dashed gray lines), and experimental measurements (filled circles) for a 1:10 solid solution of [2,3-$^2H_4$, $^{13}C_3$, ^{15}N]-L-alanine in 2,3-$^2H_4$-L-alanine. The theoretical and simulated curves have been adjusted to take into account the natural abundance ^{13}C signals from 2,3-$^2H_4$-L-alanine. All curves are normalized to have a value of 1 at $\phi_j = \pi$. (a) The ^{13}CD site is observed with selective pulses applied to the $^{13}CD_3$ site (r_{jk} = 0.152 nm). (b) The ^{13}CO site is observed with selective pulses applied to the $^{13}CD_3$ site (r_{jk} = 0.252 nm). (c) The ^{13}CD site is observed with selective pulses applied to the ^{13}CO site (r_{jk} = 0.153 nm). (d) The $^{13}CD_3$ site is observed with selective pulses applied to the ^{13}CO site (r_{jk} = 0.252 nm).

labelled L-alanine matrix, which comprises about 10% of each observed peak and which is not modulated by the phase of the second Gaussian.

The agreement between the experimental data and the simulations is good in both cases. However, some small differences can be observed in the case of strong dipolar coupling. These discrepancies have different contributions: a) imperfect performance of Gaussian pulses, b) heteronuclear ^{13}C-^{2}H interactions, c) ^{2}H relaxation effects and d) *J*-coupling evolution during the long Gaussian pulses. Imperfect performance of the Gaussian can lead to an imperfect refocussing of undesired interactions and an imperfect separation of the different dipolar couplings. The sequences $C3_3^1$ recouple the heteronuclear dipolar interactions but the heteronuclear ^{13}C-^{2}H dipolar interactions generally are quite small. However, higher order cross terms between heteronuclear and homonuclear dipolar interactions may be bigger. Therefore, experimental imperfections may induce small errors in the decoupling performance leading to imperfect ^{13}C-^{13}C homonuclear dipolar recoupling.

The agreement with the analytical curves is less good, especially when the ^{13}CO site is selected. These discrepancies can be attributed to imperfect performance of the selective pulses.

8.5. Discussion

Truncated dipolar recoupling is a promising new methodology for the estimation of selected internuclear distances in strongly-coupled multiple spin systems by solid-state NMR. However, these systems are highly complicated and several small issues remain unsolved.

The two different experimental implementations both produced good results for the case of $^{13}C_3$-alanine, showing the validity of the TDR concept. The variable-time approach is important to prove the validity of the TDR concept and the experimental applicability of it. The disadvantages of this approach are the relaxation dependence of the experiment which makes the analysis less reliable. On the other hand, the constant-time approach is more difficult to understand. However, this approach is more reliable and has the advantage of getting the experimental information for many dipolar couplings in one experiments.

Experiments and simulations agree reasonably well in both cases. The discrepancies observed are mainly related to imperfect performance of the Gaussian pulses, heteronuclear interactions and ^{2}H relaxation. Additionally, the application of the sequences described above to protonated samples is difficult due to the strong interference from heteronuclear interac-

tions. Therefore, more effective decoupling methods are required in this context.

In summary, TDR has considerable potential for selective spin-spin coupling measurements in multiple-spin systems in solid-state NMR. In principle, the idea is not restricted to nuclei with large chemical shift interactions. This idea should also be applicable to strongly-interacting abundant nuclei such as protons if other interactions such as paramagnetic shifts or heteronuclear dipole-dipole couplings provide the necessary frequency dispersion.

9. Conclusions

Two main goals have been discussed in this thesis:

i. The effects of heteronuclear interferences on double-quantum dipolar recoupling using CN_n^ν and RN_n^ν sequences and the possibility of using these sequences without decoupling.

ii. The development of methodology for the measurement of individual dipolar coupling in multiple spin systems.

The study of the effect of heteronuclear interactions was presented in chapter 7. Two experimental regimes were identified under which the heteronuclear interference with CN_n^ν and RN_n^ν recoupling sequences is minimized. One regime is the traditional one which involves a high rf irradiation on the ^{1}H channel while the ^{13}C rf field is medium or low. The second new regime uses no or low irradiation on the ^{1}H channel while the ^{13}C rf field is high. These regimes have been fully-characterized using experiments and simulations in three model compounds: diammonium [2,3-$^{13}C_2$]-fumarate, [^{15}N, $^{13}C_2$]-glycine, and [2,3-$^{13}C_2$]-L-alanine. We have shown that the observed effects can be predicted by first-order average Hamiltonian theory.

The second regime should be of interest to work with biological samples, reducing the risk of damage by strong ^{1}H decoupling. Additionally, this second regime extends the range of spinning frequencies for these sequences and improves the performance of the DQ excitation, reducing the effects of the heteronuclear couplings.

A new methodology for the estimation of individual internuclear distances in multiple spin systems, called truncated dipolar recoupling (TDR), is discussed in chapter 8. This new methodology uses a symmetry-based pulse sequence ($C3_3^1$) that recouples zero-quantum dipolar interactions as well as a frequency-dispersing interaction such as the chemical shift. Under these circumstances, the spin system behaves approximately as a weakly-coupled system if the difference between chemical shifts of the different spins are much bigger than the different dipolar couplings. The individual spin-spin couplings can be disentangled by using selective pulses. TDR has been studied by experiments and simulations on deuterated uniformly ^{13}C-labelled alanine. Simulations and experiments show a relatively good agreement between them, demonstrating the validity of the concept. However, some discrepancies are found due mainly to imperfect behaviour of the selective pulses, heteronuclear in-

teractions, relaxation effects and *J*-coupling evolution. Further investigations need to be done to understand and improve the effects of these problems.

Appendices

Appendix A.

1. The space and spin parts for a list of spin interactions:

Interactions	Frame	Space Part				Spin Part
		$[A^{\Lambda}_{00}]^F$	$[A^{\Lambda}_{20}]^F$	$[A^{\Lambda}_{2\pm1}]^F$	$[A^{\Lambda}_{2\pm2}]^F$	
Zeeman	L	ω_0	-	-	-	T^j_{10}
isoCS	L	$\omega_0\delta^j_{iso}$	-	-	-	T^j_{10}
CSA	P	-	$\omega_0(\delta^P_{zz}-\delta^j_{zz})$	0	$\frac{\eta}{\sqrt{6}}[A_{20}]^P$	T^j_{10}
Homonuclear DD-couplings	P	-	$\sqrt{6}b_{jk}$	0	0	T^{jk}_{20}
Homonuclear J-couplings	L	$-\sqrt{3}\ 2\pi J$	-	-	-	T^{jk}_{00}
Heteronuclear DD-couplings	P	-	$2b_{jk}$	0	0	$T^I_{10}T^S_{10}$
Heteronuclear J-couplings	L	$2\pi J$	-	-	-	$T^I_{10}T^S_{10}$

2. Relationships between the spatial tensor components A^{Λ}_{lm} and $\mathcal{A}^{\Lambda}_{lm}$, and the spin tensor components $T^{\Lambda}_{\lambda 0}$ and the spin-field tensor components $\mathcal{T}^{\Lambda}_{\lambda 0}$:

Interactions	C^{Λ}	Space Part	Spin Part
Zeeman	$-\gamma_S$	$[\mathcal{A}_{00}]^L=-\frac{\sqrt{3}}{\omega_0}[A_{00}]^L$	$[\mathcal{T}_{00}]^L=-\frac{1}{\sqrt{3}}B_0T^j_{10}$
isoCS	$-\gamma_S$	$[\mathcal{A}_{00}]^L=-\frac{\sqrt{3}}{\omega_0}[A_{00}]^L$	$[\mathcal{T}_{00}]^L=-\frac{1}{\sqrt{3}}B_0T^j_{10}$
CSA	$-\gamma_S$	$[\mathcal{A}_{2m}]^P=\frac{\sqrt{3}}{\sqrt{2}\omega_0}[A_{2m}]^P$	$[\mathcal{T}_{20}]^L=\sqrt{\frac{3}{2}}B_0T^j_{10}$
Homonuclear DD-couplings	1	$[\mathcal{A}_{2m}]^P=[A_{2m}]^P$	$[\mathcal{T}_{20}]^L=T^{jk}_{20}$
Homonuclear J-couplings	2π	$[\mathcal{A}_{00}]^L=\frac{1}{2\pi}[A_{00}]^L$	$[\mathcal{T}_{00}]^L=T^{jk}_{00}$
Heteronuclear DD-couplings	1	$[\mathcal{A}_{2m}]^P=\sqrt{\frac{3}{2}}[A_{2m}]^P$	$[\mathcal{T}_{20}]^L=\frac{1}{\sqrt{6}}(2T^I_{10}T^S_{10}+T^I_{1-1}T^S_{11}+T^I_{11}T^S_{1-1})$
Heteronuclear J-couplings	2π	$[\mathcal{A}_{00}]^L=-\frac{\sqrt{3}}{2\pi}[A_{00}]^L$	$[\mathcal{T}_{00}]^L=-\frac{1}{\sqrt{3}}(2T^I_{10}T^S_{10}-T^I_{1-1}T^S_{11}-T^I_{11}T^S_{1-1})$

Appendix B.

Experimental conditions for the experiments described in chapter 7.

All the tables employ the following notation:

$|\kappa|$ = Magnitude of scaling factor for recoupled heteronuclear dipole-dipole interaction;

$\omega_{nut}^{S}/2\pi = N\omega_r/N$ = theoretical nutation frequency for 13C field;

$\Delta^S/2\pi$ = difference between optimized experimental 13C nutation frequency and theoretical values;

$\phi = \pi\nu/N$ = theoretical phase shift for sequence;

$\Delta\phi$ = difference between optimized experimental phase shift and theoretical value;

q = number of R or C elements used for DQ excitation and reconversion;

τ = excitation and reconversion times;

DQF_0 = experimental DQ filtering efficiency with no decoupling ;

DQF_{120} = experimental DQ filtering efficiency with a decoupling nutation frequency of 120 kHz;

1. RN_n^ν sequences.

a) Diammonium [2,3-$^{13}C_2$]-Fumarate.

$\omega_r/2\pi = 6.000\,kHz$

Symmetry	$\lvert\kappa\rvert$	$\omega_{nut}^S/2\pi$ /kHz	$\Delta^S/2\pi$ /kHz	$\phi=\pi\nu/N$ /°	$\Delta\phi$ /°	q	τ/ms	DQF_0 /%	DQF_{120} /%
$R12_2^5$	0.170	36	-1.06	75	-0.2	12	0.333	3.1	39.5
$R14_2^6$	0.172	42	-2.58	77.1	-0.1	14	0.333	6.8	35.5
$R16_2^7$	0.173	48	-3.47	78.7	-0.2	16	0.333	18.5	41.5
$R18_2^8$	0.174	54	-5.63	80	-0.2	18	0.333	22.4	40.5
$R20_2^9$	0.174	60	-8.44	81	-0.3	20	0.333	29.4	34.2
$R24_2^{11}$	0.175	72	-8.89	82.5	-0.3	24	0.333	34.9	-
$R28_2^{13}$	0.175	84	-12	83.5	-0.4	28	0.333	33.5	-
$R32_2^{15}$	0.176	96	-11.83	84.4	-0.3	32	0.333	36.5	-
$R36_2^{17}$	0.176	108	-11.06	85	-0.4	36	0.333	36.8	-
$R40_2^{19}$	0.176	120	-9.63	85.5	-0.3	40	0.333	36.6	-

b) Diammonium [2,3-$^{13}C_2$]-Fumarate.

$\omega_r/2\pi = 12.000\,kHz$

Symmetry	$\lvert\kappa\rvert$	$\omega_{nut}^S/2\pi$ /kHz	$\Delta^S/2\pi$ /kHz	$\phi=\pi\nu/N$ /°	$\Delta\phi$ /°	q	τ/ms	DQF_0 /%	DQF_{120} /%
$R12_2^5$	0.170	72	-10.20	75	-0.6	24	0.333	26.8	22.3
$R14_2^6$	0.172	84	-8.50	77.1	-0.7	28	0.333	37.8	-
$R16_2^7$	0.173	96	-12.47	78.7	-0.6	32	0.333	43.0	-
$R18_2^8$	0.174	108	-13.00	80	-0.7	36	0.333	39.5	-
$R20_2^9$	0.174	120	-13.00	81	-0.7	40	0.333	48.3	-

c) [^{15}N,$^{13}C_2$]-glycine.

$\omega_r/2\pi$=**6.000** ***kHz***

Symmetry	$\|\kappa\|$	$\omega_{nut}^{s}/2\pi$ /kHz	$\Delta^{s}/2\pi$ /kHz	$\phi=\pi\nu/N$ /°	$\Delta\phi$ /°	q	τ/ms	DQF_0 /%	DQF_{120} /%
$R12_2^5$	0.170	36	-1.70	75	-0.2	18	0.500	0.4	24.1
$R14_2^6$	0.172	42	-2.56	77.1	-0.2	20	0.476	1.7	33.5
$R16_2^7$	0.173	48	-0.01	78.7	-0.2	24	0.500	5.3	31.5
$R18_2^8$	0.174	54	-0.84	80	-0.2	26	0.481	7.0	32.8
$R20_2^9$	0.174	60	-2.72	81	-0.2	28	0.467	10.6	20.6
$R24_2^{11}$	0.175	72	-2.033	82.5	-0.2	34	0.472	16.7	7.0
$R28_2^{13}$	0.175	84	-5.46	83.5	-0.2	40	0.476	25.9	4.6
$R32_2^{15}$	0.176	96	-2.02	84.4	-0.2	46	0.479	27.2	1.4
$R36_2^{17}$	0.176	108	-15.39	85	-0.3	52	0.481	27.5	0.3
$R40_2^{19}$	0.176	120	-10.59	85.5	-0.2	56	0.467	28.2	-

d) [^{15}N,$^{13}C_2$]-glycine.

$\omega_r/2\pi$=**12.000** ***kHz***

Symmetry	$\|\kappa\|$	$\omega_{nut}^{s}/2\pi$ /kHz	$\Delta^{s}/2\pi$ /kHz	$\phi=\pi\nu/N$ /°	$\Delta\phi$ /°	q	τ/ms	DQF_0 /%	DQF_{120} /%
$R12_2^5$	0.170	72	-4.77	75	-0.6	36	0.500	8.6	14.3
$R14_2^6$	0.172	84	-12.65	77.1	-0.9	42	0.500	21.2	2.7
$R16_2^7$	0.173	96	-10.59	78.7	-0.7	48	0.500	24.4	3.0
$R18_2^8$	0.174	108	-8.53	80	-0.7	54	0.500	26.8	-
$R20_2^9$	0.174	120	-8.53	81	-0.8	60	0.500	35.9	-

e) [2,3-$^{13}C_2$]-alanine.

$\omega_r/2\pi$=**6.000** ***kHz***

Symmetry	$\lvert\kappa\rvert$	$\omega_{nut}^{S}/2\pi$ /kHz	$\Delta^S/2\pi$ /kHz	$\phi=\pi\nu/N$ /°	$\Delta\phi$ /°	q	τ/ms	DQF_0 /%	DQF_{120} /%
$R12_2^5$	0.170	36	-1.36	75	-0.2	18	0.500	6.0	49.1
$R14_2^6$	0.172	42	-2.56	77.1	-0.2	20	0.476	8.9	45.3
$R16_2^7$	0.173	48	-4.10	78.7	-0.3	24	0.500	18.3	46.0
$R18_2^8$	0.174	54	-0.84	80	-0.3	28	0.519	19.2	44.0
$R20_2^9$	0.174	60	-1.70	81	-0.3	30	0.500	32.8	38.3
$R24_2^{11}$	0.175	72	-7.17	82.5	-0.4	36	0.500	36.5	12.8
$R28_2^{13}$	0.175	84	-5.11	83.5	-0.3	42	0.500	41.6	12.3
$R32_2^{15}$	0.176	96	-8.20	84.4	-0.3	48	0.500	41.9	7.1
$R36_2^{17}$	0.176	108	-15.39	85	-0.3	54	0.500	27.0	-
$R40_2^{19}$	0.176	120	-10.24	85.5	-0.4	60	0.500	41.2	-

f) [2,3-$^{13}C_2$]-alanine.

$\omega_r/2\pi$=**12.000** ***kHz***

Symmetry	$\lvert\kappa\rvert$	$\omega_{nut}^{S}/2\pi$ /kHz	$\Delta^S/2\pi$ /kHz	$\phi=\pi\nu/N$ /°	$\Delta\phi$ /°	q	τ/ms	DQF_0 /%	DQF_{120} /%
$R12_2^5$	0.170	72	-0.32	75	-0.6	36	0.500	26.3	27.2
$R14_2^6$	0.172	84	-5.11	77.1	-0.6	42	0.500	34.1	4.3
$R16_2^7$	0.173	96	-6.82	78.7	-0.7	48	0.500	48.8	2.4
$R18_2^8$	0.174	108	-1.68	80	-0.7	54	0.500	33.2	-
$R20_2^9$	0.174	120	-6.82	81	-0.8	60	0.500	47.6	-

2. CN_n^ν sequences.

a) Diammonium [2,3-$^{13}C_2$]-Fumarate.

$\omega_r/2\pi = 6.000\,kHz$

Symmetry	$\lvert\kappa\rvert$	$\omega_{nut}^S/2\pi$ /kHz	$\Delta^S/2\pi$ /kHz	$\phi=\pi\nu/N$ /°	$\Delta\phi$ /°	q	τ/ms	DQF_0 /%	DQF_{120} /%
$C7_2^1$	0.155	42	0	51.4	0	7	0.333	11.9	3.1
$C9_2^1$	0.163	54	0	40	0	14		17.5	0
$C11_2^1$	0.168	66	0	32.7	0	11	0.333	32.1	5.8
$C13_2^1$	0.170	78	0	27.7	0	13	0.333	38.7	5.9
$C15_2^1$	0.171	90	0	24	0	15	0.333	40.2	-
$C17_2^1$	0.172	102	0	21.2	0	17	0.333	38.5	-
$C19_2^1$	0.173	1140	0	18.9	0	18	0.316	35.7	-
$C20_2^1$	0.174	120	0	18	0	18	0.367	35.5	

b) Diammonium [2,3-$^{13}C_2$]-Fumarate.

$\omega_r/2\pi = 12.000\,kHz$

Symmetry	$\lvert\kappa\rvert$	$\omega_{nut}^S/2\pi$ /kHz	$\Delta^S/2\pi$ /kHz	$\phi=\pi\nu/N$ /°	$\Delta\phi$ /°	q	τ/ms	DQF_0 /%	DQF_{120} /%
$C7_2^1$	0.155	72	0	51.4	0	14	0.333	42.2	-
$C8_2^1$	0.160	84	0	45	0	16	0.333	40.5	-
$C9_2^1$	0.163	96	0	40	0	19	0.352	39.9	-
$C10_2^1$	0.165	108	0	36	0	22	0.360	42	-

Appendix C.

1. SIMPSON input files Chapter 7

a) RN_n^ν sequences

```
# R_n^nu sequence for homonuclear recoupling of two spin-1/2
nuclei in the presence of two 1H
#  the 1H decoupling power is varied
#  R element is (90)0(270)180


# define the spin system

spinsys {
    channels 13C 1H
    nuclei   13C 13C 1H 1H
    shift  1   0p  94p  0.59   -65 -102  9
    shift  2   0p  94p  0.59   -65 -102  9
    shift  3   0p   0   0        0    0  0
    shift  4   0p   0   0        0    0  0

    dipole 1 2 -3127          0    0    0
    dipole 1 3 -20938                0  120    0
    dipole 2 4 -20938                0   60  180
    dipole 1 4 -3057          0  153  180
    dipole 2 3 -3057          0   27    0
    dipole 3 4 -3821          0  142  180
}

#
# define specific parameters for the calculation
#
# Make sure that maxHdec is an integer multiple of stepHdec
#

par {
    variable N       12.
    variable n        2.
    variable nu       5.
    spin_rate         6000
    variable nRexc    12
    variable nRrec    12

    variable maxHdec 120000
    variable stepHdec 3000

    sw                  1000000/stepHdec
    np                  maxHdec/stepHdec +1

    start_operator    Inz
```

```
    detect_operator  -I1z-I2z

    gamma_angles     10
    crystal_file     rep100
    proton_frequency 300e6

    method             direct
    verbose          1111
    use_cluster      0
}

#
# start the pulse program
#
proc pulseq {} {
   global par
   maxdt 1

   set phi         [expr 180*$par(nu)/$par(N)]
   set rf          [expr $par(spin_rate)*$par(N)/$par(n)]
   set tR          [expr 1e6/$rf]
   set pw90      [expr 0.25*$tR]
   set pw270       [expr 0.75*$tR]

   matrix set 2 totalcoherence {-2 +2}

  for {set d 0} {$d <= [expr $par(np)-1]} {incr d} {

    reset
    set Hdec      [expr $d*$par(stepHdec)]


   for {set i 1} {$i <= [expr $par(nRexc)/2]} {incr i} {

 # R element
     pulse $pw90   $rf  [expr (+1)*$phi +   0]  $Hdec  0
     pulse $pw270  $rf  [expr (+1)*$phi + 180]  $Hdec  0

 # R' element
     pulse $pw90   $rf  [expr (-1)*$phi -   0]  $Hdec  0
     pulse $pw270  $rf  [expr (-1)*$phi - 180]  $Hdec  0
    }

     filter 2

   for {set i 1} {$i <= [expr $par(nRrec)/2]} {incr i} {

 # R element
     pulse $pw90   $rf  [expr (+1)*$phi +   0]  $Hdec  0
     pulse $pw270  $rf  [expr (+1)*$phi + 180]  $Hdec  0

 # R' element
     pulse $pw90   $rf  [expr (-1)*$phi -   0]  $Hdec  0
```

```
     pulse $pw270  $rf  [expr (-1)*$phi - 180]  $Hdec  0
    }

     acq
}

}

proc main {} {
    global par
    set f [fsimpson]
    fsave $f $par(name).fid
    funload $f
}
```

b) CN_n^ν sequences

```
# C_n^nu sequence for homonuclear recoupling of two spin-1/2
nuclei in the presence of two 1H
#  the 1H decoupling power is varied
#  C element is (90)0(360)180(270)0
#

# define the spin system

spinsys {
    channels 13C 1H
    nuclei   13C 13C 1H 1H
    shift  1   0p  94p  0.59   -65 -102  9
    shift  2   0p  94p  0.59   -65 -102  9
    shift  3   0p   0   0        0    0  0
    shift  4   0p   0   0        0    0  0

    dipole 1 2 -3127            0   0   0
    dipole 1 3 -20938                0   120 0
    dipole 2 4 -20938                0   60  180
    dipole 1 4 -3057            0   153 180
    dipole 2 3 -3057            0   27  0
    dipole 3 4 -3821            0   142 180
}

# define specific parameters for the calculation
#
# Make sure that maxHdec is an integer multiple of stepHdec
#

par {
    variable N          14.
    variable n       2.
    variable nu      1.
```

```
    spin_rate         6000
    variable nCexc    1
    variable nCrec    1

    variable maxHdec 120000
    variable stepHdec 3000

    sw                  1000000/stepHdec
    np                  maxHdec/stepHdec +1

    start_operator    Inz
    detect_operator   -I1z-I2z

    gamma_angles      10
    crystal_file      rep100
    proton_frequency 400e6

    method              direct
    verbose           1111
    use_cluster       0
}

#
# start the pulse program
#
proc pulseq {} {
   global par
   maxdt 1

   set rf          [expr 2*$par(spin_rate)*$par(N)/$par(n)]
   set t90 [expr 0.25e6/$rf]



# Calculate propagators



   matrix set 2 totalcoherence {-2 +2}

  for {set d 0} {$d <= [expr $par(np)-1]} {incr d} {

    reset
    set Hdec      [expr $d*$par(stepHdec)]

      set nprop    [expr round($par(N))]


 for {set i 1} {$i <= $nprop} {incr i} {

        set phase [expr $i*360.0*$par(nu)/$par(N)]
        pulse $t90 $rf $phase                              $Hdec 0
        pulse [expr 4.0*$t90] $rf [expr $phase+180]    $Hdec 0
```

```
        pulse [expr 3.0*$t90] $rf $phase                $Hdec 0

    }
store 1

reset

   for {set r 1} {$r <= [expr $par(nCexc)]} {incr r} {

prop 1


    }

     filter 2

   for {set r 1} {$r <= [expr $par(nCrec)]} {incr r} {

prop 1

    }

     acq
}

}


proc main {} {
    global par
    set f [fsimpson]
    fsave $f $par(name).fid
    funload $f
}
```

c) SIMPSON spin system parameters for U-^{13}C-^{15}N-glycine.

```
spinsys {
    channels 13C 1H
    nuclei   13C 13C 1H 1H
    shift  1   66.6p  -74.55p  0.88   -0.7 88.5  52.5
    shift  2  -66.6p  -19.43p  0.98   99.4 146.0  138.9
    shift  3   0p   0   0        0    0  0
    shift  4   0p   0   0        0    0  0

    dipole 1 2 -2138.4            0   180.0      0
    dipole 1 3 -23328                    0    69.5    240
    dipole 2 4 -3073.33                  0    28.8    120
    dipole 1 4 -23328.4           0     71.2    120
    dipole 2 3 -2982.3            0     28.1    240
    dipole 3 4 -21368.4           0     91.0     90.2
}
```

d) SIMPSON spin system parameters for 2,3-13C2-Alanine.

```
spinsys {
    channels 13C 1H
    nuclei   13C 13C 1H 1H 1H 1H
    shift  1   15.5p  -11.7p  0.76   39     77     -53
    shift  2  -15.5p  -0.44p  0.44   82     24      29
    shift  3    0p      0       0      0      0       0
    shift  4    0p      0       0      0      0       0
    shift  5    0p      0       0      0      0       0
    shift  6    0p      0       0      0      0       0

    dipole 1 2   -2147        0        0        0
    dipole 1 3  -23137        0      69.6       0
    dipole 2 4     390        0        0        0
    dipole 2 5     390        0        0        0
    dipole 2 6     390        0        0        0
    dipole 4 5   11118        0       90        0
    dipole 4 6   11118        0       90        0
    dipole 5 6   11118        0       90        0
    dipole 1 4   -2006        0        0        0
    dipole 1 5   -2006        0        0        0
    dipole 1 6   -2006        0        0        0
    dipole 2 3   -2985        0      152        0
    dipole 3 4   -7676        0      156        0
    dipole 3 5   -7676        0      156        0
    dipole 3 6   -7676        0      156        0
}
```

2. SIMPSON input files Chapter 8

a) Variable-Time Implementation

```
# C_n^nu sequence for selective homonuclear recoupling of two
spin-1/2 nuclei in multispin systems
#  C element is (90)0(360)180(270)0
#

spinsys {
    channels 13C
    nuclei   13C 13C 13C
    shift  1    -7890  7148      0.837   11.7  86.3   -53
    shift  2    4768   1980      0.437     39    77    -53
    shift  3    7890   1178      0.761     82    24     29


    dipole 1 2  -2117             176.8  109.6   -16.8
    dipole 1 3   -476                   176.8  145.3   -16.8
    dipole 2 3  -2148                   0       0       0


}

par {
    spin_rate               11000
    variable tau_r          1.0e6/spin_rate
    variable delta          1000
    variable eps            100

      variable  Tgauss              1e6*(2.0/delta)*(log(eps)/
3.141592654)
    variable m              int(ceil(Tgauss/(3.0*tau_r)))
    variable pw_Gauss       m*3.0*tau_r
    variable tau             pw_Gauss*0.5*sqrt(3.141592654/log
(eps))
    variable Gauss_pts      256
    variable dtG            pw_Gauss/Gauss_pts
    variable M              int(ceil(pw_Gauss/dtG))
    variable Gauss_pts_hf   int(floor(M/2))
    variable sigma          1/tau
    variable mGauss_pts_hf -1*int(floor(M/2))
    variable cs1            7890
    variable angolo             2.0*3.141592654e-6 *cs1*dtG
    variable nCmax          180
    variable Cstep          3
    variable n              3.
    variable nu             1.
    variable N              3.
    start_operator          I1x+I2x+I3x
    detect_operator         I3x
```

```
    gamma_angles            10
    crystal_file            rep100
    proton_frequency        400e6
    dipole_check            false
    method                    direct
    verbose                 1111
    use_cluster             0

    np                      nCmax/Cstep +1
    sw                      spin_rate*(N/n)/Cstep
}


proc pulseq {} {
   global par
   maxdt 1
   set NrFullCycles          [expr $par(nCmax)/$par(N)]
   set rf  [expr 8*$par(spin_rate)*$par(N)/$par(n)]
   set t360 [expr 1e6/$rf]
   set t90 [expr 0.25e6/$rf]
   set t270 [expr 0.75e6/$rf]



# Calculate propagators



       reset
       offset 0
for {set iG $par(mGauss_pts_hf)} {$iG < $par(Gauss_pts_hf)}
{incr iG} {

       set C    [expr cos($par(angolo)*$iG)]
       if { $C >= 0 } {
       set Amplfact $C
       set phG 0
       } elseif { $C < 0 } {
       set Amplfact [expr -1*$C]
       set phG 180
       }
       set rfG  [expr $par(sigma)/(1.0e-6)]
       pulse $par(dtG) [expr $Amplfact*$rfG*exp(-3.141592654*
$par(sigma)*$par(sigma)*$par(dtG)*$par(dtG)*$iG*$iG)] $phG
}
       store 1000

set nprop          [expr round($par(N))]

for {set i 1} {$i <= $nprop} {incr i} {
          reset [expr ($i-1)*(($t360*4)+(4*(1e6/$rf)))]
        offset 0
        set phase [expr $i*360.0*$par(nu)/$par(N)]
```

```
        delay  [expr 2*(1e6/$rf)]
        pulse  $t90 $rf $phase
        pulse  $t360 $rf [expr $phase+180]
        pulse  $t270 $rf $phase
        pulse  $t90 $rf [expr $phase+180]
        pulse  $t360 $rf $phase
        pulse  $t270 $rf [expr $phase+180]
        delay  [expr 2*(1e6/$rf)]
        store $i
    }

        reset
for {set i 1} {$i <= $nprop} {incr i} {
        prop $i
    }
        store 500

# Calculate DQ filter

  matrix set 2 totalcoherence {1 -1}



# Use calculated propagators to calculate curve

for {set r 0} {$r <= [expr $NrFullCycles]} {incr r} {

  reset

  #for {set i 1} {$i <= [expr $r]} {incr i} {
  # prop 500
  #}


  if { $r == 1 } {
        prop 500
        store 2001
  } elseif { $r > 1 } {
        prop 2001
        prop 500
        store 2001
  }

filter 2

        prop 1000

filter 2

   if { $r > 0 } {
        prop 2001
        }
```

```
    acq

}
}

proc main {} {
global par
    set f [fsimpson]
    fsave $f $par(name).fid
    funload $f

}
```

b) Constant-Time implementation

```
# C_n^nu sequence for selective homonuclear recoupling of two
spin-1/2 nuclei in multispin systems
#  C element is (90)0(360)180(270)0
#

spinsys {
    channels 13C
    nuclei   13C 13C 13C
    shift  1   -7890   7148      0.837   11.7  86.3  -53
    shift  2    4768   1980      0.437   39    77    -53
    shift  3    7890   1178      0.761   82    24     29

    dipole 1 2  -2117 176.8  109.6   -16.8
    dipole 1 3   -476 176.8  145.3   -16.8
    dipole 2 3  -2148 0      0       0

    jcoupling 1 2 55 0 0 0 0 0
    jcoupling 2 3 35 0 0 0 0 0
}

par {
    spin_rate               11000.0
    variable phmod          360
    variable phstep         36
    start_operator          Inx
    detect_operator         I1x
    gamma_angles            20
    crystal_file            rep256
    proton_frequency        400e6
    dipole_check            false
    method                    direct
    verbose                 1111
    use_cluster             0
    np                      (phmod/phstep)+1
    sw                      40000.0
```

```
}

proc pulseq {} {
   global par
   maxdt 1
   set tau_r [expr 1.0e6/$par(spin_rate)]
   set nC    3
   set n     3
   set nu    1
   set N     3
   set rf    [expr 8.0*$par(spin_rate)*$N/$n]
   set t360  [expr 1.0e6/$rf]
   set t90   [expr 0.25e6/$rf]
   set t270  [expr 0.75e6/$rf]
   set rfstrong 100000.0
   set t1802 [expr 0.5e6/$rfstrong]
   set t902  [expr 0.25e6/$rfstrong]
   set Tsync [expr $tau_r-$t902]

# Set parameters for Gaussian pulse
    set delta         1800.0
    set eps           100.0
     set Tgauss          [expr 1.0e6*(2.0/$delta)*(log($eps)/
3.1416)]
    set m             [expr int(ceil($Tgauss/($tau_r)))]
    set pw_Gauss      [expr $m*$tau_r]
     set tau              [expr $pw_Gauss*0.5*sqrt(3.1416/log
($eps))]
    set Gauss_pts     256
    set dtG           [expr $pw_Gauss/$Gauss_pts]
    set M             [expr int(ceil($pw_Gauss/$dtG))]
    set Gauss_pts_hf  [expr int(floor($M/2))]
    set sigma         [expr 1.0/$tau ]
    set mGauss_pts_hf [expr -1*int(floor($M/2))]
    set rfG           [expr $sigma/2.0e-6]

# Calculate propagators


#Calculate ideal pi pulse
reset $Tsync
pulse $t1802 $rfstrong 180
store 750


#Calculate selective 90 Gaussian
for {set i 0} {$i < $par(np) } {incr i } {
reset
offset 7890.0
for {set iG $mGauss_pts_hf} {$iG < $Gauss_pts_hf} {incr iG} {
                  pulse   $dtG   [expr   0.5*$rfG*exp(-3.1416*
$sigma*$sigma*$dtG*$dtG*$iG*$iG)] [expr $i*$par(phstep)]
}
```

```
        store [expr int(1000+$i)]
}


matrix set 2 totalcoherence {1 -1}


set nprop          $N


# C Calculation for C with 3/4 tau_r shift
reset [expr 0.75*$tau_r]
offset 0
for {set i 0} {$i < $nprop} {incr i} {
        set phase [expr $i*360.0*$nu/$N]
        delay  [expr 2.0*(1.0e6/$rf)]
        pulse  $t90 $rf $phase
        pulse  $t360 $rf [expr $phase+180.0]
        pulse  $t270 $rf $phase
        pulse  $t90 $rf [expr $phase+180.0]
        pulse  $t360 $rf $phase
        pulse  $t270 $rf [expr $phase+180]
        delay  [expr 2.0*(1.0e6/$rf)]
    }
         store 500
reset

# Calculate accumulated propagator for C block before Pi
pulse at time 0.75*tau_r
reset [expr 0.75*$tau_r]
if { $nC == 3 } {
         prop 500
         store 2001
  } elseif { $nC > 3 } {
  for { set i 3 } { $i <= [ expr $nC ] } { incr i 3 } {
         prop 2001
         prop 500
         store 2001
         }
  }
reset

# Calculate propagator for C-Pi-C block and store in 2002 at
time 0.75*tau_r
reset [expr 0.75*$tau_r]
   if { $nC > 0 } {
         prop 2001
         }
         pulseid $t1802 $rfstrong 0
   if { $nC > 0 } {
         prop 2001
         }
store 2002
```

```
reset


# Calculate propagator for C-Pi-C-C-Pi-C block and store in
2003 at time 0.75*tau_r
reset [expr 0.75*$tau_r]
   prop 2002
   prop 2002
   store 2003
   reset



# C Calculation for C with 1/4 tau_r shift
reset [expr 0.25*$tau_r]
offset 0
for {set i 0} {$i < $nprop} {incr i} {
        set phase [expr $i*360.0*$nu/$N]
        delay  [expr 2.0*(1.0e6/$rf)]
        pulse  $t90 $rf $phase
        pulse  $t360 $rf [expr $phase+180.0]
        pulse  $t270 $rf $phase
        pulse  $t90  $rf [expr $phase+180.0]
        pulse  $t360 $rf $phase
        pulse  $t270 $rf [expr $phase+180]
        delay  [expr 2.0*(1.0e6/$rf)]
    }
         store 600
reset


# Calculate accumulated propagator for C block after Pi pulse
at time 0.25*tau_r
reset [expr 0.25*$tau_r]
if { $nC == 3 } {
         prop 600
         store 3001
  } elseif { $nC > 3 } {
  for { set i 3 } { $i <= [ expr $nC ] } { incr i 3 } {
         prop 3001
         prop 600
         store 3001
         }
  }
reset

# Calculate propagator for C-Pi-C block and store in 2002 at
time 0.25*tau_r
reset [expr 0.25*$tau_r]
   if { $nC > 0 } {
         prop 3001
         }
```

```
        pulseid $t1802 $rfstrong 0
   if { $nC > 0 } {
        prop 3001
        }
store 3002
reset


# Calculate propagator for C-Pi-C-C-Pi-C block and store in
2003 at time 0.25*tau_r
reset [expr 0.25*$tau_r]
   prop 3002
   prop 3002
   store 3003
reset


# Use calculated propagators to calculate curve: phase loop

for {set r 0} {$r < [expr $par(np)]} {incr r } {
reset

delay [expr 0.75*$tau_r]
prop 2003
delay [expr 0.25*$tau_r]

filter 2
prop 1000
delay $Tsync
prop 750
delay $Tsync
prop [expr int(1000+$r)]
filter 2

    delay [expr 0.25*$tau_r]
    prop 3003
    delay [expr 0.75*$tau_r]

    acq
}
}

proc main {} {
global par
    set f [fsimpson]
    fsave $f $par(name).fid
    fsave $f $par(name).asc -xreim
    funload $f
}
```

c) SIMPSON spin system parameters for U-13C3-pyruvate.

```
spinsys {
    channels 13C
    nuclei   13C 13C 13C
    shift  1  -1825.6    82p 0.5 60  0  0
    shift  2   1825.6  -110p 0.6  0 95 90
    shift  3 -12308.9  -24p 0.7  0  0  0

    dipole 1 2 -2004 0 0 0
    dipole 1 3  -430 0 0 0
    dipole 2 3 -2259 0 0 0

    jcoupling 1 2 62.1 0 0  0 0 0
    jcoupling 1 3 13.5 0 0  0 0 0
    jcoupling 2 3 39.6 0 0  0 0 0
}
```

Bibliography

[1] E. M. Purcell, H. C. Torrey and R. V. Pound. Resonance Absorption by Nuclear Magnetic Moments in a Solid. *Phys. Rev.*, **69**, 37 (1946)

[2] F. Bloch, W. W. Hansen and M. Packard. Nuclear Induction. *Phys. Rev.*, **69**, 127 (1946)

[3] W. G. Proctor and F. C. Yu. The Dependence of a Nuclear Magnetic Resonance Frequency upon Chemical Compound. *Phys. Rev.*, **77**, 717 (1950)

[4] W. C. Dickinson. Dependence of the ^{19}F Nuclear Resonance Position on Chemical Compound. *Phys. Rev.*, **77**, 736 (1950)

[5] M. E. Peskin and D. V. Schroeder, *An Introduction to Quantum Field Theory*, Addison-Wesley, 1995

[6] M. H. Levitt, *Spin dynamics: Basics of Nuclear Magnetic Resonance*, Wiley, 2001

[7] A. Brinkmann, *Dipolar Recoupling in Magic-Angle-Spinning Nuclear Magnetic resonance, PhD thesis*, Stockholm University, 2001

[8] A. Abragam, *The Principles of Nuclear Magnetism*, Clarendon Press, Oxford, 1961

[9] E. Merzbacher, *Quantum Mechanics*, Wiley, New York, 1998

[10] B. I. Bleaney and B. Bleaney, *Electricity and Magnetism*, Oxford University Press, Oxford, 1976

[11] E. Fukushima and S. B. W. Roeder, *Experimental Pulse NMR. A Nuts and Bolts Approach*, Perseus Press, Cambridge, Massachusetts, 1986

[12] R. N. Bracewell, *The Fourier Transform and Its Applications*, McGraw-Hill, New York, 1986

[13] T. Gullion and J. Schaefer. Rotational-Echo Double-Resonance NMR. *J. Magn. Reson.*, **81**, 196 (1989)

[14] D. A. Varshalovich, A. N. Moskalev and V. K. Kheronskii, *Quantum Theory of Angular Momentum*, World Scientific, Singapore, 1988

[15] I. N. Levine, *Quantum Chemistry*, Prentice-Hall, (1991)

[16] M. Mehring and V. A. Weberruß, *Object-oriented Magnetic Resonance*, Academic Press, London, 2001

[17] M. E. Rose, *Elementary Theory of Angular Momentum*, John Wiley & Sons, Inc, 1957

[18] S. A. Smith, W. E. Palke and J. T. Gerig. The Hamiltonians of NMR, Part. I. *Conc. Magn. Reson.*, **4**, 107-144 (1992)

[19] M. Mehring, *Principles of High Resolution NMR in Solids*, Springer, Berlin, 1983

[20] M. M. Maricq and J. S. Waugh. NMR in Rotating Solids. *J. Chem. Phys.*, **70**, 3300-3316 (1979)

[21] C. P. Slichter, *Principle of Magnetic Resonance*, Springer-Verlag, Berlin, 1992

[22] C. Connor, J. W. Chang, and A. Pines. Magnetic Resonance Spectrometer with a dc SQUID Detector. *Rev. Sci. Instr.*, **61(3)**, 1059 (1990)

[23] W. S. Veeman. Carbon-13 Chemical Shift Anisotropy. *Prog. NMR Spectr.*, **16**, 193 (1984)

[24] K. Schmidt-Rohr and H. W. Spiess, *Multidimentional Solid-State NMR and Polymers*, Academic Press, London, 1996

[25] U. Haeberlen. High Resolution NMR in Solids. Selective Averaging. *Adv. Magn. Reson.*, **Supplement 1**, 1976

[26] J. Cavanagh, W. Fairbrother, A. G. Palmer and N. Skelton, *Protein NMR Spectroscopy: Principles and Practice*, Academic Press, San Diego, 1988

[27] L. van Dam and M. H. Levitt. BII Nucleotides in the B and C-Forms of Natural-Sequence Polymeric DNA: A New Model for the C-Form of DNA. *J. Mol. Biol.*, **304**, 541 (2000)

[28] K. Schmidt-Rohr, J. Clauss and H. W. Spiess. Correlation of Structure, Mobility, and Morphological Information in Heterogeneous Polymer Materials by Two-Dimensional Wideline-Separation NMR Spectroscopy. *Macromolecules*, **25**, 3273 (1992)

[29] M. Carravetta, *Symmetry-Based Double Quantum Recoupling in Solid*, Stockholm University, 2002

[30] R. R. Ernst, G. Bodenhausen and A. Wokaun., *Principles of Nuclear Magnetic Resonance in One and Two Dimensions*, Clarendon, Oxford, 1987

[31] S. P. Brown, M. Perez-Torralba, D. Sanz, R. M. Claramunt and L. Emsley. Direct Detection of a Hydrogen-Bond in the Solid State by NMR Through the Observation of a Hydrogen-Bond Mediated ^{15}N-^{15}N J-coupling. *J. Am. Chem. Soc.*, **124**, 1152 (2002)

[32] S. P. Brown, M. Perez-Torralba, D. Sanz, R. M. Claramunt and L. Emsley. Determining Hydrogen-bond Strengths in the Solid State by NMR: the Quantitative Measurement of Homonuclear J-couplings. *Chem. Commun.*, 1852 (2002)

[33] W. C. Lai, N. McLean, A. Gansmüller, M. A. Verhoeven, G. C. Antonioli, M. Carravetta, O. G. Johannessen, R. C. D. Brown, S. P. Brown, L. Emsley, W. J. de Grip, H. J. M. de Groot, J. Lugtenburg and M. H. Levitt. Accurate Measurements of ^{13}C-^{13}C *J*-couplings in the Rhodopsin Chromophore by Double-Quantum Solid-State NMR. *J. Am. Chem. Soc.*, **128**, 3878 (2006)

[34] P. Man. Quadrupolar Interactions. *Encyclopedia of Nuclear Magnetic Resonance*, **6**, 3838 (1996)

[35] A. J. Vega. Quadrupolar Nuclei in Solids. *Encyclopedia of Nuclear Magnetic Resonance*, **6**, 3869 (1996)

[36] R. Tycko. Overtone Spectroscopy of Quadrupolar Nuclei. *Encyclopedia of Nuclear Magnetic Resonance*, **5**, 3425 (1996)

[37] H. W. Spiess. Polymer Dynamics and Order from Multidimensional Solid-state NMR. *Encyclopedia of Nuclear Magnetic Resonance*, **6**, 3668 (1996)

[38] U. Haeberlen and J. S. Waugh. Coherent Averaging Effects in Magnetic Resonance. *Phys. Rev.*, **175**, 453 (1968)

[39] W. Magnus. On the Exponential Solution of Differential Equations for a Linear Operator. *Commun. Pure Appl.*, **7**, 649 (1954)

[40] S. R. Kiihne and H. J. M. de Groot, *Perspectives on Solid State NMR in Biology*, Kluwer Academic Publishers, 2001

[41] M. Carravetta, X. Zhao, O. G. Johannessen, W. C. Lai, M. A. Verhoeven, P. H. M. Bovee-Geurts, P. J. E. Verdegem, S. Kiihne, H. Luthman, H. J. M. de Groot, W. J. de Grip, J. Lugtenburg and M. H. Levitt. Protein-induced Bonding Perturbation of the Rhodopsin Chromophore Detected by Double-Quantum Solid-State NMR. *J. Am. Chem. Soc.*, **126**, 3948 (2004)

[42] D. H. Brouwer, R. J. Darton, R. E. Morris and M. H. Levitt. A Solid-state NMR Method for the Solution of Zeolite Crystal Structures. *J. Am. Chem. Soc.*, **127**, 10365 (2005)

[43] D. H. Brouwer, P. E. Kristiansen, C. A. Fyfe and M. H. Levitt. Symmetry-Based ^{29}Si Dipolar Recoupling Magic Angle Spinning NMR Spectroscopy: A New Method for Investigating Three-Dimensional Structures of Zeolite Frameworks. *J. Am. Chem. Soc.*, **542**, 127 (2005)

[44] I. J. Lowe. Free Induction Decay of Rotating Solids. *Phys. Rev. Lett.*, **2**, 285 (1950)

[45] E. R. Andrew, A. Bradbury and R. G. Eades. Removal of Dipolar Broadening of Nuclear Magnetic Resonance Spectra of Solids by Specimen Rotation. *Nature*, **182**, 1659 (1958)

[46] E. O. Stejskal, J. Schaefer and J. S. Waugh. Magic-Angle Spinning and Polarisation Transfer in Proton-enhanced NMR. *J. Magn. Reson.*, **28**, 105 (1977)

[47] A. Pines, M. G. Gibby and J. S. Waugh. Proton-enhanced NMR of Dilute Spins in Solids. *J. Chem. Phys.*, **59**, 569 (1973)

[48] F. Bloch. Dynamical Theory of Nuclear Induction. II. *Phys. Rev.*, **102**, 104 (1956)

[49] F. Bloch. Theory of Line Narrowing by Double-Frequency Irradiation. *Phys. Rev.*, **111**, 841 (1958)

[50] A. E. Bennett, C. M. Rienstra, M. Auger, K. V. Lakshmi and R. G. Griffin. Heteronuclear Decoupling in Rotating Solids. *J. Chem Phys*, **103**, 6951 (1995)

[51] B. M. Fung, A. K. Khitrin and K. Ermolaev. An Improved Broadband Decoupling Sequence for Liquid Crystals and Solids. *J. Magn. Reson.*, **142**, 97 (2000)

[52] R. E. Taylor. Setting up C-13 CP/MAS experiments. *Concepts in Magnetic Resonance Part A*, **22A (1)**, 37 (2004)

[53] R. K. Harris, *Nuclear Magnetic Resonance Spectroscopy, a Physicochemical View*, Longman, 1997

[54] M. J. Duer, *NMR Spectroscopy. Principles and Applications*, Blackwell Science, (2002)

[55] S. R. Hartmann and E. L. Hahn. Nuclear Double Resonance in the Rotating Frame. *Phys. Rev.*, **128**, 2042 (1962)

[56] G. Metz. X. Wu and S. O. Smith. Ramped-Amplitude Cross-Polarisation in Magic-Angle-Spinning NMR. *J. Magn. Reson.*, **110**, 219 (1994)

[57] M. Ernst. Heteronuclear Spin Decoupling in Solid-State NMR under Magic-Angle Sample Spinning. *J. Magn. Reson.*, **162**, 1 (2002)

[58] M. H. Levitt. Symmetry-Based Pulse Sequences in Magic-Angle Spinning Solid-State NMR. *Encyclopedia of Nuclear Magnetic Resonance*, **9**, 165 (2002)

[59] A. Brinkmann and M.H. Levitt. Symmetry Principles in the Nuclear Magnetic Resonance of Spinning Solids: Heteronuclear Recoupling by Generalised Hartmann-Hahn Sequences. *J. Chem. Phys.*, **115**, 357 (2001)

[60] R. Tycko and G. Dabbagh. Double-quantum Filtering in Magic-Angle-Spinning NMR Spectroscopy: An Approach to Spectral Simplification and Molecular Structure Determination. *J. Am. Chem. Soc.*, **113**, 9444 (1991)

[61] R. Tycko and S. O. Smith. Symmetry Principles in the Design of Pulse Sequences for Structural Measurements. *J. Chem. Phys.*, **98**, 932 (1993)

[62] A. E. Bennett, J. H. Ok, R. G. Griffin and S. Vega. Chemical Shift Correlation Spectroscopy in Rotating Solids: Radio Frequency-Driven Dipolar Recoupling and Longitudinal Exchange. *J. Chem. Phys.*, **96**, 8624 (1992)

[63] D. K. Sodickson, M. H. Levitt, S. Vega, and R. G. Griffin. Broadband Dipolar Recoupling in the Nuclear Magnetic Resonance of Rotating Solids. *J. Chem. Phys.*, **98**, 6742 (1993)

[64] A. E. Bennett, C. M. Rienstra, J. M. Griffiths, W. Zhen, P. T. Lansbury and R. G. Griffin. Homonuclear Radio frequency-Driven Recoupling in Rotating Solids. *J. Chem. Phys.*, **108**, 9463 (1998)

[65] N. C. Nielsen, H. Bildsøe, H. J. Jakobsen and M. H. Levitt. Double-quantum Homonuclear Rotary Resonance: Efficient Dipolar Recovery in Magic-Angle Spinning Nuclear Magnetic Resonance. *J. Chem. Phys.*, **101**, 1805 (1994)

[66] Y. K. Lee, N. D. Kurur, M. Helmle, O. G. Johannessen, N. C. Nielsen, M. H. Levitt. Efficient Dipolar Recoupling in the NMR of Rotating Solids. A Sevenfold Symmetric Radiofrequency Pulse Sequence. *Chem. Phys. Lett.*, **242**, 304 (1995)

[67] M. Hohwy, H. J. Jakobsen, M. Edén, M. H. Levitt and N. C. Nielsen. Broadband Dipolar Recoupling in the Nuclear Magnetic Resonance of Rotating Solids: A Compensated C7 Pulse Sequence. *J. Chem. Phys.*, **108**, 2686 (1998)

[68] C. M. Rienstra, M. E. Hatcher, L. J. Mueller, B. Sun, S. W. Fesik and R. G. Griffin. Efficient Multispin Homonuclear Double-Quantum Recoupling for Magic-Angle Spinning NMR: ^{13}C-^{13}C Correlation Spectroscopy of U-^{13}C-Erythromicin A. *J. Am. Chem. Soc.*, **120**, 10602 (1998)

[69] A. Brinkmann, M. Edén and M. H. Levitt. Synchronous Helical Pulse Sequences in Magic-Angle Spinning Nuclear Magnetic Resonance: Double Quantum Recoupling of Multiple Spin Systems. *J. Chem. Phys*, **112(19)**, 8539 (2000)

[70] M. Carravetta, M. Edén, X. Zhao, A. Brinkmann and M. H. Levitt. Symmetry Principles for the Design of Radiofrequency Pulse Sequences in the Nuclear Magnetic Resonance of Rotating Solids. *Chem. Phys. Lett.*, **321**, 205 (2000)

[71] T. Gullion and J. Schaefer. Detection of Weak Heteronuclear Dipolar Couplings by Rotational-Echo Double-Resonance Nuclear Magnetic Resonance. *Adv. Magn. Reson.*, **13**, 57 (1989)

[72] X. Zhao, J. L. Sudmeier, W. W. Bachovchin and M. H. Levitt. Heteronuclear Recoupling in Fast Magic-Angle Spinning Solid-State NMR Spectroscopy. Measurement of NH Bond Lengths and Quantification of Hydrogen Bonds. *J. Am. Chem. Soc.*, **123**, 11097 (2001)

[73] J. D. van Beek, R. Dupree and M. H. Levitt. Symmetry-Based Recoupling of ^{17}O-^{1}H Spin Pairs in Magic-Angle Spinning NMR. *J. Magn. Reson.*, **179**, 39 (2006)

[74] A. Brinkmann and A. P. M. Kentgens. Sensitivity Enhancement and Heteronuclear Distance Measurements in Biological ^{17}O Solid-State NMR. *J. Phys. Chem.*, **B 110**, 16089 (2006)

[75] I. Marin Montesinos, D. H. Brouwer, G. Antonioli, W.C. Lai, A. Brinkmann, and M. H. Levitt. Heteronuclear Decoupling Interference During Symmetry-based Homonuclear Recoupling in Solid-State NMR. *J. Magn. Reson.*, **177**, 307 (2005)

[76] X. Zhao, W. Hoffbauer, J. Schmedt auf der Günne and M. H. Levitt. Heteronuclear Polarization Transfer by Symmetry-Based Recoupling Sequences in Solid-State NMR. *Solid State NMR*, **26**, 57 (2004)

[77] A. Brinkmann and A. P. M. Kentgens. Proton-Selective ^{17}O-^{1}H Distance Measurements in Fast Magic-Angle-Spinning Solid-State NMR Spectroscopy for the Determination of Hydrogen Bond Lengths. *J. Am. Chem. Soc.*, **128**, 14758 (2006)

[78] I. Marin-Montesinos, G. Mollica, M. Carravetta, A. Gansmüller, G. Pileio, M. Bechmann, A. Sebald and M. H. Levitt. Truncated Dipolar Recoupling in Solid-State Nuclear Magnetic Resonance. *Chem. Phys. Lett.*, **572**, 432 (2006)

[79] U. Haeberlen and J. S. Waugh. Coherent Averaging Effect in Magnetic Resonance. *Phys. Rev.*, **175**, 453 (1968)

[80] A. Brinkmann and M. Edén. Second-order Average Hamiltonian Theory of Symmetry-based Pulse Schemes in the Nuclear Magnetic Resonance of Rotating Solids: Application to Triple-Quantum Dipolar Recoupling. *J. Chem. Phys.*, **120**, 11726 (2004)

[81] S. Wolfram, *The Mathematica Book*, Wolfram Media, Inc, (2003)

[82] H. Hosomi, Y. Ito and S. Ohba. Ammonium and Isopropylammonium Salts of the Fumaric Acid Dianion. *Acta Cryst. C*, **54**, 142 (1998)

[83] P. G. Jonsson and A. Kvick. Precision Neutron Diffraction Structure Determination of Protein and Nucleic Acid Components. III. The Crystal and Molecular Structure of the Amino Acid α-Glycine. *Acta Cryst. B*, **28**, 1827 (1972)

[84] M. S. Lehmann, T. F. Koetzle, and W. C. Hamilton. Precision Neutron Diffraction Structure Determination of Protein and Nucleic Acid Components. I. The crystal and Molecular Structure of the Amino Acid L-Alanine. *J. Am. Chem. Soc.*, **94:8**, 2657 (1972)

[85] W. Rach, G. Kiel and G. Gattow. Untersuchungen über Salze der Pyruvinsäure. 2. Kristallstruktur von Kaliumpyruvat, Neubestimmung dere Struktur von Natriumpyruvat. *Z. Anorg. Allg. Chem.*, **563**, 87 (1988)

[86] J. S. Frye and G. E. Maciel. Setting the Magic-Angle using a Quadrupolar Nuclide.

J. Magn. Reson., **48**, 125 (1982)

[87] D. D. Laws, H. M. L. Bitter and A. Jerschow. Solid State NMR Spectroscopy. Methods in Chemistry. *Angew. Chem. Int.*, **41**, 3096 (2002)

[88] F. Stickney de Bouregas and J. S. Waugh. ANTIOPE. A Program for Computer Experiments on Spin Dynamics. *J. Magn. Reson.*, **96**, 280 (1992)

[89] S. A. Smith, T. O. Levante, B. H. Meier and R. R. Ernst. Computer Simulations in Magnetic Resonance. An Oriented Programming Approach. *J. Magn. Reson.*, **106**, 75 (1994)

[90] M. Bak, J. T. Rasmussen and N. C. Nielsen. SIMPSON: A General Simulation Program for Solid-State NMR Spectroscopy. *J. Mag. Reson.*, **147**, 296 (2000)

[91] M. Veshtort and R. G. Griffin. SPINEVOLUTION: A Powerful Tool for the Simulation of Solid and Liquid State NMR Experiments. *J. Magn. Reson.*, **178**, 248 (2006)

[92] J. K. Ousterhout, *Tcl and the Tk Toolkit*, Addison-Wesley Publication Company, 1994

[93] W. A. Dollase, M. Feike, H. Forster, T. Schaller, I. Schnell, A. Sebald and S. Steuernagel. A 2D P-31 MAS NMR Study of Polycrystalline $Cd_3(PO_4)_2$. *J. Am. Chem. Soc*, **119**, 3807 (1997)

[94] F. Fayon, C. Bessada, J. P. Coutures, and D. Massiot. High-resolution Double-Quantum P-31 MAS NMR Study of the Intermediate-Range Order in Crystalline and Glass Lead Phosphates. *Inorg. Chem.*, **38**, 5212 (1999)

[95] X. Helluy, C. Marichal and A. Sebald. Though-bond Indirect and Through-Space Direct Dipolar Couplings P-31 MAS NMR Constraints for Spectral Assigment in the Cubic 3 X 3 X 3 Superstructure of Ti_2O_7. *J. Phys. Chem. B*, **104**, 1836 (2000)

[96] A. Le Sauze, L. Montagne, G. Palavit, F. Fayon, and R. Marchand. X-ray Photo-Electron Spectroscopy and Nuclear Magnetic Resonance Structural Study of Phosphorus Oxynitride Glasses, "LiNaPON". *J. Non Cryst. Solids*, **263**, 139 (2000)

[97] M. Baldus. Correlation Experiments for Assignment and Structure Elucidation of Immobilized Polypeptides under Magic Angle Spinning. *Prog. NMR Spectrosc.*, **41**, 1 (2002)

[98] M. Edén and M. H. Levitt. Excitation of Carbon-13 Triple Quantum Coherence in Magic-Angle-Spinning NMR. *Chem. Phys. Lett.*, **293**, 173 (1998)

[99] H. Geen, R. Graf, A. S. D. Heinrichs, B. S. Hickman, I. Schnell, H. W. Spiess. Spin Counting with Fast MAS. *J. Magn. Reson.*, **138**, 167 (1999)

[100] C. E. Hughes, J. Schmedt auf der Günne and M. H. Levitt. A Test for the Number of Coupled Spins I = 1/2 in Solids. Zero-Quantum Recoupling of Multiple-Quantum Coherences. *Chem. Phys. Chem.*, **4**, 457 (2003)

[101] M. Edén. Order-Selective Multiple-Quantum Excitation in Magic-Angle Spinning NMR: Creating Triple-Quantum Coherences with a Trilinear Hamiltonian. *Chem. Phys. Lett.*, **366**, 469 (2002)

[102] M. Carravetta, M. Edén, O. G. Johannessen, H. Luthman, P. Verdegem, A. Sebald, and M. H. Levitt. Estimation of Carbon-Carbon Bond Lengths and Medium-Range Internuclear Distances by Solid-State Nuclear Magnetic Resonance. *J. Am. Chem. Soc.*, **123**, 10628 (2001)

[103] X. Feng, Y. K. Lee, D. Sandstrom, M. Edén, H. Maisel, A. Sebald, and M. H. Levitt. Direct Determination of a Molecular Torsional Angle by Solid-State NMR. *Chem. Phys. Lett.*, **257**, 314 (1996)

[104] X. Feng, P. J. E. Verdegem, Y. K. Lee, D. Sandstrom, M. Edén, P. Bovee-Geurts, W. J. de Grip, J. Lugtenburg, H. J. M. de Groot and M. H. Levitt. Direct Determination of a Molecular Torsional Angle in the Membrane Protein Rhodopsin by Solid-State NMR. *J. Am. Chem. Soc.*, **119**, 6853 (1997)

[105] S. Ravindranathan, T Karlsson, K. Lycknert, G. Widmalm and M. H. Levitt. Conformation of the Glycosidic Linkage in a Disaccharide Investigated by Double-Quantum Solid-State NMR. *J. Magn. Reson.*, **151**, 136 (2001)

[106] M. Carravetta, Y. Murata, M. Murata, I. Heinmaa, R. Stern, A. Tontcheva, A. Somoson, Y. Rubin, K. Komatsu, and M. H. Levitt. Solid-State NMR Spectroscopy of Molecular Hydrogen Trapped Inside an Open-Cage Fullerene. *J. Am. Chem. Soc.*, **126**, 4092 (2004)

[107] Y. Ishii, J. Ashida and T. Terao. ^{13}C-^{1}H Dipolar Recoupling Dynamics in ^{13}C Multiple Pulse Solid-State NMR. *Chem. Phys. Lett.*, **246**, 439 (1995)

[108] P. E. Kristiansen, D. J. Mitchell and J. N. S. Evans. Double-Quantum Dipolar Recoupling at High Magic-Angle Spinning Rates. *J. Magn. Reson.*, **154**, 253 (2002)

[109] Y. Ishii. ^{13}C-^{13}C Dipolar Recoupling Under Very Fast Magic-Angle Spinning in Solid-State NMR: Applications to Distance Measurements, Spectral Assigments, and High-Throughput Secondary-structure Determination. *J. Chem. Phys.*, **114**, 8473 (2001)

[110] C. E. Hughes, S. Luca and M. Baldus. Radio-frequency Driven Polarisation Transfer without Heteronuclear Decoupling in Rotating Solids. *Chem. Phys. Lett*, **385**, 435 (2004)

[111] J. Schmedt auf der Günne. Effective Dipolar Couplings Determined by Dipolar

Dephasing of Double-Quantum Coherences. *J. Magn. Reson.*, **180**, 186 (2006)

[112] V. Ladizhansky and R. G. Griffin. Band-Selective Carbonyl to Aliphatic Side Chain ^{13}C-^{13}C Distance Measurements in U-^{13}C,^{15}N-Labeled Solid Peptides by Magic Angle Spinning NMR. *J. Am. Chem. Soc.*, **126**, 948 (2004)

[113] C. P. Jaroniec, B. S. Tounge, J. Herzfeld and R. G. Griffin. Frequency-Selective Heteronuclear Dipolar Recoupling in Rotating Solids: Accurate ^{13}C-^{15}N Distance Measurements in Uniformly ^{13}C,^{15}N-labeled Peptides. *J. Am. Chem. Soc.*, **123**, 3507 (2001)

[114] A. Verhoeven, P. T. F. Williamson, H. Zimmermann, M. Ernst, and B. H. Meier. Rotational-Resonance Distance Measurements in Multi-spin Systems. *J. Magn. Reson.*, **168**, 314 (2004)

[115] A. T. Petkova. A Test for the Number of Coupled Spins I=1/2 in Magic-Angle-Spinning Nuclear Magnetic Resonance. *J. Magn. Reson.*, **168**, 137 (2004)

[116] K. Komura, K. Takegoshi, T. Terao, K. Uchida and M. Kainosho. Determination of the Complete Structure of a Uniformly Labeled Molecule by Rotational Resonance Solid-State NMR in the Tilted Rotating Frame. *J. Am. Chem. Soc.*, **121**, 4064 (1999)

[117] R. Tycko. Normal Angle Spinning Dipolar Spectroscopy for Structural Studies by Solid-State Nuclear Magnetic Resonance. *J. Am. Chem. Soc.*, **116**, 2217 (1994)

[118] A. C. Kolbert, P. J. Grandinetti, M. Baldwin, S. B. Prusiner and A. Pines. Measurement of Internuclear Distances by Switched Angle Spinning NMR. *J. Phys. Chem.*, **98**, 7936 (1994)

[119] A. Brinkmann, J. Schmedt auf der Günne and M. H. Levitt. Homonuclear Zero-Quantum Recoupling in Fast Magic-Angle Spinning Nuclear Magnetic Resonance. *J. Magn. Reson.*, **156**, 79 (2002)

[120] R. Freeman. Shaped Radiofrequency Pulses in High Resolution NMR. *Prog. NMR Spectrosc.*, **32**, 59 (1998)

[121] M. Edén and M. H. Levitt. Numerical Simulation of Periodic NMR Problems: Fast Calculation of Carousel Averages. *Mol. Phys.*, **95**, 879 (1998)

[122] M. Bak and N. C. Nielsen. REPULSION, a Novel Approach to Efficient Powder Averaging in Solid-State NMR. *J. Magn. Reson.*, **125**, 132 (1997)

[123] Y. Ishii, J. J. Balbach and R. Tycko. Measurement of Dipole-Coupled Lineshapes in a Many-Spin System by Constant-Time Two-Dimensional Solid-State NMR with High-Speed Magic-Angle Spinning. *Chem. Phys.*, **266**, 231 (2001)

[124] G. N. Watson, *Theory of Bessel Functions*, Cambridge University Press, 1922